Quantitative Approach to Supramolecular Assembly Engineering for Isolating and Activating Antigen-Specific T Cells

by

Mason R. Smith

A dissertation submitted in partial fulfillment
of the requirements for the degree of
Doctor of Philosophy
(Chemical Engineering)
in the University of Michigan
2018

Doctoral Committee:

Assistant Professor Fei Wen, Chair
Professor Jennifer J. Linderman
Professor Malini Raghavan
Assistant Professor Greg M. Thurber

Mason R. Smith

masonrsm@umich.edu

ORCID iD: 0000-0002-0005-2535

Dedication

To my parents, Geoff and Rhonda Smith

Acknowledgements

First, I would like to thank my advisor, Professor Fei Wen, for her valuable insight and mentorship throughout the course of my Ph.D. It has been a long road, and I am grateful to Professor Wen for her constant support and encouragement, which pushed me to do my best as a graduate student and as a researcher. When I leave the lab and begin a career, I will undoubtedly draw on lessons I have learned from Professor Wen. I would also like to thank my committee members: Professor Jennifer Linderman, Professor Malini Raghavan, and Professor Greg Thurber, for their valuable feedback over the years. As a student, interacting with established experts on one's committee can be intimidating; however, I always left these exchanges feeling encouraged and grateful for their advice.

Pursuing a Ph.D has been one of the most challenging endeavors I have undertaken in my life. While the journey has been incredibly rewarding, there were times when I questioned whether I had made the right decision. At these moments, I could always rely on a great group of friends to keep things in perspective. I would therefore like to thank Brett, Vikesh, Dave, Sumit, Trenton, Cornelius, and Bob for their company and conversation. When I look back on my time in Ann Arbor, it will be the friendships I made there that I value most. Of course, no one has been a better friend through the highs and lows of graduate school than my wonderful girlfriend,

Deepika. I have learned so much from you over the past five years and I am excited to see what the future holds for us.

Finally, I would like to thank my parents and sister for all their love and support throughout my entire academic career. From high school wrestling matches, to dropping me off in Morgantown, to watching Ratchet on weekend escapes from Ann Arbor, you have always been there.

Table of Contents

List of Tables

List of Figures

Abstract

T cell immunotherapy is a novel therapeutic strategy that aims to leverage the antigen-specific nature of a T cell immune response to treat a variety of immunological conditions. Over the past twenty years, T cell immunotherapy has been applied to treat several types of cancer, autoimmune conditions, and chronic infections, culminating in the FDA approval of two highly effective chimeric antigen receptor (CAR) T cell therapies targeting hematological cancers in 2017. While the initial success of T cell immunotherapy has been encouraging, identifying appropriate antigenic targets and optimizing T cell activation to promote effective responses *in vivo* remain significant challenges. In this dissertation, we discuss the development and application of new molecular tools for identifying, isolating, and activating antigen-specific T cells, which are directly relevant to the current challenges facing T cell immunotherapy.

One of the greatest obstacles to developing a successful T cell immunotherapy is the selection of appropriate antigenic targets. T cells naturally recognize antigen-derived peptides presented on polymorphic major histocompatibility complex (MHC) proteins, and different MHC alleles exhibit different peptide binding specificities. Therefore, peptides that promiscuously bind multiple MHC alleles representing a diverse population have significant potential in the development of broadly protective peptide-based therapeutics and vaccines. A number of high-throughput *in silico* strategies have been developed to predict peptide-MHC

binding; however, the accuracy of these approaches is generally inadequate for the reliable prediction of class II peptide-MHC (MHCII) interactions. In contrast, most experimental systems designed to measure peptide-MHCII binding emphasize quantitative detail over throughput. In this dissertation, we develop and validate a high-throughput screening strategy to evaluate peptide binding to four common MHCII alleles. Using this strategy, which we have termed microsphere-assisted peptide screening (MAPs), we screened overlapping peptide libraries of antigenic viral proteins and identified 12 promiscuously MHCII-binding peptides. Subsequent structural analysis indicated that nearly half of these peptides overlapped with antibody neutralization sites on the respective viral protein. Together, these results indicate that the MAPS strategy can be used to rapidly identify promiscuously binding and immunodominant peptides that have therapeutic relevance.

Another significant challenge limiting the successful application of T cell immunotherapy is expanding a clinically relevant number of therapeutically effective T cells. The effectiveness of a T cell response is largely determined by the spatial and stoichiometric organization of signals delivered to the T cell during T cell activation. One strategy for promoting an effective T cell response is to tune the presentation of stimulatory and costimulatory signals through artificial antigen presentation. However, existing technologies have a limited ability to control the spatial and stoichiometric organization of T cell ligands on 3D surfaces. In this dissertation, we introduce a novel strategy for presenting highly organized clusters of stimulatory and costimulatory ligands to T cells using protein-scaffold directed assembly. Using this approach, we systematically investigated how the global surface density, local valency, and stoichiometric ratio of T cell ligands on a 3D cellular (yeast) surface can be manipulated to tune T cell activation. After validating this approach, we further develop more complex scaffold-assembly

schemes to enhance the controllability of isolating and activating antigen-specific T cells. We believe that MAPS and artificial antigen presentation using protein-scaffold directed assembly provide a robust toolset for identifying, isolating, and activating antigen-specific T cells for T cell immunotherapy.

Chapter 1. Introduction

1.1. T Cell Immunity

T cells are specialized cells of the adaptive immune system that inspect antigen presenting cells (APCs) for signs of disease using a surface protein called a T cell receptor (TCR). Each T cell expresses a unique TCR that recognizes a specific peptide (antigen) bound to a major histocompatibility complex (MHC) protein. All nucleated cells in the body process and present peptides derived from intracellular proteins on class I MHC (MHCI), while certain phagocytic cells (macrophages, dendritic cells, and B cells) process and present peptides derived from extracellular material on class II MHC (MHCII). Peptide-MHCI (pMHCI) complexes are recognized by $CD8^+$ cytotoxic T cells, which directly lyse cells presenting the recognized antigen. In contrast, peptide-MHCII (pMHCII) complexes are recognized by $CD4^+$ helper T cells, which secrete immune-modulating cytokines that promote antigen uptake and B cell differentiation or attenuate an immune response upon pMHCII recognition.

1.1.1 Peptide-MHC Binding

Because T cell antigen recognition is restricted to MHC-presented peptides, peptide-MHC binding is a prerequisite to an antigen-specific T cell response. Therefore, understanding how peptides are presented on MHC molecules is an important consideration in T cell immunity. Both MHCI and MHCII molecules are highly polymorphic heterodimeric proteins, consisting of

an alpha chain and a beta chain. MHC polymorphism results in a number of distinct MHCI and MHCII alleles, the frequency of which varies between diverse ethnic populations. To date, 13,680 MHCI alleles and 5,091 MHCII alleles have been identified.[1] An important consequence of this MHC polymorphism is that different MHC alleles exhibit different peptide-binding specificities. As a result, peptides that are stably presented on one MHC allele might not be presented at all on another MHC allele.

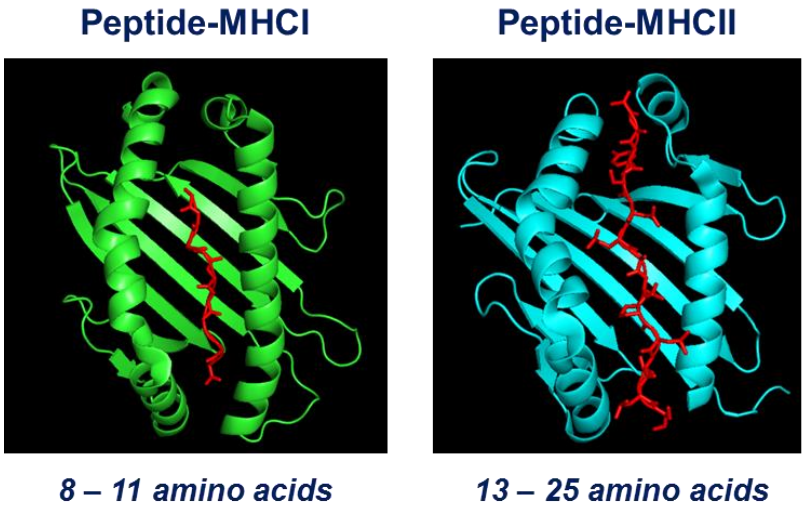

Figure 1.1. Top down representation of peptide-MHC binding.
Peptide (red) is shown within the peptide-binding groove of MHCI (green) and MHCII (cyan). The peptide-MHCI interaction represents HLA-A2 in complex with a 9mer hepatitis B virus peptide (UniProt: 5E00).[2] The peptide-MHCII interaction represents HLA-DR1 in complex with the 15mer invariant chain peptide CLIP (UniProt: 3QXA).[3]

While both MHCI and MHCII are polymorphic heterodimeric proteins, they differ significantly in how they present antigenic peptides. Peptides presented on MHCI are derived from cytosolic proteins, which are degraded into 8 – 11 amino acid peptides by the proteasome and loaded on MHCI molecules in the endoplasmic reticulum.[4,5] In contrast, peptides presented on MHCII are derived from exogenous proteins, which are endocytosed and degraded into longer 13 – 25 amino acid peptides by proteases.[6] The early endosomes containing the processed

peptides then fuse with larger endosomes containing MHCII for peptide loading.[5] For both MHCI and MHCII, peptides are bound by interacting with anchoring residues in a region of the MHC molecule called the peptide-binding groove. The peptide-binding groove of MHC is composed of a beta-sheet floor flanked by two alpha helices (**Figure 1.1**). The amino acid content of the peptide-binding groove is determined by the particular MHC allele, and thus different MHC alleles tend to bind different peptides. Because there are many different MHC alleles and the frequency of these alleles varies based on genetic history and ethnicity, peptides that stably bind multiple MHC alleles are of considerable interest. Such peptides are referred to as "promiscuously binding peptides", and have significant potential for the development of broadly protective of peptide-based therapeutics and vaccines.[7–10]

Although the general structure of MHCI and MHCII peptide-binding grooves appear similar (**Figure 1.1**), they have one important difference. The peptide-binding groove of MHCI is closed at both ends, completely accommodating 8 – 11 amino acid peptides within the groove. In contrast, the peptide-binding groove of MHCII is open at both ends, accommodating longer and variable length peptides by allowing the peptide to extend outside of the ends of the groove. Peptide-MHCII binding is primarily governed by the interactions between a continuous 9mer binding core (also referred to as the peptide-biding register, or PBR) within the peptide and the peptide-binding groove.[11] However, because MHCII-presented peptides are longer than nine amino acids, peripheral flanking residues (PFRs) outside the 9mer binding core can also affect peptide-MHCII binding through complex, secondary interactions with the MHCII molecule.[12,13]

Because peptide-MHC binding is necessary for T cell immune responses, developing computational tools to accurately predict binding for any peptide-allele combination has been a major focus of applied immunological research.[14] To this end, a wide range of *in silico* strategies

have been pursued including, machine learning methods using artificial neural networks,[15–20] matrix based methods using position-specific scoring,[21–23] and a number of structure-based methods[24,25] including molecular dynamics.[26] While these methods – and machine learning methods in particular – have significantly improved over the past two decades and can now accurately predict peptide-MHCI binding, their performance for reliably predicting peptide-MHCII binding has lagged behind.[27] The limited accuracy of *in silico* peptide-MHCII binding predictors is largely due to the structural complexities of MHCII antigen presentation. Specifically, it is often difficult to identify the optimal 9mer peptide-binding core within longer peptides. Additionally, the open-ended nature of the MHCII peptide-binding groove allows the peptide considerable conformational freedom, which produces difficult to predict PFR interactions. Further, most machine learning and matrix-based methods require peptide sequences to be of identical length to accurately predict binding to a particular MHCII allele.[28] These methods will therefore underperform when queried with the variable length peptides associated with MHCII binding. In contrast, structure-based peptide-MHCII binding predictors are not limited to identical length peptides, but these methods are generally slower and restricted to the small minority of MHCII alleles with available crystal structures.[29,30]

Given the current limitations of *in silico* peptide-MHCII binding predictors and the fact that the most promising of these methods – namely, machine learning – are trained on experimental binding data, robust experimental assays measuring peptide-MHCII binding are indispensable. A wide range of strategies[31] for assessing and/or quantifying peptide-MHCII binding have been developed including fluorescence polarization assays,[32] ELISA,[33,34] and bead[35] and cell-surface[36] display screening. While each of these experimental assays has its own advantages, the vast majority of peptide-MHCII binding assays use competitive-binding methods

for quantifying peptide-MHCII binding affinity (represented as IC50). These approaches yield high-quality quantitative peptide-MHCII binding data; however, throughput is sacrificed in favor of quantitative detail. Because only a fraction of peptides within a given peptide library will bind a particular MHCII allele, protein and labor will necessarily be wasted on measuring the peptide-MHCII binding affinity for non-binding peptides. Therefore, a preliminary peptide-MHCII screening system designed to strike a balance between throughput and detail should increase the efficiency of more quantitative assays by rapidly segregating binding peptides from non-binding peptides. Such a strategy should also allow the rapid identification of promiscuously binding peptides with potential therapeutic applications. This idea will be discussed in more detail in **Chapter 2.**

1.1.2. T Cell Specificity and Phenotype

The specific MHC-bound peptide recognized by a TCR is called a T cell epitope. Understanding and identifying T cell epitopes is an important aspect of T cell immunity, as it provides insight into antigen processing and presentation that can be used to develop peptide-based vaccines and targeted therapies for a wide range of immunological conditions.[27,37–41] T cell epitope identification began in earnest in 1996 with development of pMHCI tetramers by J. D. Altman and colleagues. In this seminal work, it was shown that biotinylated pMHCI incubated with fluorescently labeled avidin could produce tetrameric reagents for antigen-specific staining of $CD8^+$ TCRs.[42] $CD8^+$ T cells that bound the fluorescently labeled pMHCI tetramers could then be detected and sorted using flow cytometry. This technology was expanded to allow the identification of $CD4^+$ T cell epitopes with pMHCII tetramers in 1999.[43] Since then, a number of technological advances including photo-cleavable[44,45] and enzyme-cleavable[46] peptide exchange,

combinatorial pMHC tetramer staining,[47,48] and T-cell enrichment[46,49] have allowed for the identification of more than 305,000 MHCI-restricted and more than 95,000 MHCII-restricted T cell epitopes, according to Immune Epitope Database and Analysis Resource (IEDB).[50] While the rate of progress has been impressive, it is worth noting that the number of T cell epitopes identified thus far represents only a small fraction of the total T cell repertoire, which is estimated to be at least 2.5×10^7 specificities.[51,52]

In addition to simply identifying T cell epitopes, pMHC tetramer staining also allows the phenotype of antigen-specific T cells to be studied by co-staining T cells with fluorescently-labeled antibodies that bind phenotypic and functional markers on the T cell surface.[37,46,47,53–58] Recently, this strategy has been used to profile T cells that recognize unique antigens arising from tumor-specific DNA-mutations (neoantigens) with the goal of leveraging this tumor-specificity in targeted therapies.[56,59–61]

While pMHC tetramer and phenotypic marker staining is still commonly used for profiling antigen-specific T cells, the number of markers that can be detected simultaneously is inherently limited by overlapping fluorescence spectra. The development of cytometry by time of flight (CyTOF) – which uses isotopically purified heavy metal atoms and mass spectrometry instead of fluorophores and photomultiplier tubes[62] – has allowed the simultaneous detection of more than 40 phenotypic markers on the surface of antigen-specific T cells.[63] This type of deep immune profiling is important for two reasons. First, the high-dimensional datasets acquired from CyTOF experiments have shifted the long-established bottleneck for T cell phenotypic analysis from data collection to data analysis. This shift has produced an interdisciplinary renaissance in immunological research, as sophisticated statistical tools and systems approaches are needed to deconvolute the highly complex data.[64] The second important outcome of high-

dimensional T cell phenotypic profiling by CyTOF, is that these studies have expanded our understanding of T cell subsets[65] and revealed profound relationships between T cell specificity, phenotype, and function.[48,66,67] In a landmark 2012 study, Newell and colleagues used CyTOF to show that $CD8^+$ T cells exhibit much greater phenotypic and functional complexity than previously thought. This complexity provides a large pool of potential $CD8^+$ T cell profiles, allowing virus-specific T cells to exhibit distinct phenotypes and functionalities tailored to the targeted pathogen.[66]

pMHC tetramer staining has produced a wealth of phenotypic and functional data for antigen-specific T cells; however, the pMHC-TCR binding affinity necessary for detection by tetramer staining is significantly greater than the pMHC-TCR binding affinity necessary for T cell activation.[68,69] This difference in affinity threshold is especially important considering that T cells associated with tumor-specific and autoimmune responses tend to bind cognate pMHC with low affinity.[70,71] Further, pMHC tetramer staining has been less successful in the detection of low-frequency antigen-specific $CD4^+$ T cells and rare γδ T cells.[71,72] As a result, a significant fraction of T cell specificities that contribute to a T cell response will not be detected using conventional pMHC tetramer staining. One strategy for overcoming the affinity limitation of pMHC tetramer staining is to engineer more multivalent complexes that promote greater pMHC-TCR binding avidity.[71,72] Multivalent pMHC pentamers, octamers,[73] dextramers,[74–76] and dodecamers[77] have all been shown to increase the sensitivity of T cell epitope detection. Among these highly multivalent molecules, pMHC dodecamers based on the linkage of four streptavidin molecules to a central scaffold have thus far provided the best staining intensity and sensitivity with low non-specific signal.[77] Further applications of highly multivalent pMHC molecules will be discussed in **Chapter 3**, **Chapter 4,** and **Chapter 5**.

1.1.3. T Cell Activation

A T cell immune response is initiated when a TCR binds a cognate pMHC on the surface of an APC. After engaging a cognate pMHC, the immunoreceptor tyrosine-based activation motifs (ITAMs) on the intracellular domains of the TCR-CD3ζ chains are phosphorylated by the tyrosine kinase Lck. The phosphorylated ITAMs then recruit the zeta-chain associated protein kinase 70 (ZAP-70), which promotes further activation signaling by phosphorylating the linker of activated T cells (LAT). The phosphorylated LAT then serves as docking station where signaling complexes assemble and cascade to the T cell nucleus resulting in a transcriptional response (**Figure 1.2**).

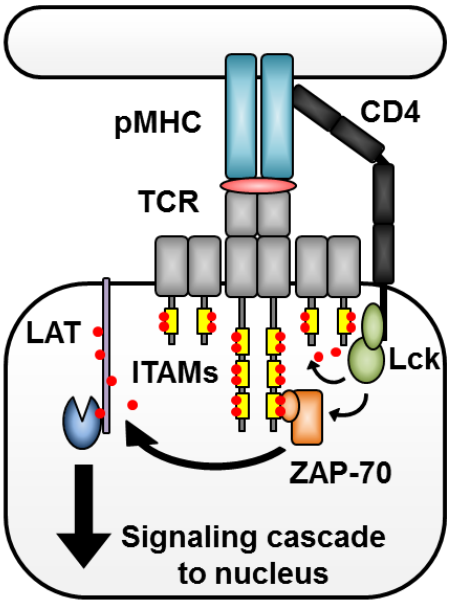

Figure 1.2. Schematic of signaling events that produce T cell activation.

While much is known about the biochemical pathway leading to and following T cell activation, the exact molecular mechanism that links pMHC-TCR binding to ITAM phosphorylation (TCR triggering) has puzzled immunologists for decades. One of the reasons this mechanism has remained elusive is the paradoxical nature of the pMHC-TCR interaction.[78]

pMHC-TCR binding is highly specific and highly sensitive, yet relatively low affinity (K_D ~ 1 – 100 μM) – properties that appear contradictory in the context of protein-protein binding. The enigmatic origin or TCR triggering is problematic because a mechanistic understanding of how T cells are activated is crucial for optimizing large-scale *ex vivo* T cell activation processes for immunotherapy. Three general theories have been proposed to explain TCR triggering: (1) the receptor aggregation model, (2) the receptor deformation model, and (3) the kinetic segregation model.[79]

The receptor aggregation model of TCR triggering postulates that clustering of TCR complexes recruits a critical number of Lck proteins to the immediate proximity of TCR-CD3 ITAMs following pMHC engagement, leading to ITAM phosphorylation and TCR triggering. Early support for this theory came from the observation that multivalent TCR binding via soluble pMHC multimers induced TCR triggering while soluble pMHC monomers did not.[80] It was therefore hypothesized that crosslinked TCRs trapped Lck near the engaged TCR-CD3 complexes, promoting ITAM phosphorylation and TCR triggering. However, it has been difficult to explain how multivalent binding of pMHC can induce TCR-CD3 complex aggregation when agonist pMHC are present at such low densities on the surface of natural APCs.[79] To account for this discrepancy, it was suggested that an agonist pMHC adjacent to a non-agonist pMHC might trigger multivalent TCR engagement via the TCR coreceptor (CD4 or CD8, depending on the T cell type). According to this model, the CD4 or CD8 coreceptor of a proximal but unengaged TCR could bind an adjacent pMHC-TCR complex forming a "pseudodimer" structure.[81] Under these conditions, the proximity of the coreceptors and their associated Lck proteins[82,83] to the engaged TCR ITAMs could be sufficient to drive ITAM phosphorylation and TCR triggering. While this model is consistent with the striking observation that non-agonist pMHC significantly

enhance TCR recognition of agonist pMHC for $CD4^+$ T cells,[84] it does not explain how TCR triggering can occur in the complete absence of co-receptors.[85,86]

Another set of theories suggests that TCR triggering is not caused by receptor aggregation alone, but instead by mechanical force transmitted to the TCR following pMHC binding.[87–91] These receptor deformation models postulate that pMHC-TCR binding coupled with cell movement applies tensile and shearing forces to the TCR sufficient to induce a conformational change in the TCR-CD3 complex that favors activation. Direct evidence of conformational changes in the TCR-CD3 complex has been reported;[92,93] however, the significance of these changes with respect to TCR triggering has yet to be shown. One theory that supports the receptor-deformation hypothesis is the safety-catch model of TCR triggering.[94,95] The safety-catch model proposes that basic residue rich sequences (BRS) of the TCR-CD3 ITAMs have a tendency to associate with acidic lipid vesicles in the plasma membrane. Thus, under normal non-activating conditions, TCR-CD3 ITAMs are buried in the membrane and protected from phosphorylation. When an agonist pMHC is bound, the pMHC-TCR binding event causes a conformational change in the CD3 cytoplasmic domain that allows the ITAMs to dissociate from the plasma membrane (safety-off), thus exposing them to phosphorylation by neighboring Lck.[94,95] While elegant and supported by experiment data, this theory cannot explain the fact that treating T cells with phosphatase inhibitor causes a significant increase in ITAM phosphorylation in the absence of receptor engagement.[96] More recently, it has been suggested that TCR triggering may be a result of the cumulative effect of catch bonds between pMHC and TCR.[97] In a 2014 study, it was shown that weak-agonist pMHC have high on and off rates, which allows TCRs to rapidly sample pMHCs via slip bonds. In contrast, strong-agonist pMHC – which have slower off rates – transmit force to the receptor through the

formation of a catch bond. In this study, the magnitude, duration, and frequency of the force applied to the TCR by the bound pMHC directly influenced intracellular Ca^{2+} flux, an early hallmark of TCR triggering. This model is consistent with the finding that mechanical force on the TCR can produce TCR triggering.[91] However, it should be cautioned that nearly any surface-displayed protein-protein interaction will result in the application of some mechanical force on the engaged receptors, yet not all biochemical reactions that follow are directly caused by that application of force. Further, receptor aggregation and mechanical force on the TCR are not mutually exclusive events, and both phenomenon could occur in the course of TCR triggering.[98]

The final – and currently most well supported – theory of TCR triggering is related to the segregation and redistribution of T cell membrane proteins following pMHC-TCR binding. According to the kinetic-segregation theory of TCR triggering, a homeostatic equilibrium exists between kinase and phosphatase activity on the TCR-CD3 ITAMs by Lck and CD45/148, respectively. This equilibrium is disrupted when pMHC-TCR binding reduces the distance between the APC and T cell surfaces to ~14 nm.[99] Because CD45 and CD148 have large ectodomains (28 – 51 nm for CD45 and ~55 nm for CD148),[100,101] proponents of the kinetic-segregation model suggest that these phosphatases are segregated from the close-contact zone of the pMHC-TCR complex and redistributed to the periphery to better accommodate their large size.[102] This segregation of the phosphatases from the ITAMs of the engaged TCR-CD3 complex tilts the local kinase-phosphatase balance in favor of ITAM phosphorylation. The kinetic-segregation model is well supported by several independent lines of evidence. First, approximately 40% of Lck in resting T cells is constitutively active, and no significant increase in Lck activity is observed following pMHC-TCR engagement.[103] This suggests that pMHC-TCR binding is not required to activate Lck, and therefore, triggering must occur in the context

of constant phosphorylation activity. Second, it has been shown that truncating the CD45 ectodomain in T cells restricts CD45 exclusion and inhibits TCR triggering.[104] This finding was further supported in an elegant 2012 study in which it was shown that pMHC-TCR binding alone is necessary and sufficient to drive CD45 segregation and TCR triggering.[105] Finally, the kinetic-segregation model is supported by the well-established finding that surface-bound pMHC produces more effective TCR triggering than soluble pMHC, and that elongating surface-bound pMHC molecules inhibits TCR triggering.[106,107]

Regardless of the precise molecular mechanism of TCR triggering, pMHC-TCR binding is followed by the repopulation of the T cell-APC interface with a number of costimulatory molecules and their respective ligands. The cumulative structure of costimulatory molecules at the junction of the engaged T cell and APC is called the immunological synapse, and signaling from this structure promotes T cell activation and helps determine T cell response.[108] The traditional model of the immunological synapse is a bulls-eye pattern in which agonist pMHC-TCR and the costimulatory B7-1/2-CD28 interaction form the central supramolecular activation cluster (cSMAC). This central cluster is enriched in Lck favoring TCR-CD3 ITAM phosphorylation.[109] The peripheral supramolecular activation cluster (pSMAC) surrounds the cSMAC, and is populated by complexes between intercellular adhesion molecule 1 (ICAM-1) and lymphocyte function associated antigen 1 (LFA-1), in addition to the CD4 coreceptor for $CD4^+$ T cells. CD45 phosphatase is thought to be segregated outside the pSMAC in the distal supramolecular activation cluster (dSMAC) early in TCR signaling due to its relatively bulky ectodomain. In the absence of costimulatory molecules, a mature immunological synapse does not develop, and T cells exhibit an anergic phenotype.[110,111] In this state, T cells do not proliferate, secrete IL-2, or become stimulated following additional pMHC-TCR interactions. T

cell anergy is thought to play a role in limiting T cell immune responses to prevent autoimmune diseases.[111] As a result, induction of antigen-specific T cell anergy of self-reactive T cells is being pursued for the treatment of autoimmune conditions.[112]

In addition to promoting T cell activation and immunological synapse formation, costimulatory signaling also influences T cell phenotype and function.[113–117] Therefore, modulating costimulatory and inhibitory molecule signaling can be used to tailor the properties of T cells for specific therapeutic applications. Early studies of T cell activation reported pMHC-TCR and B7-1/2-CD28 binding as the minimum requirements for antigen-specific T cell activation.[110] CD28 signaling promotes T cell survival, expansion, and cytokine secretion,[118] while also stimulating Lck activity.[119] In addition to the well-established importance of the B7-1/2-CD28 interaction, ICAM-1-LFA-1 binding is also thought to play an important role in T cell activation. While the ICAM-1-LFA-1 interaction has traditionally been associated with cell adhesion,[120] recent studies have shown that LFA-1 stimulation modulates T cell gene expression and can promote differentiation into Th1, Th17, and regulatory (Treg) phenotypes.[115] Further, ICAM-1-LFA-1 signaling sustains elevated levels of intracellular calcium during pMHC-TCR binding and promotes the expansion of proliferation-competent memory T cells.[121,122] The costimulatory role of ICAM-1-LFA-1 binding will be explored further in **Chapter 3**. Another important costimulatory interaction – especially in the context of an anti-tumor T cell response – is 4-1BBL-4-1BB. Recent studies have shown that 4-1BB signaling is more effective than CD28 signaling for ameliorating T cell exhaustion in therapeutic chimeric antigen receptor (CAR)-T cells.[116] In addition, 4-1BBL-4-1BB binding is thought to play an important role in enhancing tumor-specific cytotoxicity by preferentially expanding memory T cells.[123–125]

Costimulatory signals do not act independently, and T cell costimulation in the body involves multiple molecules with complex spatial and stoichiometric organizations. It has been shown that a combination of both CD28 and 4-1BB signaling is superior for the long term propagation of $CD8^+$ T cells than either signal alone.[126] Similarly, the presentation of various combinations of ICAM-1, B7-1 (CD80), B7-2 (CD86), and 4-1BBL improves T cell proliferation and activation compared to presentation of each individual molecule.[126–128] The importance of costimulatory ligand stoichiometry was further highlighted in an experiment designed to study cytotoxic T-lymphocyte-associated protein 4 (CTLA-4), an inhibitory analog of B7-1/2. Here it was shown that not only could CTLA-4 outcompete CD28 for B7-2 binding,[129] but also that CTLA-4 could capture bound B7-2 from the opposing cell surface via trans-endocytosis. Interestingly, the researchers showed that a 1:8 stoichiometric ratio of CTLA-4:B7-2 was sufficient for the complete functional depletion of B7-2 from the APC surface.[130]

1.2. T Cell Immunotherapy

Autoimmune disease, cancer, and chronic viral infections all arise from a breakdown in the activation and function of antigen-specific T cells. In autoimmune disease, T cells are generally overactive, targeting self-antigen on healthy cells and causing significant damage to host tissue. In contrast, cancer and chronic viral infections persist from of a fundamental failure of T cells to recognize and destroy tumor and infected cells, respectively. One reason for this failure, especially in solid-tumor cancers, is widespread immunosuppression in the tumor microenvironment. Tumor metastasis occurs, in part, by evading immune detection using a variety of soluble (*e.g.* IL-10 and TFG-β) and surface displayed (PD-L1) immunosuppressive

signals. These signals facilitate immune tolerance by, for example, promoting the expansion of tolerant Treg phenotypes.[131–133]

To circumvent ineffective T cell activation within immunosuppressive environments, tumor-specific T cells can be isolated, engineered, and expanded *ex vivo* in the presence of signals that promote a more effective T cell phenotype. This process of modulating T cell phenotype and function to achieve a better clinical response is called T cell immunotherapy. As our understanding of T cell biology has improved, T cell immunotherapy has gained traction as an effective alternative to conventional therapies, and should continue to do so well into the future (**Figure 1.3)**. While T cell immunotherapy has been studied and applied to autoimmune conditions[134–137] and chronic viral infections,[138–142] the primary application of T cell immunotherapy has been in the treatment of a variety of cancers.[143,144] Therefore, we will largely focus on T cell immunotherapy in the context of cancer.

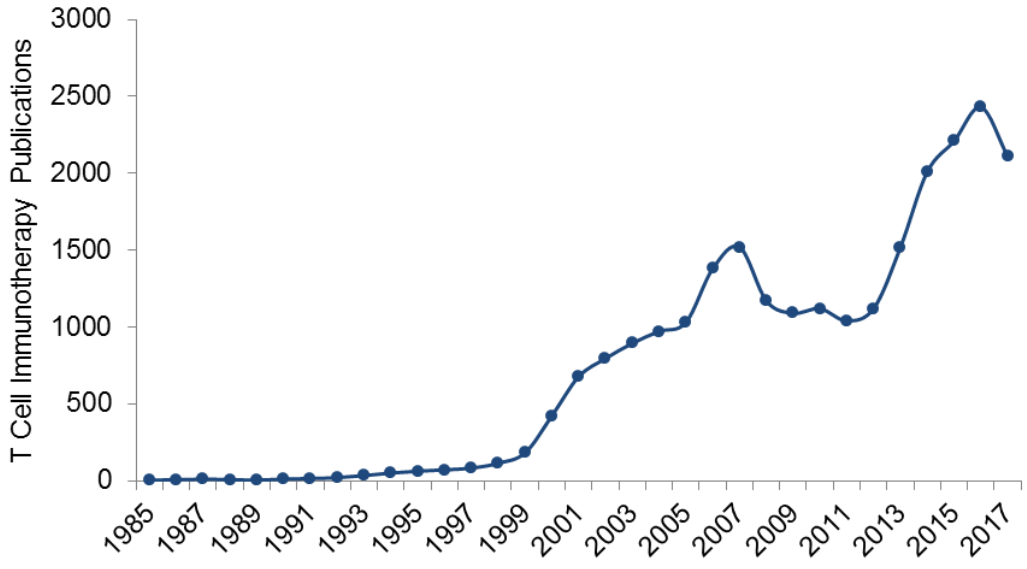

Figure 1.3. Academic publications related to T cell immunotherapy since 1985.
Number of articles containing the words "T cell immunotherapy" published in academic journals each year since 1985. Publication counts were determined using Google Scholar.

The first demonstrated successes of T cell immunotherapy were achieved in the mid-1980s by S.A. Rosenberg's research group at the National Cancer Institute. In 1986, Rosenberg and colleagues showed that tumor infiltrating lymphocytes (TILs) harvested from a tumor and expanded *ex vivo* in the presence of IL-2 could mediate tumor regression in the lungs and livers of mice, in conjunction with cyclophosphamide.[145] Shortly after this finding, *ex vivo* expanded TILs were used in human trials[146] and shown to mediate tumor regression in the lungs, liver, bone, and skin of up to 60% of patients with metastatic melanoma.[147] By 2002, highly specific TILs expanded *ex vivo* and re-infused in patients with advanced melanoma were shown to mediate tumor regression by exhibiting potent activity toward a self-antigen associated with melanoma (MART-1).[148] This study demonstrated that *ex vivo* expanded TILs recognizing self-antigen could persist *in vivo*, and suggested that the adoptive transfer of similar TILs could be used to treat a variety of common cancers. While early trials with *ex vivo* expanded TILs highlighted the incredible potential of T cell immunotherapy, these studies also revealed significant limitations of this approach. First, TILs need to be harvested from solid tumors, and not all tumors are resectable – that is, not all tumors can be safely accessed for harvesting TILs. Further, many tumors that are resectable do not yield appreciable TILs. These limitations led to the realization that universal approaches and/or off-the-shelf therapeutic T cells would be necessary for T cell immunotherapy to be widely applicable and cost-effective.[149]

1.2.1 Transgenic TCRs

The necessity of universal approaches to T cell immunotherapy inspired researchers to identify TCRs that recognize common tumor-specific T cell epitopes. Once identified, TCRs recognizing these tumor-specific epitopes can be expressed in autologous T cells to establish off-

the-shelf therapeutic T cells tailored for different types of cancer.[150] For example, T cell lines expressing TCRs that recognize melanoma-associated antigens could be established and used to treat skin cancer. Similarly, T cell lines recognizing additional tumor-associated antigens could be established and used to treat other common types of cancer. The first demonstration that T cells engineered to express tumor-specific transgenic TCRs could mediate tumor regression in advanced melanoma patients was reported in 2006 using the HLA-A2 restricted MART-1_{27-35} epitope.[151] This work showed that not only could T cells expressing transgenic TCRs persist *in vivo*, but that these T cells could mediate full clinical regression of metastatic melanoma in humans. Additional studies using transgenic TCRs recognizing common tumor associated antigens – primarily NY-ESO-1, MART-1, and several melanoma associated antigens (MAGE) – have improved on this initial success,[152–156] and a number of clinical trials are ongoing.[149]

Despite success in the treatment of melanoma, transgenic TCR immunotherapy is limited by the fact that many solid tumors down-regulate antigen presentation machinery including MHC molecules.[157] Further, even when antigen presentation machinery is functional, tumors presenting the most common tumor associated antigens are often cleared by the immune system early in the disease. This elimination of immunogenic tumor cells exerts a selective pressure, allowing less immunogenic tumors to escape in a process called immunoediting.[158] Tumor escape through immunoediting has inspired researchers to study neoantigens produced by unique mutations using whole-exome sequencing of tumor cells. While this is a relatively novel approach, early results have indicated that T cell recognition of patient-specific neoantigens is an important factor in the success of clinical immunotherapy.[60,61] The growing importance of neoantigens in cancer immunotherapy casts doubt on the therapeutic potential of off-the-shelf T cells expressing transgenic TCRs that recognize generic tumor associated antigens.

Another challenge associated with T cells expressing transgenic TCRs for immunotherapy is the potential for off target activity. In one case, 3 of 9 patients injected with T cells expressing a transgenic TCR recognizing the melanoma antigen (MAGE)-A3, experienced significant mental health changes within 48 hours of injection. Two of these patients lapsed into comas and subsequently died while the third recovered but experienced Parkinson's like symptoms over four weeks. Molecular analysis of human brain samples revealed that neurons in the brain expressed MAGE-A12, which cross-reacted with the transgenic MAGE-A3-specific TCRs.[159] Off-target cardiovascular toxicity has also been observed with transgenic MAGE-A3-specific TCRs; however, in this case the cardiovascular tissue targeted did not express any MAGE antigen. Instead, the cardiac tissue presented a peptide derived from the striated muscle-specific protein titin, which bound HLA-A1 and was molecularly similar to the MAGE-A3 T cell epitope.[160] Finally, transgenic TCR therapy is limited to patients that both have tumors that present the target antigen and also match the haplotype restriction of the engineered TCR.[149]

1.2.2. Chimeric Antigen Receptor (CAR) T cells

The idea to expand T cell immunotherapy beyond MHC-restricted antigenic targets was first introduced by Japanese researchers[161] at the Institute for Comprehensive Medical Science in Toyake in 1987 and more thoroughly explored by Israeli researchers[162] at the Weizmann Institute of Science in 1989. There, Eshhar and colleagues engineered T cells to express a fusion protein consisting of the variable domain of an antibody and the constant domain of a TCR. These modified T cells exhibited antibody -like specificity while retaining the ability to transmit signals that produce T cell activation.[162] Eshhar and colleagues modified this novel surface receptor into a single chain in 1993 by fusing an antibody single-chain variable fragment (scFv) recognizing a

target antigen to the intracellular CD3ζ chain.[163] T cells expressing the resulting fusion proteins were initially called "T-bodies" – a combination of T cell and antibody – but would become more widely known as chimeric antigen receptor (CAR) T cells.

The first generation of CAR T cells were relatively simple and closely resembled the initial "T-body" design of an extracellular scFv fused to an intracellular CD3ζ chain. While promising in theory, the preliminary results of first-generation CAR T cells designed to target ovarian and renal cancers, lymphomas, and neuroblastomas were disappointing due to limited *in vivo* persistence and modest activity.[164] These initial limitations were overcome by engineering a second generation of CAR T cells, which included the scFv and CD3ζ domains of the first generation fused to either the 4-1BB or CD28 endodomain.[165,166] In a series of 2009 studies, June and colleagues demonstrated that CAR T expressing an engineered receptor containing the 4-1BB endodomain survived longer *in vivo* and exhibited significantly greater activity against leukemia in tumor-bearing mice than first generation CAR T cells.[167] In a follow up study, June and colleagues further demonstrated that anti-mesothelin CAR T cells containing both the 4-1BB and CD28 endodomains persisted longer *in vivo* and exhibited more potent anti-tumor activity than CAR T cells expressing either the 4-1BB or CD28 endodomain alone.[168] At almost the same time, Rosenberg and colleagues found that second generation CAR T cells recognizing the B-cell surface antigen CD19 could achieve the complete regression of B cell lymphomas in human patients.[169]

The initial success of second generation CAR T cells in treating $CD19^+$ hematological cancers was proven durable in a series of subsequent studies,[170–173] and in 2017 the first CD19 CAR T cell therapies were approved by the U.S. FDA. The first of these therapies, tisagenlecleucel-T (Kymriah; Novartis), was FDA approved for treating children and young

adults (up to age 25) with relapsed or refractory acute lymphoblastic leukemia (ALL), and is currently being considered for use in other $CD19^+$ hematological cancers. Within months of the approval of Kymriah, the FDA approved a second CAR T cell therapy, axicabtagene ciloleucel (Yescarta; Kite Pharma/Gilead Sciences), for the treatment of relapsed or refractory B cell lymphoma. The alacritous approval of these new therapies was well founded – within months of infusion, 83% of patients treated with Kymriah CAR T cells and 51% of patients treated with Yescarta CAR T cells experienced complete remission.[174] While these results are undoubtedly impressive, the approved CAR T cell therapies are the most expensive oncology therapies to date, with list prices of $475,000 for Kymriah and $373,000 for Yescarta. A major reason for the exorbitant costs of these therapies is that, like transgenic TCR therapies, the FDA approved CAR T cell therapies rely on genetically modifying autologous T cells. Reducing the cost will therefore require off-the-shelf CAR T cells, though whether such cells will be able to deliver the same level of safety and efficacy as autologous CAR T cells remains to be seen.[174]

The overwhelming success of second-generation CAR T cells in eradicating hematological cancers demonstrated two things. First, it showed that CAR T cell therapy is incredibly effective when it can be directed at clear antigenic targets (i.e. CD19). Second, it established that costimulatory T cell signaling is indispensable for promoting T cell survival *in vivo* and sustaining anti-tumor activity. Despite the promise of second-generation CAR T cells, several important challenges remain. Like transgenic TCRs, CAR T cells are prone to over-activity and off-target activity if the target antigen is not unique to cancer cells. However, because CAR T cells bind their cognate antigen with high affinity, this over-activity can lead to a life threatening inflammatory response called cytokine release syndrome (also known as a "cytokine storm).[175,176] Further, while CAR T cell therapies have been successful against

hematological cancers like leukemia and lymphoma, similar therapies targeting solid tumors have been much less effective.[177] This is due in part to the immunosuppressive nature of the tumor microenvironment and clinical trials investigating CAR T cell therapy in conjunction with PD-1/PD-L1 blockades are ongoing.[166] However, the single greatest challenge in applying CAR T cell therapy to solid tumors is the selection and frequent loss of appropriate antigenic targets on tumors. Cancer cells are notoriously fickle and evade targeted therapies via immunoediting and downregulating the expression of surface antigen.[178] The difficulty of overcoming immune evasion was highlighted recently when CAR T cells targeting a tumor associated variant of epidermal growth factor receptor (EGFRvIII) in patients with glioblastoma resulted in tumor-antigen loss and adaptive resistance.[179]

1.2.3. T Cell Immunotherapy Challenges

The T cell immunotherapy strategies described hitherto have achieved considerable success in the past two decades. However, serious challenges must be overcome for T cell immunotherapy to reach its full clinical potential. Identifying and selecting appropriate antigenic targets – particularly on solid tumors – is among the most significant of these challenges. Most antigens presented on solid tumors are also expressed on healthy cells. This is a serious concern, especially with CAR T cell therapies, in which off target activity can produce life threatening cytokine storms. In fact, minimizing off-target activity is currently the primary factor in the selection of CAR T cell antigenic targets.[180] The desire to minimize off-target activity has led researchers to target unique tumor-specific antigens. However, identifying, isolating, and expanding a clinically relevant number of T cells recognizing neoantigens is difficult, as these T cells represent as little as 0.002% of the peripheral T cell population prior to therapy.[56] In

addition, the targeting of neoantigens is problematic for CAR T cells, as many neoantigens are derived from intracellular proteins and their presentation is MHC restricted.[180]

Further, all of the discussed T cell immunotherapy strategies involve the *ex vivo* expansion of autologous T cells. T cell phenotype and function change following repeated stimulation and often exhibit significantly reduced proliferative capacity, which negatively correlates with the treatment efficacy.[143] A number of studies have demonstrated that proliferative capacity and functionality *in vivo* can be enhanced by carefully modulating the costimulatory and soluble signals delivered to T cells during *ex vivo* activation.[116,181] However, data regarding the optimal combination of costimulatory signals to maximize *in vivo* efficacy are scarce. Achieving a comprehensive understanding of how T cell costimulation translates to therapeutic efficacy will require new modular tools capable of precisely organizing signals presented to T cells during activation. Systematic investigation of T cell activation using such tools should allow the full characterization of the T cell activation design space. This characterization should also help identify and evaluate biomarkers that predict success *in vivo.*

1.3. Artificial Antigen Presentation

While autologous APCs have traditionally been used in clinical environments for safety reasons, these cells are not always available or desirable for *ex vivo* T cell expansion. Expanding different T cell types requires different molecular signals that may not be present on autologous APCs. Further, maintaining multiple cultures of autologous APCs under different conditions for each patient and/or application is laborious and expensive. For example, sipuleucel T (Provenge; Dendreon Corporation) is an FDA approved therapy that involves culturing autologous APCs with a stimulatory fusion protein containing a peptide associated with prostate cancer. While

sipuleucel T was shown to increase the median survival time of patients by 4.1 months,[182] the treatment comes at a cost of approximately $93,000.[183] The high cost of sipuleucel T is reflective of the labor-intensive process of culturing autologous APCs. Reducing the costs and increasing the accessibility of T cell immunotherapy will therefore require universal systems capable of delivering stimulatory and costimulatory signals to T cells using off-the-shelf components.

Artificial antigen presentation seeks to reconstitute the fundamental features of APCs – namely, stimulatory TCR ligands and costimulatory molecules – on an artificial or engineered cell surface. Artificial antigen presentation systems thus represent a cost-effective, scalable, and tunable technology for optimizing *ex vivo* T cell activation and expansion. A wide variety of artificial antigen presentation systems have been engineered thus far,[184] including planar 2D systems, engineered cellular systems, and 3D acellular systems. The most appropriate artificial antigen presentation strategy depends on the specific application, and together they have greatly improved our understanding of how T cell phenotype and function can be influenced by modulating stimulatory and costimulatory signaling during T cell activation.

1.3.1. 2D Artificial Antigen Presentation Systems

2D artificial antigen presentation systems are the most tunable type of artificial antigen presentation system, as they are amenable to a wide range of patterning techniques and conjugation chemistries. 2D artificial antigen presentation systems can be described as either static or dynamic, depending on the mobility of the presented ligands. Static presentation systems use lithographic patterning of anchor points (usually metal or organic nanoparticles) to immobilize T cell ligands on a surface. In contrast, dynamic presentation systems embed ligands in fluid lipid bilayers. While each system has its advantages and disadvantages, both are

powerful and customizable platforms for studying the molecular organization of proteins during T cell activation.

The most successful static presentation systems involves di-block micelle assisted lithographic patterning of gold nanoparticles.[185] Lithographic surface patterning with gold nanoparticles allows the spatial organization of T cell ligands to be controlled with nanoscale precision. Using this approach, it was shown that T cell activation can be finely tuned by modulating both the surface density and intermolecular spacing of TCR-ligands.[186–188] In addition, it was recently shown that lithographic patterning can achieve single molecule occupancy on each patterned nanoparticle, providing unprecedented control over the spatial organization of individual proteins.[189] Similarly, lithographically patterned surfaces have also been used to show that T cell activation is enhanced when costimulatory molecules (in this case anti-CD28 antibodies) are segregated from TCR ligands.[190,191] More recently, all-organic lithographic patterning has enabled the live-cell imaging of T cells interacting with patterned proteins by total internal reflection and reflection interference contrast microscopy.[192] Using this approach, researchers observed that while TCR clustering is driven by the nanoscale organization of TCR ligands, the cell-scale response as measured by T cell adhesion and spreading is determined by the global antigen density.[193] Taken together these studies indicate that T cells recognize the organization of T cell ligands at the molecular level, as well as their overall surface density. Further, these reports suggest that T cells integrate spatially complex multi-scale signals, which shape the functional T cell response. The precision of patterns created using lithography is not attainable in cell-cell or dynamic 2D systems. Therefore, static 2D artificial antigen presentation systems represent a highly tunable platform for investigating how

the nanoscale organization and geometry of immobilized T cell ligands influences T cell activation.[194]

The primary disadvantage of static presentation systems using lithographic patterning is that they do not allow the patterned proteins to move or reorganize during T cell activation. For applications that require dynamic antigen presentation, T cell ligands are presented in fluid lipid bilayers,[195] which allow lateral mobility of the embedded T cell ligands during T cell activation. A number of different 2D artificial antigen presentation systems using fluid lipid bilayers have been engineered, and studies using these systems tend to emphasize the importance of ligand mobility in immunological synapse formation and T cell activation.[194] For example, when T cell ligands were embedded in fluid lipid bilayers of heterogeneous membrane fluidity, it was found that T cell activation and immunological synapse formation were notably weaker in less mobile membranes than more mobile membranes.[196] Interestingly, additional studies found that when pMHC was embedded in fluid lipid bilayers containing barriers to restrict ligand mobility, T cell activation was sensitive to the number of pMHC within individual corrals[197] and was greatest when pMHC and TCR clusters were mechanically trapped at the periphery of the cSMAC.[198] While the latter result was counterintuitive based on the traditional understanding of the immunological synapse as a bulls-eye pattern, it nonetheless supports the notion that T cell activation can be modulated by controlling the spatial organization of T cell ligands. 2D artificial antigen presentation systems using fluid lipid bilayers have also provided compelling evidence in support of the kinetic-segregation theory of TCR triggering, which has important implications in the design of future artificial antigen presentation systems.[104,105,199] For example, if CD45 exclusion is necessary to sustain stimulatory Lck and ZAP-70 activity, artificial antigen presentation systems incorporating surface displayed supramolecular assemblies should consider

how assembly size might restrict CD45 exclusion. This idea will be discussed in more detail in **Chapter 4** and **Chapter 5**. Despite their demonstrated success as research tools, the relatively short shelf-life of dynamic 2D antigen presentation systems limits their potential applications.[200] In addition, because artificial fluid membranes lack cytoskeletal components, proteins tend to aggregate within these bilayers in the absence of membrane organizers.[201]

While 2D artificial antigen presentation systems provide unparalleled control over the spatial organization of T cell ligands, these systems are not scalable for large-scale *ex vivo* T cell activation. Further, while the interface between T cells and natural APCs is often described as 2D, it is not clear if T cells primed on a 2D surface will integrate stimulatory and/or costimulatory in the same way as 3D surfaces like natural APCs. For example, 2D artificial antigen presentation systems exhibit a constant polarity with respect to the orientation of the presented antigen, while natural APCs like dendritic cells do not. This constant field of uniform antigen on 2D surfaces may underestimate the importance of adhesion and costimulatory molecules, which stabilize the T cell-APC interface and enhance TCR signaling. The differences between 2D and 3D artificial antigen presentation systems will be discussed in more detail in **Chapter 3.**

1.3.2. Cell-based and 3D Acellular Artificial Antigen Presentation Systems

Like dynamic 2D artificial antigen presentation systems, cellular artificial antigen presentation systems generally present antigen in the context of fluid membranes, allowing ligand mobility and immunological synapse formation. However in contrast to 2D systems, cellular artificial antigen presentation systems present T cell ligands on a living cell surface with active cytoskeletal components, which reduces unnatural protein aggregation and more

accurately represents natural antigen presentation. Another significant advantage of artificial antigen presenting cells (aAPCs) is that once a desired aAPC is engineered, it can be cloned and cryopreserved for extended periods of time. Cryopreservation of well-characterized aAPC clones is not only convenient, but also helps ensure batch-to-batch consistency, which is an important consideration in the application of off-the-shelf aAPCs in a clinical environment. In addition, cellular systems generally lack protein purification steps and are relatively stable under physiological conditions.

aAPCs have been successfully engineered using four cellular platforms: yeast cells,[202] insect cells,[203–205] fibroblast cell lines,[206–208] and leukemic cell lines.[126,127,209] Of these various cellular platforms, the human leukemic cell line K562 has been among the most popular for artificial antigen presentation, as K562 cells do not express native MHC molecules but do express an array of adhesion molecules present on natural APCs. Engineered K562 aAPCs expressing various combinations of costimulatory molecules allowed the expansion of distinct T cell phenotypes.[126] Importantly, this result suggests that custom aAPCs expressing different molecules can be tailored for the optimal expansion of desired T cell subsets.[126] Despite providing a more physiologically accurate surface for presenting antigen to T cells, aAPCs generally provide much less control over the spatial and stoichiometric organization of T cell ligands. In addition, while clinical grade aAPCs based on leukemic cell lines have worked well in small-scale research environments, many medical professionals have reservations about infusing T cells and aAPCs derived from a malignant cell line into cancer patients.[210]

In contrast to cellular artificial antigen presentation systems, 3D acellular artificial antigen presentation systems pose little risk of immunological complications (e.g. graft vs. host disease)[211] when used with primary T cells. The first 3D acellular artificial antigen presentation

systems were designed using sepharose[212,213] and polystyrene beads.[214,215] These initial systems laid the groundwork for a second generation of tunable 3D artificial antigen presentation platforms based on magnetic particles[216] and a range of biocompatible polymers,[217,218] and liposomes.[219–221] More recently, advanced acellular artificial antigen presentation systems using highly multivalent soluble complexes[222–224] and nanoparticles[225–227] have been engineered and have significant potential as biocompatible therapeutics that can be delivered *in vivo*.

Currently, the most widely used system for activating and expanding T cells are Dynabeads™, which are 4.5 μm diameter beads covalently coupled to anti-CD3 and anti-CD28 antibodies.[228] Recently, the Dynabeads™ system has been updated to include anti-CD137 (4-1BB) antibodies as well, as a result of the increasingly understood importance of 4-1BB signaling for T cell survival and proliferation.[116] While these bead-based systems have been effective for expanding a clinically-relevant number of antigen-specific T cells *ex vivo*,[229] they provide little to no control over the spatial organization of T cell ligands. In addition, these systems have been associated with poor biocompatibility *in vivo* as the small particles are susceptible to entrapment in lung capillaries.[230–232] Liposomes and biodegradable particles could prove to be an effective alternative for *in vivo* immunotherapy; however, these materials are less stable than polymeric beads[231] and sustained antigen presentation in vivo or during long-term cell culture could be problematic.

1.4. Project Overview

T cell immunotherapy represents a powerful and promising approach for the treatment of a wide range of immunological conditions. However, the continued success of T cell immunotherapy will require a more thorough understanding of T cell activation and cost-

effective tools for controlling the T cell activation process. The central theme of this dissertation is the development and application of molecular tools for isolating and activating antigen-specific T cells, with direct applications to T cell immunotherapy. Because this is an inherently broad topic, I have organized the following discussion around three sub-themes, which will be discussed in **Chapter 2**, **Chapter 3**, and **Chapter 4**, respectively (**Figure 1.4**).

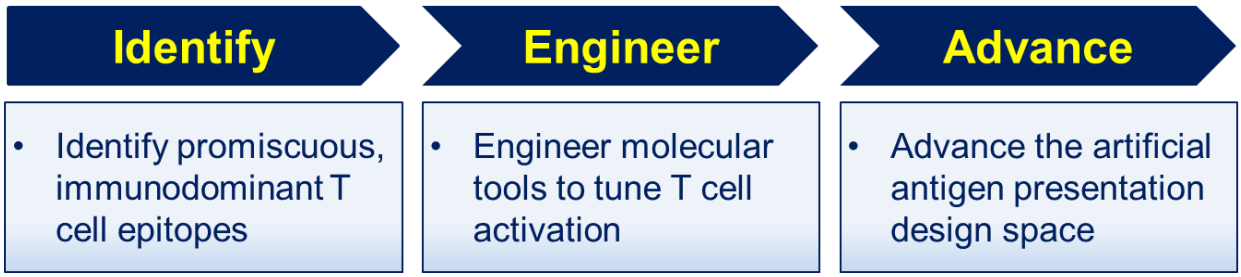

Figure 1.4. Organization of dissertation.

The second chapter of this dissertation will introduce a high-throughput strategy for rapidly identifying promiscuous peptide-MHCII interactions. This strategy – which we have called microsphere-assisted peptide screening (MAPS) – aims to strike a balance between throughput offered by *in silico* prediction algorithms and quantitative detail offered by competition-based binding assays. By screening a reference peptide library with known binding affinity to four common MHCII alleles, we found that the *in silico* prediction algorithms recommended by IEDB were poor predictors of peptide-MHCII binding, achieving an AUC of only 0.632 compared to 0.851 for MAPS. Using MAPS, we then identified seven peptides within the rotavirus VP7 protein and six peptides within the Zika virus envelope (E) protein that bound to all four MHCII alleles tested. Interestingly, we also found that these promiscuously binding peptides overlapped significantly with antibody neutralization sites on each respective protein, indicating that these are immunodominant regions. In addition, we observed that the MAPS

signal is sensitive to the relative position of the peptide-binding core within the peptide. While unexpected, the sensitivity of the MAPS signal to the relative core position should allow for more accurate binding core identification when MAPS is used in conjunction with other quantitative peptide-MHCII binding assays. Although the peptide-MHCII screening strategy described in **Chapter 2** was performed using peptide libraries derived from viral proteins, the same approach could be applied to screening neoantigen libraries for the design of potential peptide-based cancer vaccines and therapeutics.[40]

The third chapter of this dissertation will describe a method for using high-affinity protein-protein binding to control the spatial and stoichiometric organization of T cell ligands on a 3D yeast cell surface. Using these yeast antigen-presenting cells (yAPCs), we explored the role of overall ligand surface density, ligand valency, and costimulatory molecule display ratio on T cell activation. Interestingly, we observed that the T cell activation threshold is independent of local pMHC density – with or without costimulatory molecules – however, in the absence of costimulation T cells require six-fold greater pMHC surface density for activation. Further, we observed that T cell IL-2 secretion is maximized at a display ratio of 15% pMHC and 85% ICAM-1. The systematic investigation of T cell activation described in **Chapter 3** could be repeated for additional costimulatory molecules to provide a more comprehensive understanding of how T cells integrate signals, and how combinatorial costimulation affects T cell phenotype and function.

The fourth chapter of this dissertation will describe potential strategies for advancing the artificial antigen presentation design space using surface displayed 2D multi-scaffold assemblies. These supramolecular assemblies are based on scaffold-scaffold complex formation, where an anchor scaffold (aScaf) displayed on the yeast cell surface binds a soluble primary scaffold

(pScaf) by *in vitro* loading. By engineering multi-scaffold complexes, both the valency and the spatial organization of multiple ligands can be controlled simultaneously and with nanoscale precision. However, before directly applying this approach to tuning T cell activation, we sought to understand how these large complexes assemble, what parameters affects their overall assembly efficiency. To this end, we developed a theoretical and quantitative approach for characterizing each aspect of the assembly process. Interestingly, we found that the assembly efficiency of these multi-scaffolded complexes is inherently limited by crowding effects on the cell surface. These crowding effects were most prominent for the largest aScafs, which suggest that assemblies are created via "outside-in" pScaf loading. While these results are presented in the context of whole-cell biocatalysis, the mechanistic insights into protein-scaffold directed assembly is equally applicable to the design of highly ordered T cell ligand assemblies in the future.

Finally, the dissertation will conclude with a brief summary of ongoing work as well as potential future directions for these projects in **Chapter 5**.

Chapter 2. Rapid Identification of Promiscuous Peptide-class II MHC Interactions Using Microsphere Assisted Peptide Screening (MAPS)

2.1. Publication Information

Smith, M. R., Wen, F. Rapid identification of promiscuous peptide-class II MHC interactions using microsphere assisted peptide screening (MAPS). (*In Prep*)

The goal of this chapter is to develop and validate a high-throughput screening strategy for evaluating peptide-class II MHC interactions. Specifically, we aimed to develop a new peptide-MHC screening strategy that strikes a balance between the throughput offered by computational peptide-MHC binding predictors and the quantitative detail offered by competition-based peptide-MHC binding assays.

2.2. Abstract

A robust $CD4^+$ T cell response is predicated on stable peptide-MHCII binding; however, predicting if an antigenic peptide will bind to a specific MHCII protein is a significant challenge. Despite promising developments in computational tools, peptide-MHCII binding predictors continue to lag behind their peptide-MHCI counterparts. The comparatively disappointing performance of peptide-MHCII binding predictors is largely a result of three factors: the significant allelic diversity of MHCII and the role of this allelic diversity in influencing peptide binding, the long and variable length of peptides presented by MHCII, and the complexity of the interactions between these longer peptides and the peptide-binding groove of MHCII. Given

these complicating factors, peptide-MHCII binding is most often evaluated experimentally using competitive binding assays. While these binding assays provide detailed quantitative information for peptide-MHCII binding, this detail comes at the expense of throughput, as 8 to 12 point titrations (often in triplicate) are generally required to evaluate just a single peptide-MHCII combination. Here, we aimed to develop a high-throughput peptide-MHCII screening strategy to strike a balance between the throughput offered by computational peptide-MHC binding predictors and the quantitative detail and reliability offered by competitive peptide-MHCII binding assays. Using this approach – which we have termed microsphere assisted peptide screening (MAPS) – we screened antigenic peptide libraries derived from the rotavirus outer capsid glycoprotein VP7 and the Zika virus envelope (E) protein for binding to four common MHCII alleles including DR1, DR4, DR7 and DR15. Interestingly, the results of this MAPS approach revealed a significant overlap between the peptides from the two viral libraries that promiscuously bound all four MHCII alleles and the antibody neutralization sites on each respective protein. This overlap suggests a deeper relationship between B cell and $CD4^+$ T cell specificity, which could be relevant to the design of broadly protective vaccines, as well as the identification of immunodominant peptide targets for T cell immunotherapy.

2.3. Introduction

Identifying antigenic targets recognized by T cells (T cell epitopes) is a critical step in the development of peptide-based vaccines and therapeutics for treating infectious disease,[48,233] cancer,[182,234] and autoimmune conditions.[39] Before a T cell can recognize a specific antigenic peptide, that peptide must first be presented by a major histocompatibility complex (MHC) molecule. Both class I and class II MHC molecules present peptides through interactions

between specific peptide residues (called the peptide binding register, or PBR) and the MHC peptide-binding groove. MHC molecules are highly polymorphic[1] and most of the genetic diversity is manifested in the peptide-binding groove of different MHC alleles. As a result, different MHC alleles generally exhibit different binding specificities.[27] Because the frequency of MHC alleles varies among ethnically diverse populations, immunodominant peptides from viral[235] and tumor[8] proteins capable of promiscuously binding multiple MHC alleles are of considerable interest for broadly protective peptide-based therapuetics.[7]

The peptide-binding groove of class I MHC (MHCI) is composed of a single heavy chain and is closed at both ends, limiting the size (8 – 11 amino acids) and conformation of binding peptides.[4] In contrast, the peptide-binding groove of class II MHC (MHCII) is formed at the junction of a largely conserved alpha chain and a polymorphic beta chain, and is open at both ends. The open-ended nature of the MHCII peptide binding groove allows these molecules to present longer (13 – 25 amino acids) and more variable length peptides than MHCI.[6] Further, in addition to MHCII interactions with the PBR, flanking residues on either side of PBR can also interact with MHCII molecules.[12,13] These peripheral peptide-flanking residue (PFR) interactions can vary significantly between peptides, depending on their length and composition, and affect peptide-MHCII binding. Because of these factors (i.e. allelic diversity, open-ended peptide binding groove, and PFR interactions), predicting if a peptide will bind a single MHCII allele, much less multiple alleles, is a significant challenge.

Over the past twenty years, several *in silico* strategies have been devised to predict peptide-MHC binding, including matrix based methods,[21,22] structure based methods,[24,25,29] and machine learning methods using artificial neural networks.[16,17,20,236] The accuracy of *in silico* peptide-MHC binding predictors are measured by the area under (AUC) the receiver operating

characteristic (ROC) curve. Currently, machine learning methods using artificial neural networks are among the most accurate *in silico* predictors, achieving an AUC of approximately 0.85 – 0.95 for peptide-MHCI binding predictions and an AUC of approximately 0.75 – 0.85 for peptide-MHCII binding predictions.[237] The accuracy of peptide-MHC binding predictors can often be improved by combining the top-performing individual predictors into a consensus method,[18,238] which is the strategy recommended by the Immune Epitope Database and Analysis Resource (IEDB).[50] Although *in silico* peptide-MHCII binding predictors perform well during cross-validation with standardized datasets, they tend to underperform when applied to new datasets or datasets containing peptides of different lengths.[17] In a study of 21 different peptide-MHCII binding predictors, no individual predictor was found to be suitable for the prediction of promiscuously binding peptides.[27] Moreover, these predictors were characterized by high false-positive rates and even the most accurate could only identify 50% of actual T-cell epitopes from four antigenic protein libraries.[27]

Given the limited accuracy and high false-positive rate of *in silico* peptide-MHCII binding predictors, a demand exists for high-throughput systems capable of reliably identifying promiscuously binding peptides. To this end, a wide range of experimental methods have been applied to measure peptide-MHCII binding, including ELISA,[31,239] fluorescence polarization,[32] gel-filtration with radiolabeled peptides,[31,240] fluorescence resonance energy transfer (FRET),[241,242] surface plasmon resonance (SPR),[243] cell-surface display,[36] and bead-based methods.[35] While many of these techniques are well established and yield quantitative peptide-MHCII binding data, the vast majority tend to sacrifice throughput in favor of quantitative detail. For example, competition based assays like ELISA,[31,239] fluorescence polarization,[32] and some bead-based methods[35] involve titrating the target peptide for competitive binding with a labeled

reference peptide. Although the quantitative binding data derived from these competition assays is critical to improving *in silico* peptide-MHCII binding prediction algorithms, they typically involve 8 – 12 point titrations in triplicate for reliable data. As a result, these strategies require a significant amount of MHCII protein for evaluating just a single peptide-MHCII interaction. Given that a many of the peptides within a library are unlikely to bind a specific MHCII allele, up to 36 allocations (12-point titration in triplicate) of MHCII protein may be dedicated to an assay in which no peptide binding occurs. The MHCII protein requirement of competitive binding assays could be greatly reduced, and the study of peptide-MHCII binding made more efficient, if a preliminary screening strategy was used to identify MHCII binding peptides from a large library of non-binders using a binary classification scheme. Once identified, these MHCII binding peptides could be studied in more detail without spending unnecessary time and resources on non-binding peptides.

Here, we developed and validated one such preliminary peptide-MHCII binding assay called microsphere-assisted peptide screening (MAPS). The MAPS strategy was designed to strike a balance between the throughput offered by *in silico* peptide-MHCII binding predictors and the detail provided by competition-based peptide-MHC binding assays. While the MAPS strategy was found to be sensitive to the relative position of the PBR within the peptide, it significantly outperformed the recommended IEDB *in silico* peptide-MHCII binding predictors (AUC of 0.851 vs. AUC of 0.632, respectively). Moreover, when MAPS was used to screen overlapping peptide libraries derived from the rotavirus outer capsid glycoprotein VP7 and the Zika virus envelope (E) protein for binding to four common human class II MHC alleles, we identified 12 promiscuously binding peptides that bound all four alleles. Of the 12 promiscuously binding peptides within the VP7 and Zika virus E protein libraries, IEDB *in silico* binding

predictors accurately predicted only six, suggesting that computational peptide-MHCII binding predictors alone remain insufficient for the reliable identification of promiscuous peptide-MHCII interactions. Interestingly, three of the seven promiscuously binding peptides from the VP7 library and two of the five promiscuously binding peptides from the Zika virus E protein library were found to overlap with the immunodominant regions of their respective proteins. Taken together, these results demonstrate that MAPS is a reliable, high-throughput method for rapidly identifying immunologically relevant peptide-MHCII interactions.

2.4. Results and Discussion

2.4.1. MAPS Strategy and Experimental Design

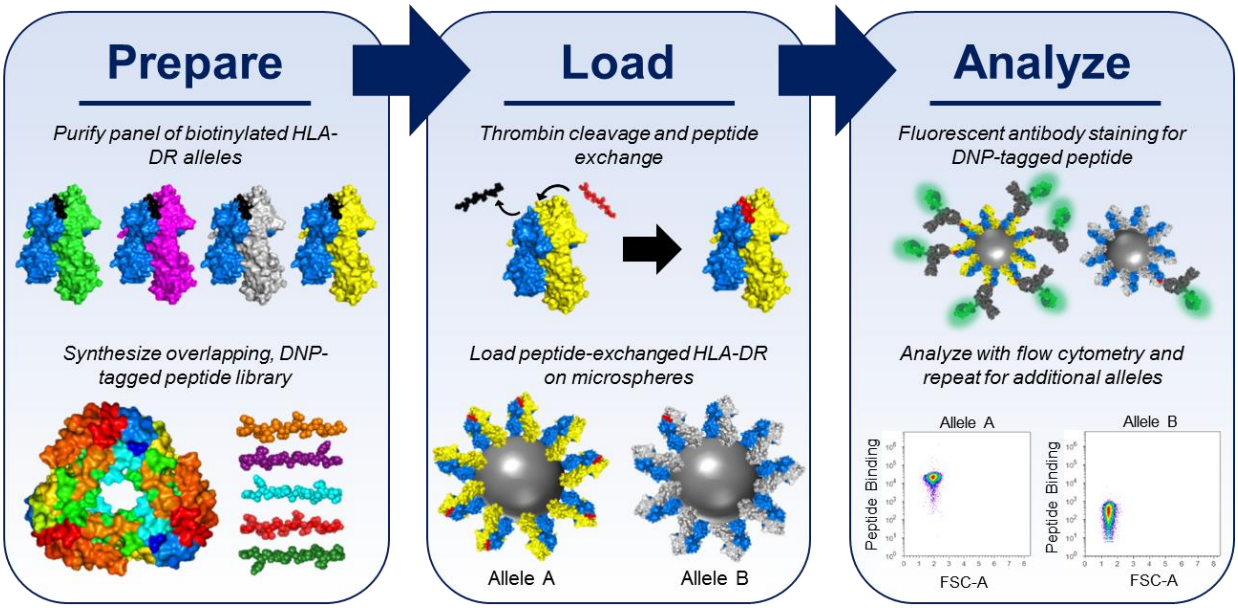

Figure 2.1. MAPS strategy overview.
MAPS involves three steps: prepare, load, and analyze. The preparation step involves purifying and biotinylating a panel of diverse human MHCII alleles and synthesizing an overlapping DNP-tagged peptide library. The loading step involves loading the DNP-tagged peptides from the library onto each MHCII allele via peptide exchange, and loading the biotinylated, peptide-exchanged MHCII on streptavidin-coated microspheres. The analysis step involves staining the loaded microspheres for the DNP-tagged peptide and analyzing resulting signal using flow cytometry.

MAPS is performed in three steps (**Figure 2.1**). First, a diverse panel of human MHCII alleles were designed, expressed, and purified from insect cells. The alpha chain (DRA) of each MHCII was fused to a biotinylation site and each beta chain allele (DRB1*01:01 – DR1, DRB1*04:01 – DR4, DRB7:01:01 – DR7, DRB1*15:01 – DR15) was fused to the invariant chain peptide CLIP, via a thrombin-cleavable linker. The four MHCII alleles chosen – DR1, DR4, DR7, and DR15 – are expected to cover approximately 34% of the U.S. population based on known MHCII allele frequencies[244] and demographic data (**Figure 2.2a**).

a

	Allele Frequency by Ethnicity in U.S.			
Allele	***Caucasian***	***African American***	***Asian***	***Hispanic***
DR1 (DRB1*01:01)	9.1%	2.6%	2.7%	3.9%
DR4 (DRB1*04:01)	9.1%	2.3%	0.9%	1.5%
DR7 (DRB1*07:01)	13.8%	9.8%	8.2%	10.5%
DR15 (DRB1*15:01)	14.4%	2.9%	7.9%	6.7%

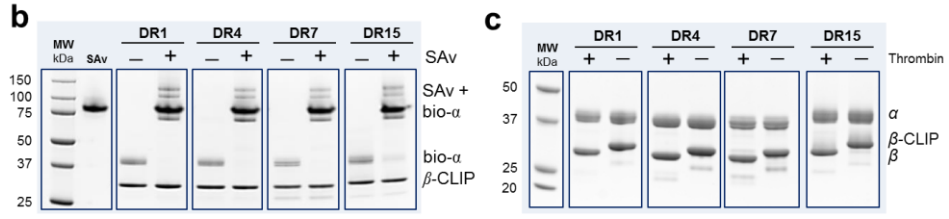

Figure 2.2. Analysis of purified panel of human MHCII alleles.
(a) Frequency of four MHCII beta-chain alleles among different ethnic groups within the U.S. population. (b) SAv gel-shift assay verifying biotinylation of each MHCII allele. Disappearance of bio-α band in the presence of SAv accompanied by a shift in the SAv band indicates biotin-SAv complex formation. (c) SDS-PAGE analysis of thrombin-induced cleavage of the CLIP peptide. A reduction in the size of the size of the β-chain in the presence of thrombin indicates CLIP cleavage.

Each alpha-beta heterodimer was purified from High-Five insect cells and biotinylated. The degree of biotinylation was assessed by incubating the purified MHCII proteins with soluble streptavidin (SAv) and evaluating the complex formation by a streptavidin shift assay using sodium dodecyl sulfate polyacrylamide gel electrophoresis (SDS-PAGE). All alleles were found to be >90% biotinylated (**Figure 2.2b**). In addition to verifying the biotinylation efficiency, the

ability of each MHCII allele to undergo peptide exchange via thrombin-induced cleavage of the CLIP-linker fusion was also verified. To evaluate peptide exchange, each MHCII allele was incubated with thrombin and the CLIP-peptide cleaved constructs were compared to the uncleaved constructs using SDS-PAGE (**Figure 2.2c**). The reduction in the size of the beta chain of each allele confirmed thrombin cleavage.

We next synthesized three peptide libraries to screen for binding to each MHCII allele. Each peptide library consisted of dinitrophenyl- (DNP) tagged 20mers overlapping by 10 amino acids. The first peptide library synthesized was derived from the alkyl hydroperoxide reductase (AhpC) protein of *Burkholderia pseudomallei*. This particular peptide library was chosen because it was recently screened for binding to a diverse panel of MHCII alleles including DR1, DR4, DR7, and DR15.[245] The AhpC peptides therefore served as a reference library for benchmarking the accuracy of the MAPS strategy, as the binding affinity of each peptide MHCII allele combination was known. In addition to the reference library, overlapping peptide libraries derived from the rotavirus outer capsid glycoprotein (VP7) and the Zika virus envelope (E) protein were also synthesized. VP7 and E protein were chosen for screening because each represents a major antigenic target on its respective virus, and immune responses against these proteins generally correlates with positive outcomes during infection.[246–250]

2.4.2. Validating MAPS Strategy with AhpC Reference Library

The MAPS strategy was first validated by screening the AhpC reference library of 16 peptides with known binding affinities for each DR allele (DR1, DR4, DR7, and DR15). Peptide exchange was performed for each peptide-MHCII allele combination, and the exchanged pMHC were loaded onto SAv-coated microspheres (**Figure 2.1)**. The microspheres presenting the

peptide-exchanged MHCII were then stained for the DNP-tagged peptide and analyzed using flow cytometry. Peptide-MHCII binding was quantified as the MAPS signal, which was defined as the ratio of the median fluorescence intensity (MFI) of the DNP-tagged peptide bound to each allele and the MFI of the DNP-tagged peptide incubated with SAv-microspheres alone. Peptide-MHC interactions with a MAPS signal greater than or equal to five were classified as binding peptides.

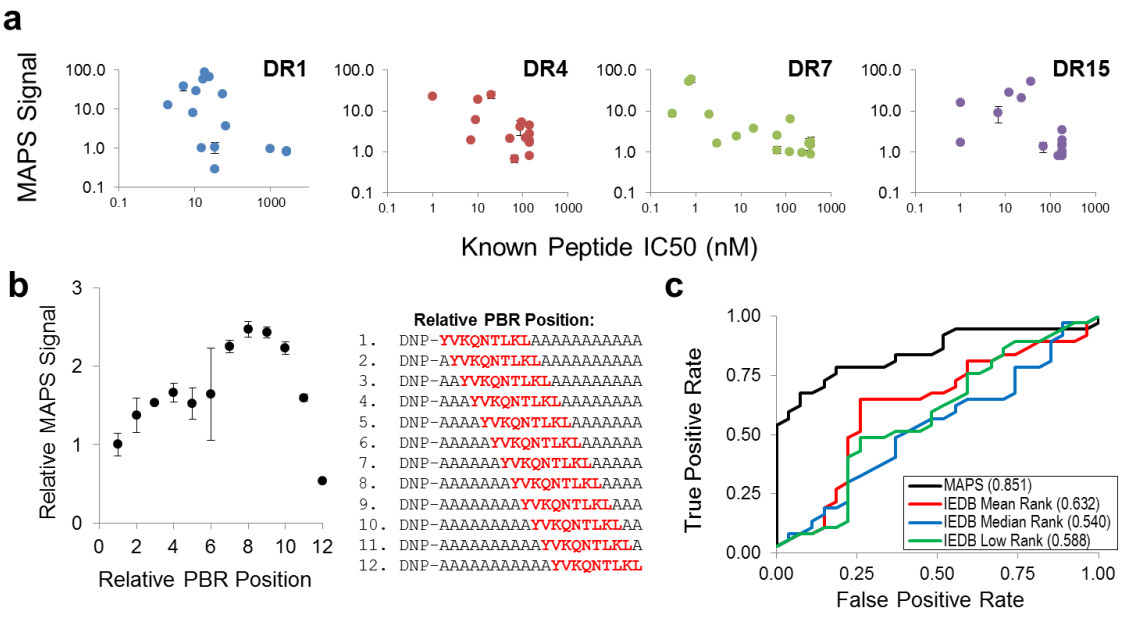

Figure 2.3. Validation of MAPS strategy with AhpC reference peptides.
(a) MAPS signal for each peptide in the AhpC reference library plotted with respect to known peptide IC50. (b) Relative MAPS signal plotted with respect to the relative position of the $HA_{306-318}$ PBR within a 20mer peptide. PFR residues were mutated to alanine. Relative MAPS signal represents the MAPS signal of each peptide normalized by the MAPS signal observed for the peptide with a relative PBR position of one (c) ROC analysis of MAPS strategy compared to the IEDB consensus peptide-MHCII binding predictor for the AhpC reference peptide library. The AUC of each curve is provided in the legend.

The accuracy of the MAPS strategy was then evaluated by plotting the MAPS signal of each peptide-MHCII combination with respect to the peptide's known IC50 value, as determined from a previous study[245] (**Figure 2.3a**). The inverse relationship observed between the MAPS

signal and known IC50 value indicates that the MAPS signal largely correlates with peptide-MHC binding affinity. While the MAPS strategy is generally accurate, we observed that MAPS missed some known binding peptides within the reference library (i.e. peptides known to bind a particular MHCII allele, but exhibited a MAPS signal less than five). To explain these missed binders, we hypothesized that the relative position of the 9mer PBR within the 20mer peptide might affect the accessibility of the DNP tag during antibody staining. For example, if the PBR is located at the N-terminus of a given peptide, the beta-sheet and alpha helices of the peptide-binding groove might obstruct antibody binding to the DNP tag, resulting in a lower MAPS signal. To test this hypothesis, we synthesized 12 DNP-tagged 20mers in which the relative position of the PBR from a well-characterized influenza peptide ($HA_{306-318}$) was shifted from the N-terminus (relative PBR position of 1) to the C-terminus (relative PBR position of 12). The remaining residues were mutated to alanine to avoid introducing complex PFR interactions.

Each peptide was then loaded onto DR1 and MAPS was performed. The MAPS signal for each PBR-variant peptide was normalized such that the MAPS signal observed when the PBR was at the N-terminus (relative PBR position of 1) was equal to one. As expected, the relative MAPS signal was dependent on the position of the PBR within the peptide (**Figure 2.3b**). The relative MAPS signal was highest when the PBR was positioned near the middle of the 20mer peptide (between residues seven and ten), which resulted in up to 2.5 times greater signal than when the PBR was located at the N-terminus. Interestingly, the relative MAPS signal decreased approximately 5-fold from its maximum when the PBR was positioned at the C-terminus of the peptide, suggesting that the accessibility of the DNP tag might also be obstructed when the N-terminus of the peptide is significantly overhanging, or that peptides with a C-terminal PBRs do not MHC as well.

While the MAPS signal is somewhat sensitive to the relative position of the PBR within a given peptide, the actual number of missed binding peptides with unique PBRs should be minimal when screening overlapping peptides because most unique PBRs will appear twice. In addition, although the sensitivity of MAPS to the relative PBR position tends to reduce the overall accuracy of this strategy, this sensitivity could have unanticipated advantages. For example, MAPS used in conjunction with more rigorous protein-protein binding assays could help identify unique PBRs within binding peptides, which is a significant obstacle to improving the accuracy of computational peptide-MHCII binding predictions.[236]

The AhpC reference library was also screened for predicted binding to each MHCII allele using the *in silico* bioinformatics tools provided by IEDB.[50] Peptide-MHCII binding was predicted using the IEDB recommended consensus method,[238] which combined the predictions provided by the artificial neural network-based method NN-align,[20] the stabilized matrix method SMM-align,[22] and the combinatorial library method CombLib.[251] The binding score of the consensus prediction was given as a percentile rank, which scores each peptide's predicted binding affinity against the binding affinities of five million random 15mers from the SWISSPROT database. Therefore, peptides given a low percentile rank were predicted to be strong binders while peptides given a high percentile rank were not predicted to interact strongly with that particular MHCII allele. We defined a predicted binder as a peptide with a percentile rank of less than or equal to 20, in line with previous studies of promiscuously binding peptides.[252] Because the methods provided by the IEDB database are designed to predict MHCII binding of 15mer peptides, each 20mer peptide in the reference library had to be broken down into six different 15mers. The low, median, and mean percentile rank of each of these 15mers was then recorded to evaluate the binding prediction. The accuracy of the IEDB binding

predictions were compared to the experimental results using MAPS by plotting the respective ROC curve of each (**Figure 2.3c** above). Based on this analysis, the AUC for the MAPS ROC curve was found to be approximately 0.851, while the AUCs for the IEDB ROCs were significantly lower, ranging from 0.540 for the median percentile rank to the 0.632 for the mean percentile rank. These results indicate that while the MAPS strategy is susceptible to false-negatives depending on the relative position of the PBR within a peptide, it significantly outperforms the predictions provided by IEDB for 20mer peptide-MHCII binding.

2.4.3. MAPS of Rotavirus VP7 Protein

Figure 2.4. Overlapping rotavirus VP7 library of DNP-tagged 20mers used for MAPS.

After validating the MAPS strategy with the AhpC reference library, we synthesized a 25-peptide library of overlapping 20mers derived from the rotavirus outer capsid glycoprotein VP7 (**Figure 2.4**). Rotavirus is the most common cause of diarrheal disease in children worldwide[253] and remains a significant health challenge in developing countries despite the

approval of two rotavirus vaccines.[254,255] Moreover, genetic analyses of circulating rotavirus strains have revealed differences between the dominant antigenic epitopes on VP7 in circulating rotavirus strains and the vaccine strains, potentially allowing vaccine-resistant mutants to emerge.[246,256] Given the antigenic drift observed in circulating rotavirus strains and the persistence of rotavirus infection across ethnically diverse regions (e.g. sub-Saharan Africa, Southeast Asia, etc.), we aimed to identify promiscuously binding peptides within the VP7 protein, as such peptides might have relevance in peptide-based therapeutics and/or diagnostics.

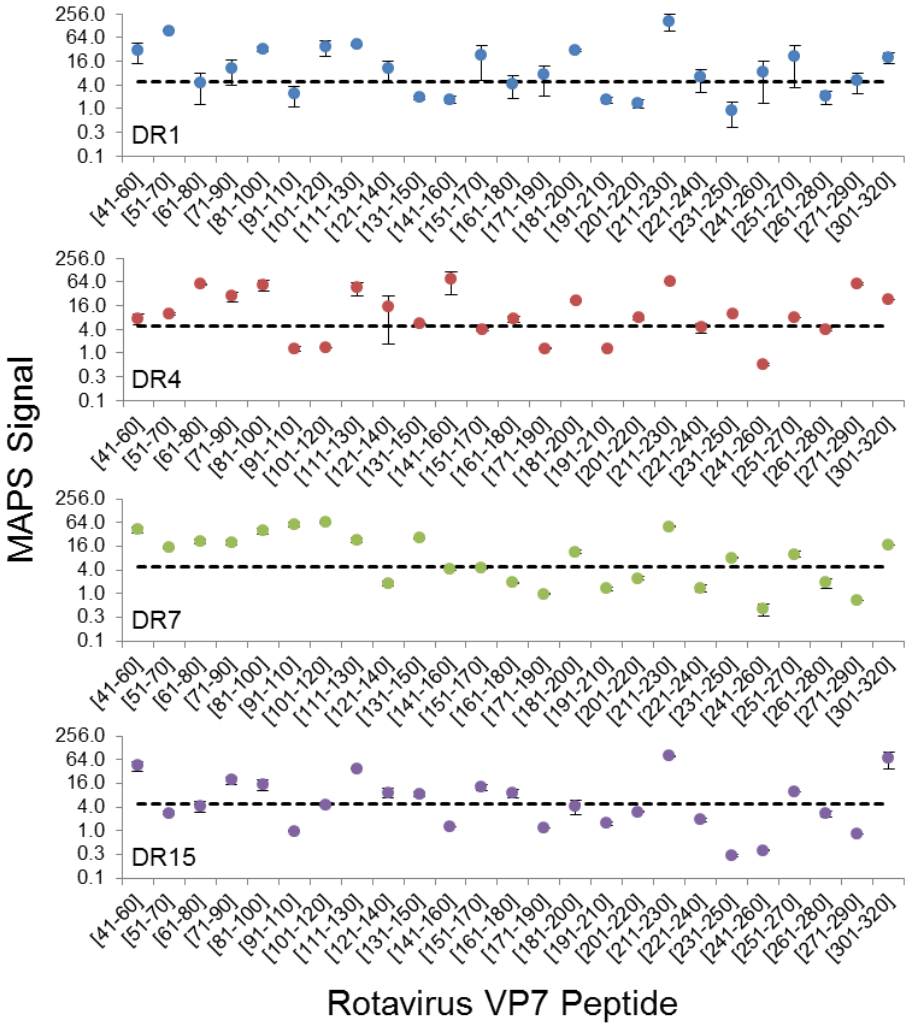

Figure 2.5. MAPS signal of each rotavirus VP7 peptide for each human MHCII allele.

Each 20mer in VP7 peptide library was loaded onto the four MHCII alleles, and peptide-MHCII binding was determined by MAPS (**Figure 2.5**). Promiscuously binding peptides were defined as peptides that exhibited a normalized MAPS signal greater than five for all four MHCII alleles. Based on this criterion, seven promiscuously binding peptides within the VP7 protein were identified: $VP7_{41\text{-}60}$, $VP7_{71\text{-}90}$, $VP7_{81\text{-}100}$, $VP7_{111\text{-}130}$, $VP7_{211\text{-}230}$, $VP7_{251\text{-}270}$, and $VP7_{301\text{-}320}$ (**Figure 2.6a**). Of these seven promiscuously binding peptides, only three were predicted to bind all four alleles by the mean and median of the IEDB percentile rank prediction, while four were predicted to bind all four alleles by the lowest IEDB percentile rank prediction (**Table 2.1**). Further, of the four human MHCII alleles screened, only DR4 was predicted to bind all seven promiscuously binding peptides using the IEDB consensus method. These results are consistent with the performance of the IEDB peptide-MHCII binding prediction for the AhpC reference library, and suggest that *in silico* strategies alone remain insufficient to reliably predict peptide-MHCII binding.

Table 2.1. IEDB consensus method percentile rank of peptide-MHCII binding for promiscuously binding VP7 20mers.
Peptides were defined as binders if the percentile rank below was less than or equal to 20, in line with previous studies investigating promiscuous MHCII-binding peptides.

	Mean IEDB Rank				Median IEDB Rank				Low IEDB Rank			
VP7 Peptide	**DR1**	**DR4**	**DR7**	**DR15**	**DR1**	**DR4**	**DR7**	**DR15**	**DR1**	**DR4**	**DR7**	**DR15**
41-60	15.9	9.1	4.0	11.2	13.0	7.0	1.7	10.2	9.6	6.2	0.9	8.7
71-90	36.9	14.5	21.7	15.9	38.2	13.1	24.0	18.3	28.5	11.0	14.0	4.2
81-100	54.2	28.1	51.6	68.5	48.0	10.3	47.1	81.6	32.3	2.4	31.4	4.8
111-130	12.6	2.2	9.0	6.3	12.8	2.0	10.1	5.6	9.5	1.6	2.8	5.6
211-230	50.1	19.4	57.6	38.9	47.7	17.3	56.4	36.5	47.7	15.5	51.1	32.9
251-270	45.1	28.4	17.6	29.7	48.8	31.9	18.9	26.3	19.0	9.2	1.7	5.5
301-320	10.0	4.0	6.5	2.8	10.0	4.0	4.6	2.4	5.6	3.3	3.9	1.3

To explore the potential immunogenicity of the promiscuously binding VP7 peptides, the position of each peptide within the VP7 protein was analyzed. VP7 contains three dominant antigenic epitopes: 7-1a (BCE 1), 7-1b (BCE 2), and 7-2 (BCE 3),[247] all of which are located near the interface of separate VP7 trimer units. Interestingly, three of the seven promiscuously binding VP7 peptides ($VP7_{81\text{-}100}$, $VP7_{111\text{-}130}$, $VP7_{211\text{-}230}$) identified by MAPS significantly overlapped with these dominant antigenic epitopes (**Figure 2.6b**). The most striking overlap was observed for $VP7_{81\text{-}100}$, which included 8 of the 14 residues of BCE 1. Further, $VP7_{81\text{-}100}$ and $VP7_{111\text{-}130}$ together cover nearly all of BCE 1, overlapping with 12 of the 14 residues (**Figure 2.6c**). $VP7_{211\text{-}230}$ – the VP7 peptide associated with the greatest MAPS signal – also overlapped with dominant antigenic epitopes, albeit to a lesser extent, sharing 3 of the 6 residues of BCE 2 and 2 of the 9 residues of BCE 3 (**Figure 2.6c**).

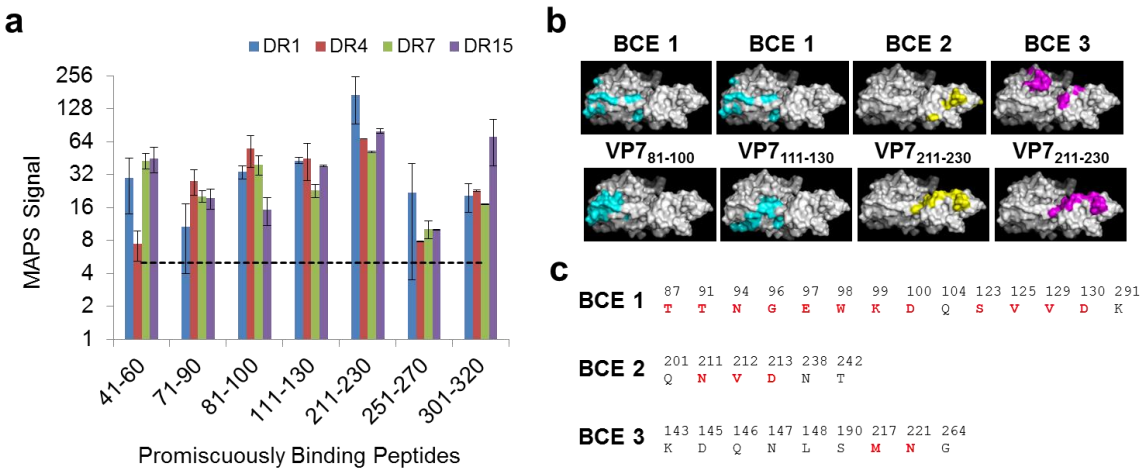

Figure 2.6. Structural analysis of MAPS-identified promiscuously binding VP7 peptides. (a) MAPS signal for each promiscuously binding VP7 peptide. (b) Comparison of the sequence overlaps between three dominant B cell epitopes (BCE) on the VP7 protein (top row) and the promiscuously binding peptides $VP7_{81\text{-}100}$, $VP7_{111\text{-}130}$, and $VP7_{211\text{-}230}$. (c) Amino acid sequence and position of each BCE within the VP7 protein. Overlapping residues with promiscuously binding VP7 peptides are indicated in red.

The significant overlap between the MAPS-identified promiscuously DR-binding VP7 peptides and the dominant antibody neutralization sites on the VP7 protein was unexpected and its immunological relevance is not immediately clear. It is possible that these particular promiscuously binding peptides simply contain "sticky" residues within their primary structure that promote non-specific protein-protein interactions. If a peptide exhibits promiscuous binding to different MHCII alleles, then it seems reasonable to think that the given peptide might also interact promiscuously with other proteins, including immunoglobulins. Alternatively, B cells are professional antigen presenting cells, and internalize extracellular material, including viral particles, using surface displayed B cell receptors (BCRs). Therefore, it is possible that protein fragments that are bound by BCRs are more likely to be presented on B-cell surface displayed MHCII than protein fragments that are not bound by BCRs. However, B cell antigen internalization and presentation alone does not explain why the peptides capable of binding *multiple* MHCII alleles would be overrepresented in terms of sharing residues with antibody neutralization sites. Finally, we cannot preclude the possibility that this overlap between the promiscuously binding VP7 peptides and dominant antibody neutralization sites is merely a coincidence observed for this particular protein. To determine if this observation is simply a coincidence or some phenomenon unique to rotavirus VP7, we synthesized an overlapping peptide library for the Zika virus E protein and performed a similar structural analysis.

2.4.4. MAPS of Zika Virus Envelope Protein

Zika virus is a type of flavivirus, which is a family of structurally similar enveloped viruses transmitted by ticks and mosquitoes. Flaviviruses are commonly associated with tropical climates and include West Nile virus (WNV), dengue virus (DENV), tick-borne encephalitis, and

yellow fever (YFV), among others. The primary antigenic target on flaviviruses – including Zika virus – is the envelope (E) protein, which binds to host cell receptors and mediates virus entry.[248] The Zika virus E protein has three domains, EDI (residues 1-52, 132-193, and 280-296), EDII (residues 52-132 and 193-280), and EDIII (residues 296-406)[257] and is highly similar to the E protein of other flaviviruses, ranging from 39.5% similarity for tick-borne encephalitis to 57.8% similarity for dengue virus 1 (DENV1).[258]

Because Zika virus E protein is similar to the E protein of other flaviviruses, antibodies that bind E protein are often cross-reactive. However, rather than neutralizing a heterologous flavivirus infection, these cross-reactive antibodies tend to exacerbate the infection by promoting the internalization and replication of virus in Fc-receptor expressing cells.[259] This phenomenon, known as antibody-dependent enhancement (ADE), can be life threatening and underscores the importance of eliciting a highly specific, neutralizing antibody response against E protein in areas where multiple flaviviruses circulate. A number of recent studies have shown that antibodies targeting the EDIII domain of the Zika virus E protein tend to be potently neutralizing[249,250,257] and less cross-reactive with E protein from other flaviviruses than antibodies targeting EDI or EDII.[257] Therefore, the EDIII domain of Zika virus E protein is of special interest for a potential Zika virus vaccine.

Although a robust and neutralizing antibody response generally correlates with flavivirus immunity, less is known about the contribution of T cells to clearing flavivirus infection. However, it is thought that T cells play an important role in clearing flavivirus infections from the central nervous system (CNS).[260,261] In a recent study, it was shown that no antibodies are present in the CNS during persistent Zika virus infection in nonhuman primates, and decreased Zika viral load in the CNS correlated with the initiation of a $CD8^+$ T cell response.[262] This

observation is especially interesting considering that while most individuals infected with Zika virus are asymptomatic, serious neurological complications including microcephaly[263] and Guillain-Barre syndrome[264] have been observed at rates up to 1 in 100 and 1 in 5,000 infections, respectively.[265] Because a robust T cell response to Zika virus could play a role in mitigating these neurological complications, the identification of both $CD4^+$ and $CD8^+$ T cell epitopes within Zika virus proteins is an active area of research.[266] Early findings have suggested that, in contrast to other flaviviruses in which T cell epitopes are primarily located on nonstructural proteins (NS), T cell epitopes in Zika virus appear to be located on structural proteins including E protein.[257,260] Given the potential importance of E-protein specific T cell responses for mitigating neurological complications in Zika virus infection, we aim to apply MAPS to identify promiscuously binding peptides within the E protein. In addition, we will also explore any overlap between MAPS-identified promiscuously binding peptides and antibody neutralization sites on the Zika virus E protein, as these shared residues could highlight immunodominant targets for peptide-based therapeutics and/or vaccine development.

To identify promiscuously binding peptides within the Zika virus E protein, we synthesized an overlapping DNP-tagged peptide library of E protein 20mers (**Figure 2.7**). As with the rotavirus VP7 peptide library, each E protein 20mer (ZikVE) was loaded onto the four MHCII alleles and peptide-MHCII binding was determined by MAPS (**Figure 2.8**). Based on the criterion that promiscuously binding peptides exhibit a MAPS signal greater than or equal to five for all four MHCII alleles, five promiscuously binding peptides within the E protein library were identified: $ZikVE_{51\text{-}70}$, $ZikVE_{131\text{-}150}$, $ZikVE_{191\text{-}210}$, $ZikVE_{311\text{-}330}$, $ZikVE_{351\text{-}370}$ (**Figure 2.9a**). Of the five promiscuously binding ZikVE peptides identified by MAPS, only two were predicted to bind all four alleles by the lowest IEDB percentile rank prediction (**Table 2.2**). Interestingly,

only DR4 was predicted to bind all five promiscuously binding peptides, which is consistent with the IEDB prediction for the promiscuously binding VP7 peptides. Together these results provide further evidence that while the IEDB consensus method for predicting promiscuous 20mer peptide-MHCII binding is generally inaccurate, it most accurate for DR4.

Figure 2.7. Overlapping Zika virus E protein library of DNP-tagged 20mers used for MAPS.

Table 2.2. IEDB consensus method percentile rank of peptide-MHCII binding for promiscuously binding ZikVE 20mers.
Peptides were defined as binders if the percentile rank below was less than or equal to 20, in line with previous studies investigating promiscuous MHCII-binding peptides.

	Mean IEDB Rank				Median IEDB Rank				Low IEDB Rank			
ZikVE	**DR1**	**DR4**	**DR7**	**DR15**	**DR1**	**DR4**	**DR7**	**DR15**	**DR1**	**DR4**	**DR7**	**DR15**
51-70	46.4	7.1	30.1	20.4	40.6	4.6	29.8	22.7	30.1	3.0	22.7	4.0
131-150	3.4	0.7	19.9	1.7	2.5	0.5	20.6	1.7	2.3	0.4	11.1	1.7
191-210	46.6	15.8	39.9	18.4	44.9	17.5	42.6	17.9	33.3	0.9	6.8	12.2
311-330	15.0	14.4	20.1	35.6	6.5	9.3	13.5	34.6	1.6	4.0	5.9	24.7
351-370	12.0	6.3	11.1	9.9	9.4	5.0	11.9	10.9	7.7	3.7	9.3	4.7

In contrast to other flaviviruses and rotavirus, a Zika virus vaccine does not currently exist. Therefore, dominant antibody neutralization sites on a vaccine strain cannot be used as point of comparison for the structural analysis of the promiscuously binding peptides within the Zika virus E protein. However, it is well documented that antibodies binding the EDIII domain tend to be potently neutralizing and less prone to ADE than antibodies binding the EDI and EDII domains.[257] Analyzing the position of each promiscuously binding ZikVE peptide within the structure of the E protein dimer revealed that one promiscuously binding peptide is within the EDI domain ($ZikVE_{131-150}$), while two are within the EDII ($ZikVE_{51-70}$ and $ZikVE_{191-210}$) and EDIII domains ($ZikVE_{311-330}$ and $ZikVE_{351-370}$) (**Figure 2.9b**).

While less data is available regarding specific antibody neutralization sites on the Zika virus E protein, a 2017 study reported that a neutralizing antibody in Zika-infected individuals contacted residues A311, T351, and L352, among others.[249] These residues can also be found within the EDIII promiscuously binding peptides $ZikVE_{311-330}$ and $ZikVE_{351-370}$. Moreover, the same study also reported that mutating the lysine at residue 394 to alanine eliminated antibody binding, suggesting that antibody recognition of K394 is critical for neutralization. While the relevant peptide $ZikVE_{391-410}$ did not fulfil our criterion as a promiscuously binding peptide, it exhibited a MAPS signal greater than five for three of the four alleles tested (DR1, DR4, and DR7). If we include this quasi-promiscuously binding $ZikVE_{391-410}$ in our analysis, 8 of the 18 antibody neutralization sites on the E protein were also present in promiscuously binding ZikVE peptides. Similarly, another study reported that antibodies contacting residues M68, S70, V153, T315, and P354 (among others) were potently cross neutralizing to Dengue and Zika virus. In addition to the T315 and P354 residues found in the promiscuously binding EDIII peptides $ZikVE_{311-330}$ and $ZikVE_{351-370}$, M68 and S70 are found in the promiscuously binding EDII

peptide ZikVE$_{51-70}$. In total, 6 of the 16 E protein antibody neutralization sites described in this study are also present in the MAPS-identified promiscuously binding ZikVE peptides. Therefore, as with the promiscuously binding VP7 peptides, we observed considerable overlap between the MAPS-identified promiscuously binding ZikVE peptides and antibody neutralization sites on the Zika virus E protein.

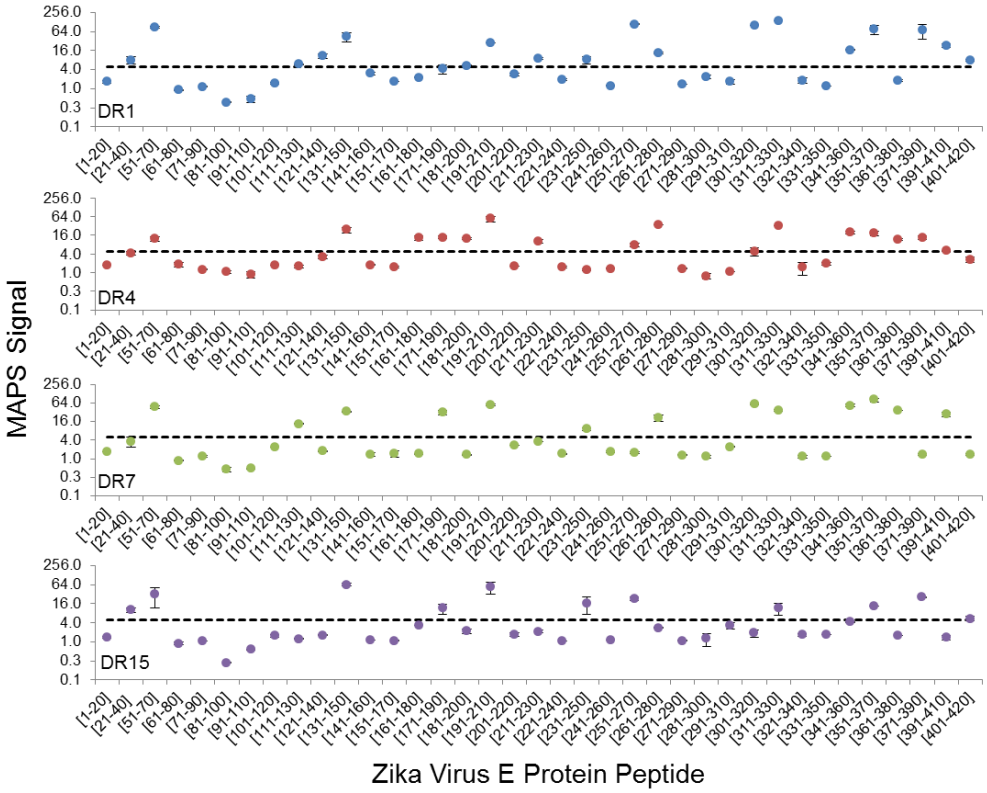

Figure 2.8. MAPS signal of each Zika virus E protein peptide for each human MHCII allele.

While the data gathered thus far are insufficient to definitively preclude coincidence, the significant overlap between MAPS-identified promiscuously binding peptides and antibody neutralization sites for both the rotavirus VP7 protein and Zika virus E protein suggests a deeper relationship between BCR binding and antigen presentation to CD4$^+$ T cells. This phenomenon

of paired antigen specificity between B cells and T cell has been observed before,[267,268] and might be caused by the fact that B cell receptor (BCR) bound residues are protected from degradation during B-cell antigen processing.[269]

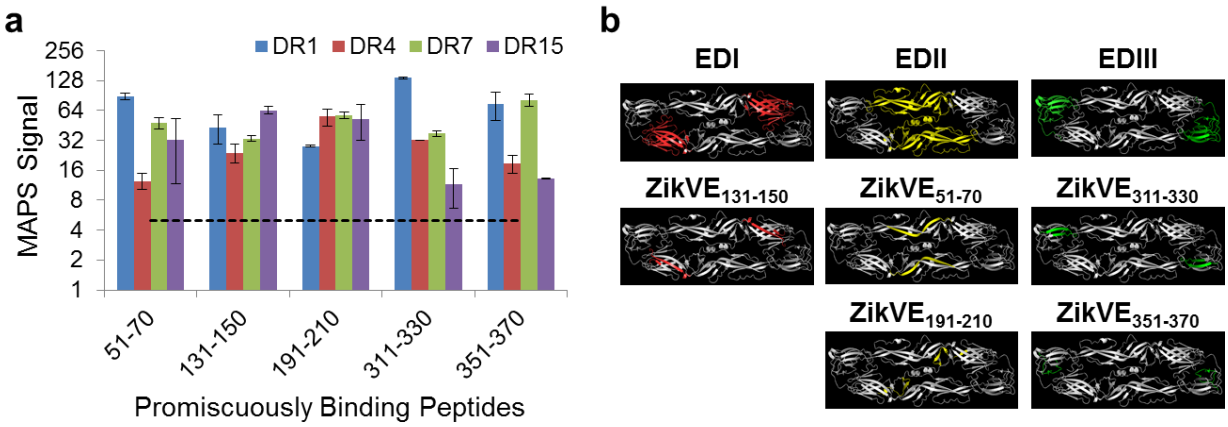

Figure 2.9. Structural analysis of MAPS-identified promiscuously binding peptides in the Zika virus E protein dimer.
(a) MAPS signal for each promiscuously binding E protein peptide. (b) Structural analysis of promiscuously binding peptides within the E protein dimer. The E protein domains are color coded in the top row (EDI – red, EDII – yellow, and EDIII – green) and the location of each MAPS-identified promiscuously binding peptide is shown in the bottom row.

A similar phenomenon was observed in a recent study that found $CD4^+$ T cells preferentially target the same structural proteins (*e.g.* E protein) as B cells during Dengue infection.[270] Moreover, as in the present study, researchers observed significant overlap between regions of the Dengue E protein recognized by $CD4^+$ T cells and those targeted by IgG molecules. Together, these results suggest that virus-specific B cells bind, internalize, and present structural proteins on MHCII during virus infection, which preferentially expand $CD4^+$ T cells of the same or similar specificity.[270] An interesting outcome of shared B/T cell specificity is the possibility of predicting $CD4^+$ T cell epitopes from known antibody neutralization sites and vice versa.[271] Regardless, the observed overlap between antibody neutralization sites and $CD4^+$ T cell epitopes

highlights the importance of MHCII restriction – and the corresponding utility of peptide-MHCII screening strategies like MAPS – in the design and development of vaccines.[271]

Although we have not yet (work in progress) independently confirmed that the promiscuously binding ZikVE peptides are actual $CD4^+$ T cell epitopes, a 2018 study[266] found that $ZikVE_{51-70}$, $ZikVE_{131-150}$, and $ZikVE_{191-210}$ existed as $CD4^+$ T cell epitopes in HLA-DR4 transgenic mice primed with 25 μg of recombinant Zika envelope protein. Similarly, $ZikVE_{131-150}$ and $ZikVE_{311-330}$ were also shown to be $CD4^+$ T cell epitopes in HLA-DR1 and HLA-DR15 transgenic mice, respectively.[266] Further, when mice were challenged with Zika virus infection, $CD4^+$ T cell response to $ZikVE_{351-370}$ was among the strongest as measured by IFNγ ELISpot. These results indicate that each of the promiscuously binding E protein peptides identified using MAPS have been shown to be true T cell epitopes in either humans or animal models. Moreover, while the aforementioned study included DR1, DR4, and DR15, we can confirm that these peptides ($ZikVE_{51-70}$, $ZikVE_{131-150}$, $ZikVE_{191-210}$, $ZikVE_{311-330}$, and $ZikVE_{351-370}$) also bind DR7, which provides broader coverage to Hispanic and African American populations (10.5% and 9.8%, respectively).

2.5. Conclusions and Outlook

Viral infections and their vaccination are often studied in the context of a neutralizing antibody response; however, $CD4^+$ T cells also play an important role in viral immunity.[272] Therefore, identifying T cell epitopes is an important part of understanding how viral antigens are processed and presented, as well as predicting what viral protein fragments are likely to be recognized by T cells. A thorough understanding of T cell epitopes derived from viral proteins

should help in the development of both diagnostic tools and peptide-based vaccines and therapeutics.[9,273,274]

However, before a T cell epitope can be identified the cognate peptide must be loaded onto an MHC molecule. Because peptide-MHC binding is a prerequisite for T cell epitope discovery, it is necessary to first evaluate whether a particular peptide is capable of binding a particular MHC allele. While computational tools have come a long way in the past two decades – especially for peptide-MHCI binding prediction – reliably predicting peptide-MHCII binding remains a challenge.[238] This is largely because the open-ended peptide-binding groove of MHCII molecules allows for the presentation of longer peptides than MHCI. Longer peptides coupled with open-ended binding grooves allow for a greater number of possible peptide conformations within MHCII, the optimum of which is difficult to predict. This difficulty is further complicated by secondary interactions between flanking residues at the peripheries of the peptide PBR and the MHCII molecule. In addition, MHCII are characterized by substantial allelic diversity, which is manifested in different peptide-contacting residues within the peptide-binding grooves of different MHCII alleles. This MHCII polymorphism results in MHCII molecules exhibiting a wide range of peptide-binding specificities, depending on the particular MHCII allele. Therefore, MHCII allelic diversity must be carefully considered in the development of therapeutic products if they are to be applicable to an ethnically diverse population.

Here we report the development and validation of MAPS – a high-throughput screening strategy for rapidly identifying promiscuously MHCII-binding peptides. Using this approach, we identified seven and five 20mer peptides derived from the rotavirus VP7 protein and the Zika virus E protein, respectively, capable of strongly binding four common class II MHC alleles. Moreover, a structural analysis of these promiscuously binding peptides within their respective

proteins revealed substantial overlap with dominant antibody neutralization sites, indicating that these peptides correspond to immunodominant regions of each viral protein, and are thus strong candidates for diagnostic and peptide-based vaccines. In addition, these findings contribute to a body of knowledge[269–271] that suggests a more complex and important relationship between the B cell and $CD4^+$ T cell specificity.

In addition to independently confirming that the MAPS identified promiscuously binding peptides are T cell epitopes by tetramer staining, we also plan to quantify peptide-MHCII binding affinity using conventional assays.[32] This quantitative peptide-MHCII binding data will then be reported so that it can be included in large datasets that are used to train predictive peptide-MHCII binding algorithms. The identification of promiscuously binding peptides is particularly interesting in the context of training predictive peptide-MHCII binding algorithms, as these peptides necessarily exhibit physical characteristics that allow binding to diverse MHCII alleles. Further investigation of the chemical and structural similarities between promiscuously binding peptides should help elucidate molecular signatures that promote their promiscuous binding and improve the accuracy of predictive algorithms.

While quantitative binding data is critical to improving the accuracy of computational peptide-MHCII binding predictors, this data alone provides an incomplete picture of peptide-MHCII binding. Identification of the 9mer PBR core that facilitates the principle interaction between a peptide and an MHCII molecule is also important. In fact, PBR identification is one of the greatest challenges associated with predicting peptide-MHCII binding.[28] Although the MAPS strategy described here was designed to rapidly identify promiscuously binding peptides, the method used to detect peptide binding was found to be sensitive to the relative position of the PBR core within 20mer peptides (**Figure 2.3b**). While this unforeseen sensitivity complicates the

translation of the observed MAPS signal to peptide-MHC binding affinity, it does provide some insight into the location of the PBR. As a result, MAPS coupled with quantitative measurements of peptide-MHCII binding affinity might provide a basis for the informed prediction of the PBR within a 20mer peptide. Moreover, our data suggests that the accuracy of such a prediction will likely improve if the PBR is located near the extreme ends of the peptide, where the MAPS signal is most sensitive (**Figure 2.3b**).

The central theme of this dissertation is the development and validation of molecular tools with applications in T cell immunotherapy. Like any tool, MAPS is designed for a specific task; namely, a simple and high-throughput method for identifying peptides that promiscuously bind to multiple MHCII alleles. In addition to identifying promiscuously binding peptides from antigenic viral protein libraries, MAPS also provided insight into immunodominant regions of these viral proteins that could be targeted by both B cells and $CD4^+$ T cells during viral infections. While we demonstrated the utility of the MAPS strategy in the context of viral immunity, this approach is also applicable to the high-throughput screening cancer neoantigens for cancer immunotherapy.

2.6. Materials and Methods

2.6.1. Protein Design, Expression, and Peptide Synthesis

Human MHCII proteins were assembled by isolating the extracellular domains of the alpha chain HLA-DRA (UniProt: P01903, residues 26-216) and each beta chain allele: HLA-DRB1*01:01 (UniProt: P04229, residues 30-227), HLA-DRB1*04:01 (UniProt:P13760, residues 30-227), HLA-DRB1*07:01 (UniProt: P13761, residues 30-227), HLA-DRB1*15:01 (UniProt: P01911, residues 30-227). The leucine zipper dimerization motifs Fos and Jun were fused to the

C-terminus of the DRA and DRB1 chains, respectively, as described elsewhere.[275] The 15 amino acid AviTag™ (GLNDIFEAQKIEWHE) was fused to the C-terminus of the Fos dimerization motif on the DRA chain to allow for biotinylation and a 6X-Histidine tag was fused to the C-terminus of the complete recombinant DRA chain for purification. The N-terminus of each DRB1 chain was fused to the invariant chain $CLIP_{87\text{-}101}$ peptide via a thrombin-cleavable linker to allow for peptide exchange, as described elsewhere.[276] The C-terminus of the Jun-dimerization motif of each DRB1 was fused to a 6X-Histidine tag for purification. Finally, the N-terminus of each dimeric chain was fused to the baculovirus gp64 signal peptide and ligated into separate baculovirus transfer vectors pAcGP67A (BaculoGold Baculovirus Expression System, Pharmingen BD Biosciences, San Jose, CA). The DNA sequence of each construct was verified by Sanger sequencing.

Spodoptera frugiperda (SF9) insect cells were transfected with transfer vectors carrying the recombinant DRA chain and each recombinant beta chain (DR1, DR4, DR7, and DR15) with linearized Baculovirus DNA (Pharmingen BD BaculoGold Biosciences, San Jose, CA) using Cellfectin II (Invitrogen) according to the manufacturer's protocol. Low-titer P0 viral stocks carrying the recombinant DRA and DRB1 genes were isolated from the transfection supernatant and amplified separately in SF9 cells to create high-titer P1 viral stocks. Each human MHCII heterodimer was expressed by co-infecting High-Five cells at a density of 2.0 M/mL with equal volumes of high-titer P1 DRA and DRB1 baculovirus stocks. MHCII protein was harvested 72 h after infection and purified using affinity chromatography with Ni-NTA beads according to the manufacturer's protocol (Qiagen). SDS-PAGE analysis was performed to evaluate protein purity.

Approximately 0.5 mg of each peptide used in this work was chemically synthesized by Sigma-Aldrich (Woodlands, TX). Each peptide was designed to be 20 amino acids long and was

fused to an N-terminal dinitrophenyl (DNP) tag. Peptide libraries covering the *B. pseudomallei* alkyl hydroperoxide reductase (AhpC) protein (UniProt: Q63T73 residues, 1 – 180), the rotavirus outer capsid glycoprotein VP7 (UniProt: P11853 residues 41 – 320), and the Zika virus E protein (UniProt: A0A024B7W1 residues 291 – 794) were designed such that each 20mer peptide overlapped with the preceding peptide in the sequence by 10 amino acids. DNP-tagged variants of DR1-binding peptide the $HA_{306-318}$ were synthesized were also synthesized to determine how relative PBR position affects MAPS signal. Peptides in the libraries that could not be chemically synthesized were not included in the MAPS analysis, and explain any non-consecutive sequences in **Figure 2.4** and **Figure 2.7**.

2.6.2. Biotinylation and Peptide Exchange

After purifying the human MHC-CLIP proteins, the DRA chain of each heterodimer was biotinylated. Biotinylation reactions were performed with the AviTag™ biotinylation kit (Avidity LLC, Aurora, CO) according to the manufacturer's protocol. Biotinylation reactions were performed at room temperature overnight. The biotinylation efficiency for each allele was assessed using a streptavidin gel-shift assay. Briefly, biotinylated MHC-CLIP proteins were buffer exchanged into HEPES buffered saline (HBS) and incubated with excess streptavidin for 1 h at 30 °C. The complexes were then analyzed using SDS-PAGE, and biotinylation efficiency was evaluated by estimating the fraction of the biotinylated DRA chain that shifted following incubation with streptavidin.

Peptide exchange was performed similar to previously published methods,[46] with some modifications. Prior to peptide exchange, the $CLIP_{87-101}$ peptide fused to each DR beta chain was cleaved. $CLIP_{87-101}$ cleavage was performed by incubating the MHC-CLIP protein with

restriction grade thrombin (Novagen, Madison, WI) for 2 h at 37 °C at a concentration of ten units per milligram of protein. Thrombin-induced $CLIP_{87-101}$ cleavage was confirmed using SDS-PAGE (**Figure 2.2c**). Following $CLIP_{87-101}$ cleavage, peptide exchange was performed by transferring the empty DR alleles into peptide exchange buffer containing 50 mM sodium citrate pH 5.2, 1% octylglucoside, and 100 mM NaCl. DR alleles were then incubated with 25 molar excess DNP-tagged peptides for 16 h at 37 °C. Peptides were diluted in a solution of 50% DMSO in HBS to minimize precipitation prior to loading. After 16 h, the peptide exchange reaction was neutralized by adding 1/5 volume of 1 M Tris pH 8.0.

2.6.3. MAPS and Flow Cytometry

Following peptide exchange, 2 μg of each exchanged MHCII was incubated with 100,000 streptavidin-coated microspheres (Bangs Laboratories, Fishers, IN) in 1% bovine serum albumin (BSA) for 1 h at room temperature. In parallel, an equivalent amount of DNP-tagged peptide used in the peptide exchange reaction was incubated with streptavidin-coated microspheres in the absence of MHCII for calculating the MAPS signal. After loading, the microspheres were washed in 1% BSA and stained with 2 ng/μL of rat anti-DNP antibody (Clone LO-DNP-2, Invitrogen, Waltham, MA) for 30 min at room temperature. Stained microspheres were washed in 1% BSA and stained with 2 ng/μL of secondary goat-anti-rat PE (Invitrogen, Waltham, MA) for 30 min at room temperature. The stained microspheres were then washed twice in 1% BSA and resuspended in 500 μL for analysis by flow cytometry. Flow cytometry was performed by gating on the population of single microspheres and analyzing the median fluorescence intensity (MFI) from the DNP fluorescent staining. The MAPS signal was determined by normalizing the peptide-MHC DNP MFI by the MFI of the peptide incubated with the microspheres alone. This

normalization accounted for non-specific binding of peptides to the streptavidin-coated microspheres. Peptide-MHC interactions exhibiting a MAPS signal greater than or equal to five were defined as binding interactions.

2.6.4. IEDB peptide-MHCII Binding Prediction

IEDB peptide-MHCII binding predictions were performed by entering each 20mer peptide sequence and predicting its binding to DRB1*01:01, DRB1*04:01, DRB1*07:01, and DRB1*15:01 using the IEDB recommended prediction method. The output data was broken down into six 15mers for each 20mer sequence provided. The IEDB consensus method[238,251] was used to predict peptide MHCII binding, which provided a binding percentile rank for each 15mer. The percentile rank binding score was calculated by comparing the predicted peptide-MHCII binding affinity of the target peptide against 5 million random 15mers from the SWISSPROT database. Accordingly, a low percentile rank indicated a high predicted binding affinity while a high percentile rank indicated a low predicted binding affinity. The mean, median, and low percentile rank were calculated from the six 15mers derived from each single 20mer sequence, and analyzed separately. Peptides were said to be binders if the percentile rank was less than or equal to 20, in accordance with a previous study concerned with promiscuously binding peptides.[252]

Chapter 3. Protein-Scaffold Directed Nanoscale Assembly of T Cell Ligands: Artificial Antigen Presentation with Defined Valency, Density, and Ratio

3.1. Publication Information

Smith, M. R., Tolbert, S. V., Wen, F. Protein-Scaffold Directed Nanoscale Assembly of T Cell Ligands: Artificial Antigen Presentation with Defined Valency, Density, and Ratio. *ACS Synth. Biol.* 7(6), 1629 – 1639. 2018.

The goal of this chapter is to demonstrate that T cell activation can be finely tuned by controlling the spatial and stoichiometric organization of T cell ligands on the surface of a yeast cell. To our knowledge, this is the first study demonstrating that the nanoscale organization of T cell ligands on the surface of a living cell can be controlled using supramolecular assembly engineering based on cohesin-dockerin binding. Stephanie Tolbert assisted in expressing and purifying the proteins used in this study.

3.2. Abstract.

Tuning antigen presentation to T cells is a critical step in investigating key aspects of T cell activation. However, existing technologies have a limited ability to control the spatial and stoichiometric organization of T cell ligands on 3D surfaces. Here, we developed an artificial antigen presentation platform based on protein scaffold-directed assembly that allows fine control over the spatial and stoichiometric organization of T cell ligands on a 3D yeast cell

surface. Using this system, we observed that the T cell activation threshold on a 3D surface is independent of peptide-major histocompatibility complex (pMHC) valency but instead is determined by the overall pMHC surface density. When intercellular adhesion molecule 1 (ICAM-1) was coassembled with pMHC, it enhanced antigen recognition sensitivity by 6-fold. Further, T cells responded with different magnitudes to varying ratios of pMHC and ICAM-1 and exhibited a maximum response at a ratio of 15% pMHC and 85% ICAM-1, introducing an additional parameter for tuning T cell activation. This protein scaffold-directed assembly technology is readily transferrable to acellular surfaces for translational research as well as large-scale T-cell manufacturing.

3.3. Introduction

In nature, T cells are activated by binding peptide-major histocompatibility complex (pMHC) and costimulatory molecules displayed on the surface of antigen presenting cells (APCs). These T cell ligands form complex multi-component assemblies with both the micro- and nanoscale organization. The spatial and stoichiometric organization of these assemblies plays an important role in promoting T cell expansion and determining T cell phenotype and function.[117,277] Therefore, identifying the spatial and stoichiometric parameters of T cell ligand assemblies that promote robust T cell activation is critical to reveal molecular insights that can be applied to translational immunotherapy.

A variety of artificial antigen presentation systems have been developed to control the spatial organization of T cell ligands including modified fluid lipid bilayers[194,197,198,278,279] and patterned coverslips.[279–281] Nanolithographic patterning of TCR ligands (e.g. anti-CD3, anti-TCR, and pMHC) on glass coverslips has been used to determine a minimum pMHC surface

density of 90 – 140 pMHC/μm^2 for T cell activation.[186,189] Above this threshold, T cell response can be fine-tuned by controlling the global TCR-ligand surface density.[186–188] The nanoscale organization of TCR-ligands can be quantified as TCR-ligand valency, and has also been shown to affect T cell activation.[81,223,282–284] When two soluble pMHC molecules are crosslinked by a peptide linker, T cell activation is inversely correlated with the linker length (5 nm – 9 nm).[282] Other studies demonstrated that T cell activation can be further enhanced several-fold by increasing the degree of valency of soluble TCR ligands up to 10 for anti-CD3[223] and up to 300 for pMHC.[283] Despite reports that soluble multivalent pMHC complexes enhance T cell activation, it is unclear if T cells respond similarly to surface-bound multivalent pMHC.[285] Given that class II pMHC arrive at the plasma membrane of dendritic cells in sub 100-nm microclusters[286] and TCR on resting T cells are similarly aggregated,[287] there is reason to believe that surface-bound multivalent pMHC may enhance T cell activation through avidity effects.

The overwhelming majority of artificial antigen presentation systems that allow the nanoscale tuning of TCR ligand organization are 2D. While 2D systems are powerful research platforms amenable to elegant imaging and signaling studies, their planar geometry represents a significant departure from 3D cell-cell interactions in nature. For example, planar systems provide sustained interfacial contact between T cells and a relatively unidirectional antigen-presenting surface, while 3D cell-cell interactions do not. In addition, 2D artificial antigen presentation systems may have limited scalability in T cell manufacturing due to their lower antigen-presentation surface area per unit than 3D systems. Most current large-scale *ex vivo* T cell activation is performed in bioreactors using anti-CD3/anti-CD28 coated beads. Recent advances in the design of patchy particles[288,289] have enabled the regular patterning of 3D surfaces; however, the resolution of this approach is currently limited to ~3 μm diameter (1/6th

the diameter of the microsphere)[288] patches. This patterning resolution is too coarse to probe how T cells respond to nanoscale ligand organization.

In addition to controlling the spatial organization of T cell ligands, artificial antigen presentation systems have also been designed to control the composition of different T cell ligands. In contrast to the aforementioned planar systems, the ones designed to control the composition of costimulatory and adhesion molecules during antigen presentation are often cell lines, and thus 3D. Studies have shown that presentation of intercellular adhesion molecule 1 (ICAM-1) by both cells and acellular beads accelerates the production of IL-2 and IFN-γ by $CD4^+$ T cells.[115] Similarly, 4-1BBL presentation on engineered cells has been shown to enhance the expansion of functional $CD8^+$ T cells more effectively than anti-CD28.[123] The presentation of multiple costimulatory molecules such as various combinations of ICAM-1, CD80, CD86, and 4-1BBL further improves T cell proliferation and activation.[126–128] While insights gained from manipulating costimulatory signals have already been translated to improved clinical designs of therapeutic T cells,[172] most studies to date have focused on simply combining costimulatory/adhesion molecules with little control over their valency or ratio. This is technically challenging on cell surfaces. Even with synthetic systems, this control has thus far been limited to biotin-avidin based presentation methods such as anti-CD3/anti-CD28 coated beads[290] and stochastically clustered anti-CD3/anti-CD28/anti-LFA-1 on neutravidin anchored in liposomes.[221] Therefore, the extent to which T cell activation can be tuned by simultaneously modulating the stoichiometric ratio and valency of pMHC and adhesion/costimulatory molecules during antigen presentation remains unclear.

Here, we describe a modular artificial antigen presentation system that provides control over the spatial and stoichiometric organization of immunological proteins on a 3D yeast cell

surface using protein-scaffold directed assembly. These yeast antigen-presenting cells (yAPCs) enabled for the first time the systematic and quantitative investigation of how nanoscale protein organization on a 3D surface influences T cell activation. This work presents a new strategy for tuning antigen presentation on 3D surfaces by controlling the valency, density, and ratio of T cell ligands. The underlying principle of scaffold-directed assembly based on high affinity protein-protein interactions described here can be readily applied to acellular 3D surfaces, such as polystyrene and magnetic microparticles and hydrogels,[291] greatly expanding its potential applications.

3.4. Results and Discussion

3.4.1. Molecular Design for Patterning Cell Surface with Defined pMHC Valency and Density

pMHC spatial organization can be controlled by manipulating both the occupancy of nanoscale pMHC clusters on a surface (i.e. pMHC valency) and the global pMHC density across the entire surface. To control pMHC valency and the global pMHC surface density, yeast cells were engineered to assemble pMHC on surface-displayed multivalent protein scaffolds (**Figure 3.1**). Yeast cells were chosen as a model antigen presenting system for their inability to activate T cells *in vitro*[41,205,292] and the versatile genetic tools available that allow proteins to be displayed on the yeast cell surface.[292–297] Modular cohesin units from the CipA protein[298] of *Clostridium thermocellum* were recombined to create custom protein scaffolds containing a tunable number of binding sites ranging from one (yAPC1) to five (yAPC5) (Coh1 – Coh5 in **Figure 3.1**). Cohesin units bind strongly to cognate protein units called dockerins. To organize pMHC on the yeast-displayed cohesin scaffolds, a cognate dockerin domain[299] from *C. thermocellum* was fused to the alpha-chain of the class II MHC HLA-DR1 (**Figure 3.2**). The pMHC-dockerin

fusion allows the protein scaffolds to direct the supramolecular assembly of pMHC on a 3D surface (**Figure 3.2b**). pMHC valency is controlled through the number of cohesin units in the protein scaffold. For example, yAPC5 represents a yeast cell displaying protein scaffolds with five cohesin units, and therefore presents five pMHC molecules per protein scaffold (**Figure 3.1**, bottom right). These multivalent protein scaffolds included an N-terminal Aga2 fusion which forms a disulfide linkage to Aga1 on the yeast cell surface[294] (**Figure 3.2a**) allowing the pMHC surface density to be tuned by treating yeast cells with a reducing agent. The protein scaffolds also included a C-terminal V5 epitope tag for detection and molecular quantification.

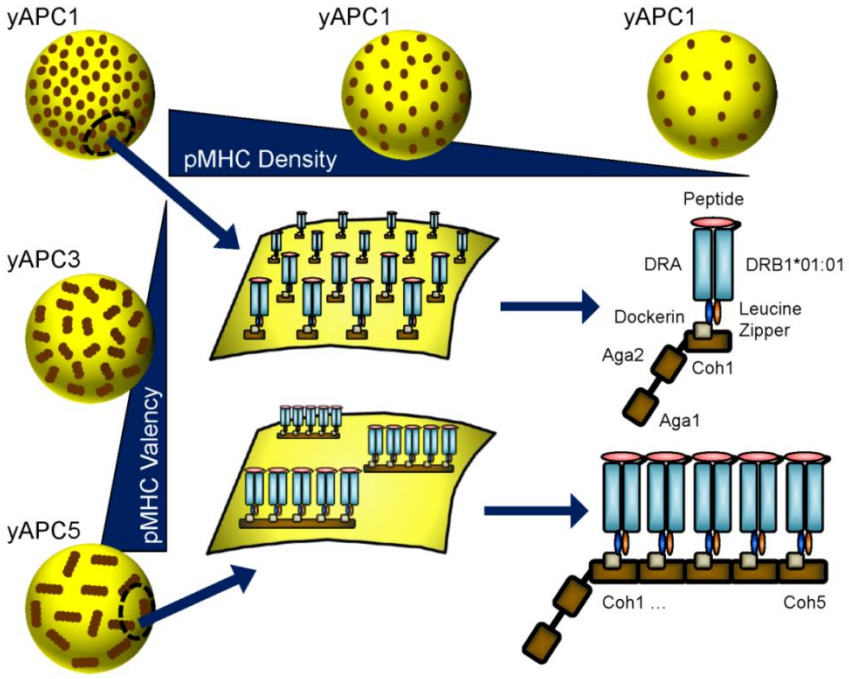

Figure 3.1. Schematic depicting yAPC system assembly and tunability.
yAPC was engineered to accommodate pMHC with valency between 1 (yAPC1) and 5 (yAPC5). Scaffold spacing and corresponding global pMHC surface density can be tuned to generate yAPCs with a broad range of pMHC surface densities. pMHC was expressed as a heterodimer stabilized by a leucine zipper. The N-terminus of the pMHC beta-chain (DRB1*01:01) was fused to the peptide. The C-terminus of the pMHC alpha chain (DRA) was fused to a dockerin-domain from C. thermocellum, which specifically associates with corresponding cohesin domains (Coh1-Coh5) from C. thermocellum expressed as yeast-surface displayed, Aga2-fused cohesin scaffolds.

3.4.2. Protein-scaffold Directed Assembly of pMHC on a Cell Surface

To verify the specific binding of dockerin-fused pMHC with cohesin-derived protein scaffolds, soluble forms of the protein scaffolds (sAPCs) and dockerin-fused pMHC were expressed and purified in *E. coli* and insect cells, respectively (**Figure 3.3a**). The binding affinity of soluble protein scaffold (sAPC1) and dockerin-fused pMHC was measured using surface plasmon resonance (SPR) and found to be approximately 10 nM (**Figure 3.4a**). This value is consistent with reported binding affinities for other enzyme-dockerin fusions,[300] suggesting that the fusion of this dockerin to pMHC does not significantly change the affinity of the cohesin-dockerin interaction. Excess dockerin-fused pMHC was incubated with the sAPCs and complex formation was assessed by a Native-PAGE shift assay. The Native-PAGE analysis showed a complete shift of each sAPC band accompanied by the appearance of bands with increasing molecular weight in the order of sAPC1 to sAPC5 (**Figure 3.3 b and c**), indicating complete complex formation between soluble protein scaffolds and dockerin-fused pMHC.

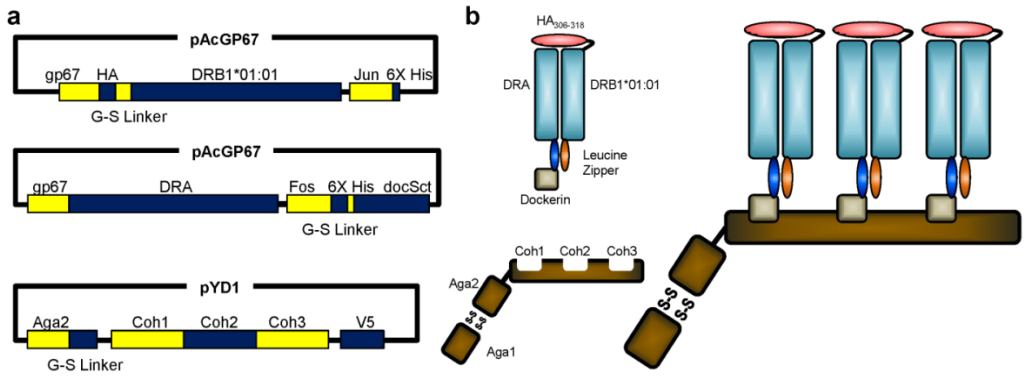

Figure 3.2. Schematic depicting the construction and assembly of recombinant pMHC and yeast-displayed scaffold.
(a) The N-terminus of the pMHC beta-chain (DRB1*01:01) is fused to the well-studied hemagglutinin peptide (HA306-318). The C-terminus of the pMHC alpha-chain (DRA) is fused to a dockerin-domain from *C. thermocellum* which specifically associates with corresponding cohesin-domains from C. thermocellum. (b) Yeast surface displayed Aga2-fused cohesin scaffolds direct the assembly of the recombinant dockerin-fused, multivalent pMHC complexes. A valency of three is shown as an example here.

To enable the assembly of pMHC on the cell surface, yeast cells were transformed with the plasmid encoding the multivalent, Aga2-fused and V5-tagged protein scaffolds. After protein induction, the transformed yAPC1 – yAPC5 were loaded with pMHC, and co-stained with fluorescent antibodies recognizing the pMHC and the V5 tag, respectively. The resulting fluorescent signals were then analyzed using flow cytometry to assess the pMHC occupancy of each surface-displayed scaffold (**Figure 3.3d**). The average pMHC occupancy of each yAPC scaffold was measured by analyzing the ratio of the pMHC signal to protein scaffold signal. These ratios were then normalized based on the valency of yAPC5.

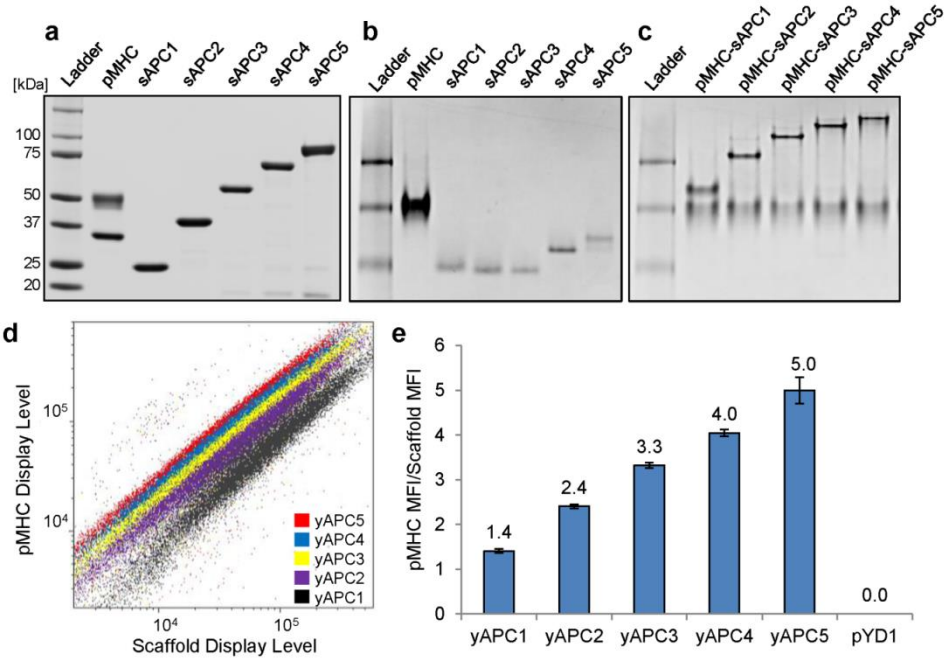

Figure 3.3. Scaffold-directed assembly of recombinant pMHC achieves expected pMHC valency.
(a) SDS-PAGE analysis and (b) Native-PAGE analysis of recombinant pMHC and soluble cohesin scaffolds. (c) Native-PAGE shift assay shows dockerin-fused pMHC forming complex with soluble cohesin-scaffolds (right). (d) Flow-cytometry dot plot showing pMHC display level plotted against scaffold display level for yeast presenting scaffolds of different valency. (e) The average number of pMHC per scaffold determined by the ratio of the median fluorescence intensity (MFI) of the bound pMHC and the MFI of the displayed scaffold. Data represent mean ± SD (n = 3). Student's t-test indicated any pair within dataset have $p < 0.05$.

The observed pMHC valency of each protein scaffold construct agreed with its designed stoichiometry, indicating that each cohesin module stably binds a dockerin-fused pMHC (**Figure 3.3e**). A yeast cell control presenting no scaffold (pYD1 in **Figure 3.3e**) was also incubated with pMHC and analyzed in the same way. No pMHC signal was detectable indicating that pMHC display is protein-scaffold dependent. The apparent binding affinity between yeast surface-displayed protein scaffolds and pMHC was measured to be 5.70 ± 1.75 nM using a flow-cytometry binding assay (**Figure 3.4b**), which was comparable to the binding affinity measured by SPR (10.00 ± 5.06 nM).

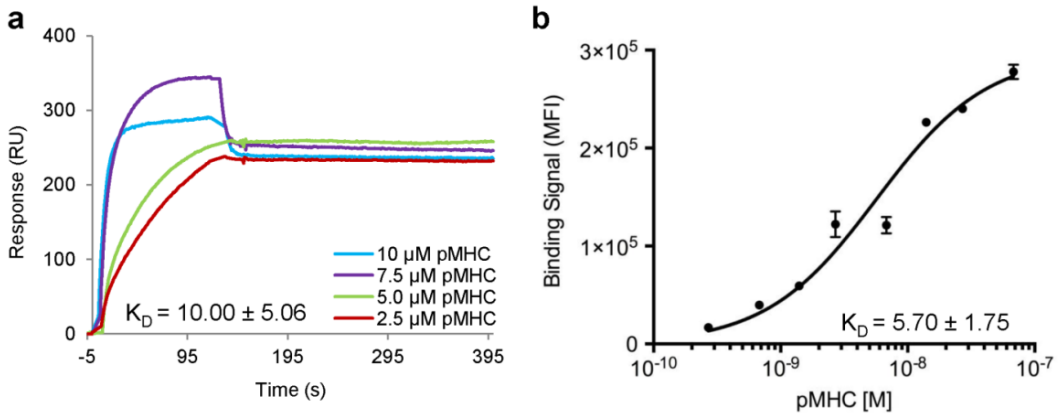

Figure 3.4. Dockerin-fused pMHC cohesin binding assays.
(a) Biacore 3000 response curves from immobilized dockerin-fused pMHC and flowing sAPC1. (b) Flow-cytometric apparent binding affinity curve between yAPC1 and dockerin-fused pMHC. The average binding affinities determined from the assays in (a) and (b) were 10.00 nM and 5.70 nM, respectively.

3.4.3. T Cell Activation by Multivalent pMHC Assembly

To ensure the functionality of the multivalent pMHC assembly, the recombinant dockerin-fused pMHC protein was first used to elicit dose-dependent, antigen-specific T cell activation. Dockerin-fused HLA-DR1 in complex with the influenza antigenic peptide[301] $HA_{306-318}$ (DR1-HA) was used to activate HA1.7 cells, a murine transgenic T cell hybridoma expressing a human α/β TCR that recognizes the DR1-HA.[302] Dockerin-fused HLA-DR1 in complex with

the invariant chain peptide[46] $CLIP_{87-101}$ (DR1-CLIP) was used as a negative control for antigen specificity. DR1-HA and DR1-CLIP were titrated and adsorbed in a 96-well polystyrene plate and incubated with HA1.7 T cells for activation. After 18 hours, IL-2 level in the supernatant was quantified using ELISA. As shown in **Figure 3.5a**, HA1.7 T cells responded to immobilized pMHC proteins in an antigen-specific, dose-dependent manner, indicating that the recombinant dockerin-fused pMHC is functional.

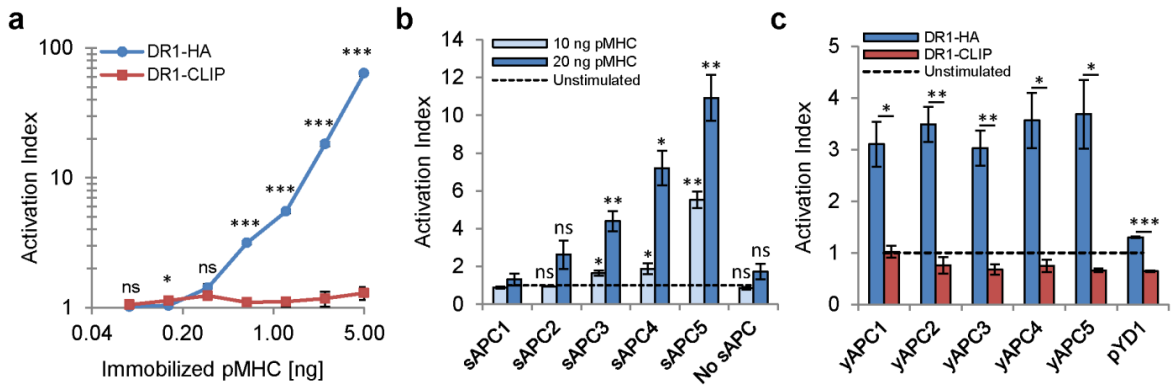

Figure 3.5. Dockerin-fused pMHC activate HA1.7 T cell hybridoma.
(a) T cell response to dockerin-fused pMHC presenting either agonist HA peptide (DR1-HA) or null CLIP peptide (DR1-CLIP) titrated and immobilized in activation plate. Activation index is the ratio of T cell IL-2 secretion over basal IL-2 signal from unstimulated control. (b) T cell response to soluble pMHC with varying valency assembled on soluble scaffold (sAPC). Soluble pMHC monomer (no sAPC) was included as a negative control. Activation was performed using either 10 ng or 20 ng pMHC. Statistical significance was determined with respect to sAPC1. (c) T cell response to dockerin-fused pMHC loaded on yeast displayed scaffolds (yAPC1 – yAPC5). yAPC1 – yAPC5 loaded with DR1-HA have statistically insignificant difference in activation, but all are statistically different from the negative control, pYD1. For a – c, data represent mean ± SD (n = 3, Student's t-test, *$p<0.05$, **$p < 0.01$, ***$p < 0.001$, not significant (ns)).

Soluble multivalent pMHC has long been known to activate T cells by cross-linking TCRs while soluble monomeric pMHC is incapable of inducing T cell activation.[80,87,223,303] To validate the pMHC-scaffold assembly scheme and test the ability of our soluble multivalent pMHC complexes to activate T cells, equal amounts of pMHC were loaded on sAPC1 – sAPC5, and the soluble pMHC-sAPC complexes were incubated with HA1.7 T cells for activation. An

equivalent amount of soluble pMHC monomer (i.e. no sAPC in **Figure 3.5b**) was included as a negative control. After 18 hours, T cell activation was assessed by quantifying IL-2 in the supernatant using ELISA. In agreement with previous studies, soluble pMHC monomer and pMHC-sAPC1 complexes failed to induce T cell IL-2 secretion (**Figure 3.5b**). Moreover, as the pMHC multivalency increased, the degree of T cell activation also increased, suggesting high pMHC multivalency on soluble complexes is more effective in cross-linking TCRs than low pMHC multivalency.

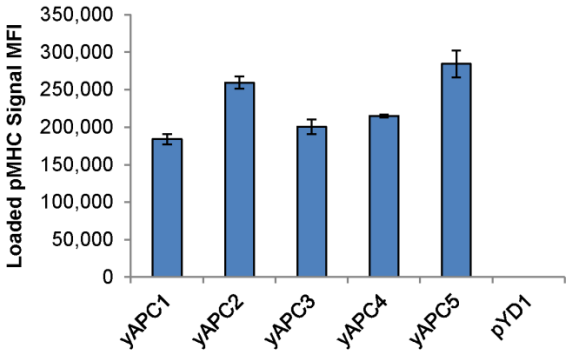

Figure 3.6. Loaded pMHC signal on unsorted yAPC.
Data represent mean ± SD (n = 3).

To further test the functionality of the protein-scaffold directed pMHC assembly on the yeast cell surface, dockerin-fused DR1-HA and dockerin-fused DR1-CLIP were loaded onto the surface of yAPC1 – yAPC5. The resulting yAPCs were then incubated with the HA1.7 T cells at a 10:1 ratio for 18 hours, and the IL-2 secretion was quantified using ELISA. Each yAPC construct presenting agonist DR1-HA produced measurable IL-2 secretion while each yAPC construct presenting DR1-CLIP did not (**Figure 3.5c**). The yeast cell displaying no protein scaffold (pYD1 in **Figure 3.5c**) was also included for both DR1-HA and DR1-CLIP, and neither produced measurable IL-2 secretion. These results suggest that the yeast cells do not non-specifically activate the T cells, and pMHC organized on yeast-displayed protein scaffolds can

induce antigen-specific T cell activation. Interestingly, pMHC valency did not significantly influence the IL-2 secretion by T cells as yAPC1 – yAPC5 induced comparable T cell activation after 18 h. This observation could be a result of the natural variation in protein scaffold expression producing similar global pMHC surface densities on each yAPC construct (**Figure 3.4d** and **Figure 3.6**). Therefore, we next aimed to tune the pMHC surface density on the yAPC constructs.

3.4.4. FACS-facilitated Tuning of Global pMHC Surface Density

To control the global pMHC surface density, we stained pMHC-loaded yAPC1 – yAPC5 with anti-His fluorescent antibodies and used FACS to isolate yAPC populations with homogeneous pMHC surface densities. As shown in **Figure 3.7a**, four gates corresponding to four different pMHC surface densities were used to sort yAPC1 – yAPC5.

This allowed the same pMHC surface density to be obtained for each pMHC valency. The sorted yAPCs were reanalyzed using flow cytometry to confirm that the pMHC surface density was indeed consistent between yAPC1 – yAPC5 (**Figure 3.7b**). Fluorescence quantitation beads were used to convert fluorescence intensity into the average pMHC surface density for each yAPC population using Equation 3.1 below (**Figure 3.7c**). This process was repeated using yAPCs treated with varying concentrations of Tris(2-carboxyethyl)phosphine hydrochloride (TCEP) prior to pMHC loading. TCEP treatment releases a fraction of protein scaffold from the yeast cell surface, broadening the range of possible pMHC surface densities (**Figure 3.8**).

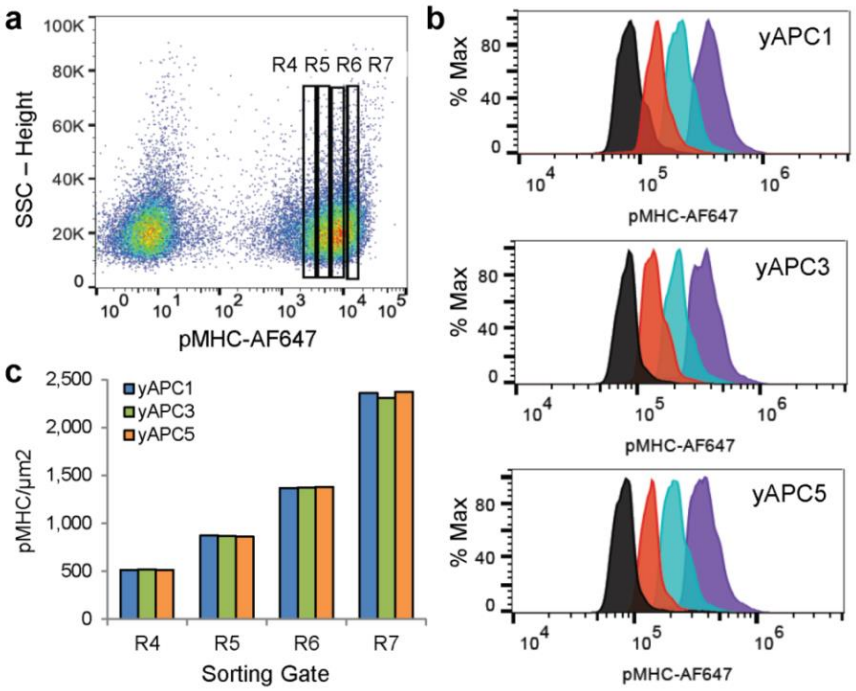

Figure 3.7. Fluorescence activated cell sorting (FACS) of yAPC based on pMHC surface density.
(a) pMHC-loaded yAPC sorted into populations with different pMHC surface densities (low – R4, high – R7). (b) Sorted yAPC1 (top), yAPC3 (middle), yAPC5 (bottom) populations analyzed using flow cytometry (left to right R4 – black, R5 – red, R6 – cyan, R7 – purple. (c) Quantification of pMHC surface density of sorted populations. All yAPC were subjected to the same treatment, yAPC2 and 4 are not shown for simplicity.

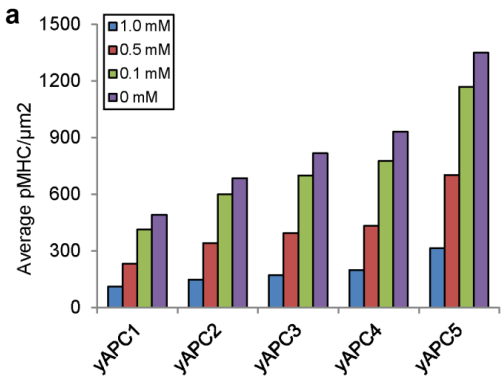

Figure 3.8. Average pMHC surface density after TCEP treatment.

3.4.5. Relationship between pMHC Surface Density and Protein Scaffold Spacing

To calculate pMHC surface density, quantitative flow cytometry was performed using fluorescence quantitation beads. Specifically, yAPCs loaded with pMHC were stained with Alexa Fluor 647-labeled anti-His antibody and the resulting median fluorescence intensity (MFI) was measured on a flow cytometer. Note that each pMHC molecule has two His tags (**Figure 3.2a**). In parallel, fluorescence quantitation beads labeled with known numbers of molecules of equivalent soluble fluorophore (MESF) were analyzed by flow cytometry to convert MFI to the number of pMHC per yAPC surface (**Figure 3.9**). The function relating MESF to MFI was determined independently for each experiment. Yeast cells were assumed to be spheres of radius R = 2 μm (ref[304] and **Figure 3.10**) and the pMHC surface density was calculated as:

$$pMHC\ Surface\ Density = \frac{A*MFI_{yAPC}+B}{2\beta*4\pi R^2} \quad (3.1)$$

where MFI_{yAPC} represents the MFI of pMHC-loaded yAPC, β represents the degree of fluorescence labeling of the anti-His antibody, and *A* and *B* are the slope and intercept, respectively, provided by the MESF vs. MFI function shown in **Figure 3.9**.

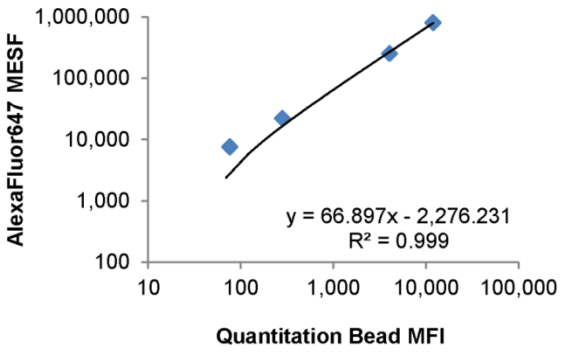

Figure 3.9. Example MESF vs. MFI standard curve.
Curve is used to define relationship between MESF and quantitation bead MFI, allowing calculation of pMHC surface density.

Next, the protein scaffold surface density ρ (i.e. number of protein scaffold / yAPC surface area) was calculated by dividing the pMHC surface density by the valency of each yAPC construct. Because the protein scaffold was assumed to be randomly distributed across the cell surface (**Figure 3.10**), the probability that a protein scaffold is *s* distance away from its nearest neighbor was calculated using the Poisson distribution $P(s) = 2\pi s\rho e^{-\pi\rho s^2}$. Integrating this function from zero to infinity provides the average protein scaffold distance to nearest neighbor (i.e. protein scaffold spacing), $\bar{s}$:

$$\bar{s} = \frac{1}{2\sqrt{\rho}} \tag{3.2}$$

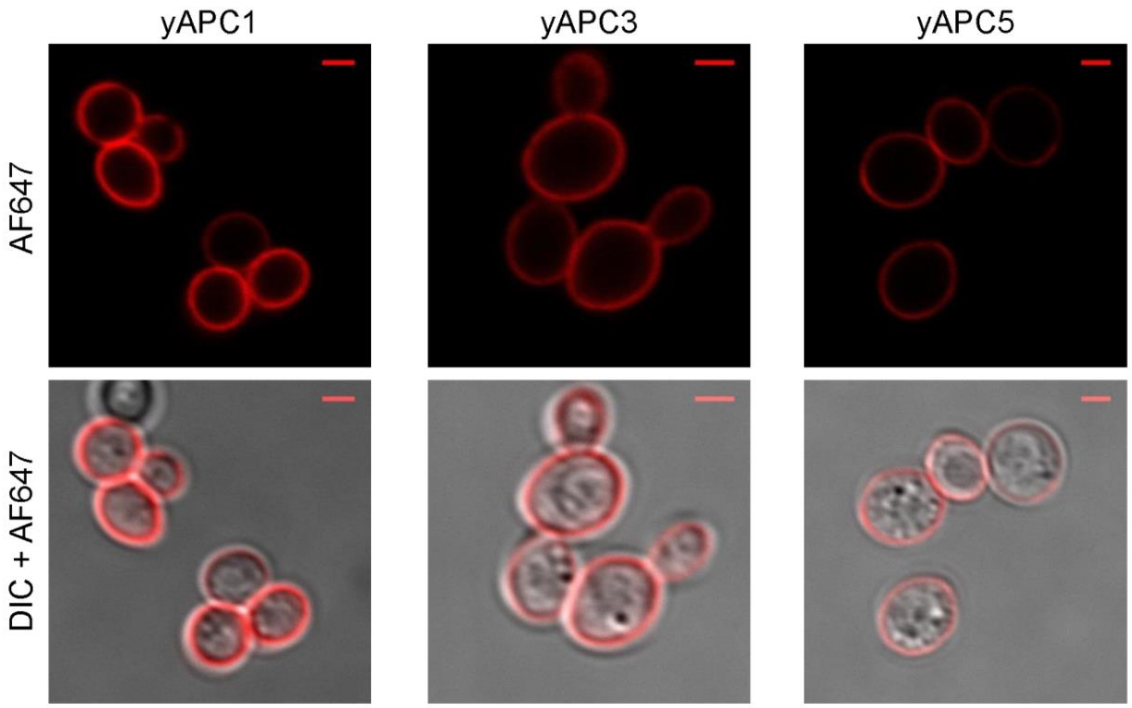

Figure 3.10. Confocal microscopy of yAPC1, yAPC3, yAPC5.
Scaffold protein is stained with Alexa Fluor 647 (AF647) (top) and its expression is approximately uniform across yAPC surface. Fluorescent and DIC overlay shown in bottom. The scale bar in each figure is 2 μm.

3.4.6. Minimum pMHC Requirement for T Cell Activation

After generating yAPC populations with defined pMHC surface densities and valencies, these well-characterized yAPCs were used to determine how global pMHC surface density, protein scaffold spacing and pMHC valency influence the T cell activation threshold. T cell activation was assessed by measuring IL-2 in the supernatant after 18 hours and plotted as a function of protein scaffold spacing for each pMHC valency (yAPC1 – yAPC5) **(Figure 3.11a**). In agreement with previous results obtained using 2D systems,[188] monovalent pMHC (i.e. yAPC1) spacing was found to inversely correlate with T cell activation. This inverse correlation was also observed for higher valencies (yAPC2 – yAPC5); however, the decrease was more gradual suggesting that increased pMHC valency can compensate for greater protein scaffold spacing.

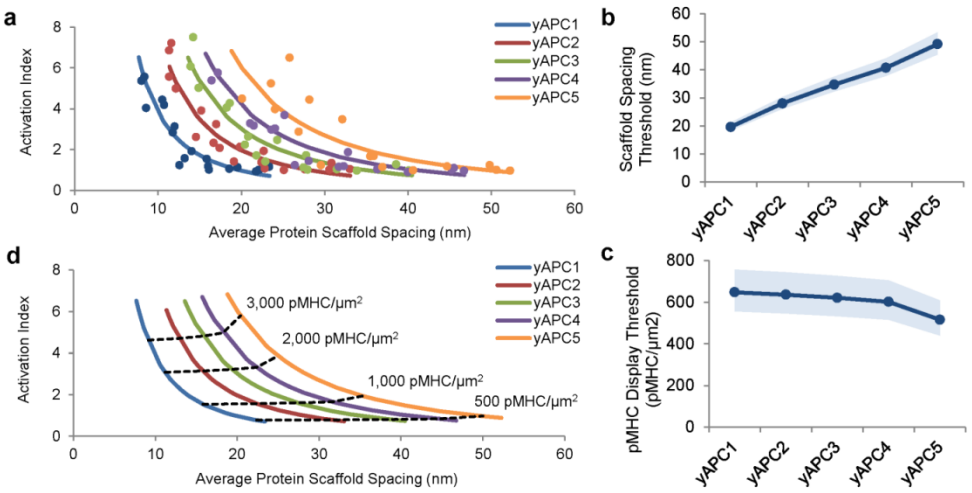

Figure 3.11. T cell response to global pMHC surface density and local pMHC valency. (a) T cell IL-2 secretion plotted against average scaffold spacing for each yAPC. Regression lines fitted using log-log transformation and linear regression. (b) Using the regressions fitted in (a), the minimum scaffold spacing required for T cell activation plotted for each pMHC valency. The shaded regions represent 95% confidence intervals. (c) Assuming uniform scaffold distribution, the minimum, global pMHC density/μm2 required for T cell activation plotted as a function of pMHC valency. The shaded regions represent 95% confidence interval. (d) Regression of T cell activation index plotted against average scaffold spacing showing lines of constant pMHC surface density.

To interpolate the T cell activation threshold, linear regression was performed on the log-log transformed data set of activation index and protein scaffold spacing for each yAPC (see methods for details). Using these regression equations, the protein scaffold spacing at which IL-2 secretion became undetectable (i.e. equal to unstimulated T cells) was determined. This scaffold spacing threshold depended linearly on pMHC valency, ranging from ~ 19.6 nm for yAPC1 to ~ 49.2 nm for yAPC5 (**Figure 3.11b**). The pMHC surface density threshold was then calculated for each yAPC construct using Equation 3.2, and was found to be independent of pMHC valency (**Figure 3.11** c and d).

Although we observed that the T cell activation threshold is independent of pMHC valency on the yeast cell surface, at high pMHC surface densities yAPC5 appeared to enhance T cell response (**Figure 3.11d**), indicating that pMHC valency may have a secondary effect on T cell activation. While these results agree with previous studies using ligands anchored on 2D surfaces,[186] they differ from our results using soluble multivalent pMHC complexes (**Figure 3.5b**) as well as previous studies,[223] suggesting that T cells respond to TCR ligand valency differently in soluble and surface-bound contexts. This notion is supported by the well-established finding that surface-anchored monomeric pMHC induces T cell activation while soluble monomeric pMHC does not.[80,87,223,303] It is also possible that the relatively weak relationship between T cell activation and pMHC valency on the yeast cell surface observed in this study is due to the limited pMHC valencies tested. Here, the maximum pMHC valency investigated was five; however, TCRs in nature are clustered at a valency of 7 – 20 following pMHC engagement.[305] Therefore, further investigation using higher valency scaffolds (e.g. yAPC6, yAPC7, etc.) would be necessary to determine the extent to which pMHC valency on a 3D surface might enhance T cell response.

The observation of a minimum pMHC requirement for T cell activation is consistent with previously published findings using lithographically patterned surfaces.[186] However, the minimum pMHC surface density required for T cell activation on the 3D yAPC surface was significantly higher than that required on 2D planes (**Table 3.1**). This discrepancy is likely related to the geometric differences between 2D and 3D systems. In the absence of adhesion and costimulatory molecules, pMHC must function as both the adhesion and stimulatory ligand. The "adhesion" role of pMHC is less important for 2D antigen presentation surfaces as their planar geometry allows for sustained interfacial contact between T cells and the antigen-presenting surface. In contrast, such contact is not assured when T cells are activated by pMHC presented on a 3D surface. Therefore, greater pMHC surface densities are required for antigen presentation on a 3D surface to maintain productive T cell-APC contacts leading to full T cell activation.

Given the abundance of costimulatory and adhesion molecules that participate in T cell activation *in vivo*, we hypothesized that the T cell activation threshold could be reduced by presenting ICAM-1 with pMHC. Further, based on our ability to tune T cell IL-2 secretion by manipulating the spatial organization of pMHC, we believed that T cell IL-2 secretion could also be controlled by manipulating the pMHC-ICAM-1 display ratio. To test these hypotheses, we co-assembled pMHC and ICAM-1 on yAPCs.

3.4.7. Protein-scaffold Directed Co-assembly of pMHC and ICAM-1

The extracellular domain of ICAM-1 was fused to the same C-terminal dockerin as the pMHC to allow for co-assembly on the yAPC-displayed scaffolds. Dockerin-fused ICAM-1 was analyzed using SDS-PAGE to verify purity and size (**Figure 3.12** a and b). The apparent binding affinity of dockerin-fused ICAM-1 for the yAPC cohesin-scaffold was measured using a flow-

cytometry based binding assay (**Figure 3.12c**) and found to be slightly higher than the dockerin-fused pMHC (5.60 nM for the pMHC vs. 1.21 nM for ICAM-1). The slightly higher binding affinity of ICAM-1 could be a result of its elongated structure, which may be less prone to steric hindrance than the bulkier heterodimeric pMHC.

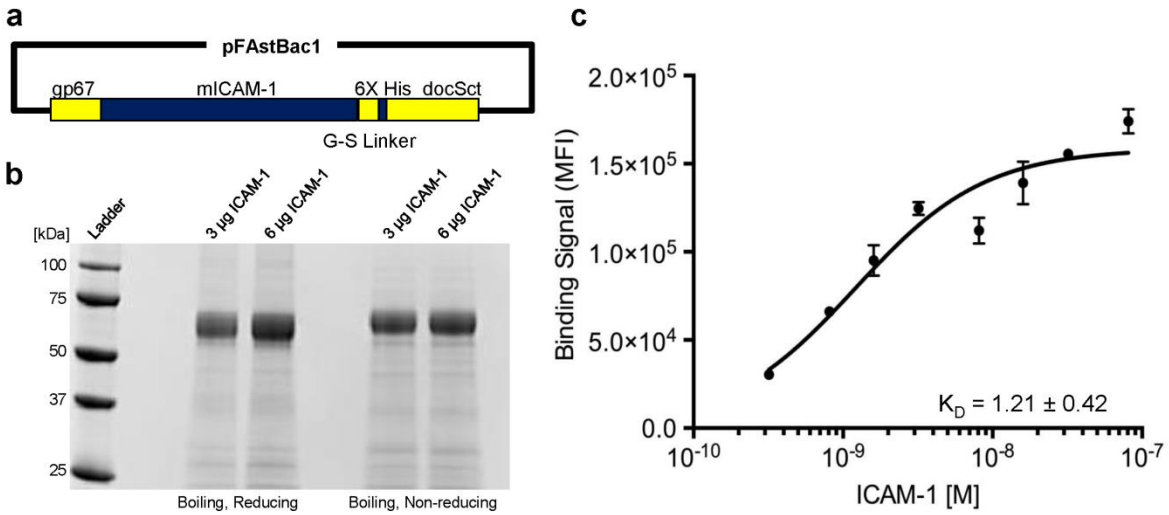

Figure 3.12. Construction and characterization of dockerin-fused ICAM-1.
(a) Schematic showing the design of recombinant ICAM-1. (b) SDS-PAGE analysis of purified dockerin-fused ICAM-1. (c) Flow-cytometry apparent binding affinity curve between yAPC1 and dockerin-fused ICAM-1.The average binding affinity determined from the assay in (c) was 1.21 nM.

The effect of pMHC-ICAM-1 co-assembly on T cell activation was assessed by loading various ratios of pMHC and ICAM-1 on unsorted yAPC1, yAPC3, and yAPC5. The fractional occupancy of pMHC and ICAM-1 on the surface of yAPCs was determined by flow cytometry (**Figure 3.13**), and the characterized yAPCs were used for T cell activation. For pMHC-ICAM-1 co-assembly, T cell activation increased sharply as the fraction of pMHC increased from 0 to 15% and then gradually decreased up to 100% pMHC (**Figure 3.14a**). This optimum assembly ratio of approximately 15% pMHC, 85% ICAM-1 was observed for each yAPC construct, and thus deemed independent of valency (**Figure 3.14a**). This optimum suggests that 15% pMHC is

sufficient to trigger widespread TCR signaling, which not only initiates T cell activation but also promotes stronger LFA-1-ICAM-1 binding by inducing a conformational change in LFA-1.[306–310] This synergistic interaction led to a ~ 3-fold increase in maximum T cell activation despite presenting ~ 6-fold less pMHC (**Figure 3.14a** vs. **Figure 3.11a**). It is worth noting that in addition to mediating intercellular adhesion, ICAM-1-LFA-1 binding has also been shown to sustain intracellular calcium flux that is required for T cell activation.[122] As a result, ICAM-1 exhibits characteristics of both adhesion and costimulatory molecules,[115,311] which might explain the synergy that produced the ~ 3-fold increase in T cell activation by the pMHC-ICAM-1 co-assemblies.

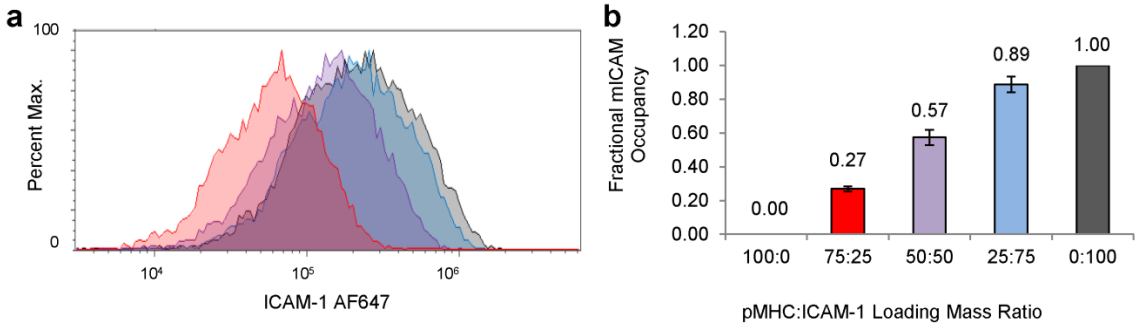

Figure 3.13. Determining fractional ICAM-1 display ratio using flow cytometry.
(a) Flow cytometer histogram corresponding to ICAM-1 signal observed for yAPC1 loaded with various pMHC:ICAM-1 mass ratios (red: 75:25; purple: 50:50; blue: 25:75; gray: 0:100). (b) The actual fractional ICAM-1 occupancy was found by dividing the MFI for each mass-loading ratio by the MFI observed when only ICAM-1 was loaded (0:100).

The T cell activation threshold for the pMHC-ICAM-1 co-assembly was determined by first loading yAPC1, yAPC3, and yAPC5 with 15% pMHC and 85% ICAM-1 (**Figure 3.15a**). The loaded yAPCs were then stained with a fluorescent anti-His antibody and sorted to isolate homogenous yAPC populations with defined total ligand surface densities (**Figure 3.15b**). T cell activation by these yAPC populations was assessed by measuring IL-2 secretion after 18 h using ELISA and plotted against the global pMHC surface density (**Figure 3.14b**). Similar to the

results for T cell activation by pMHC alone (**Figure 3.11c**), the pMHC surface density threshold for the co-assembly did not depend on valency (**Figure 3.14c** and d and **Figure 3.16**).

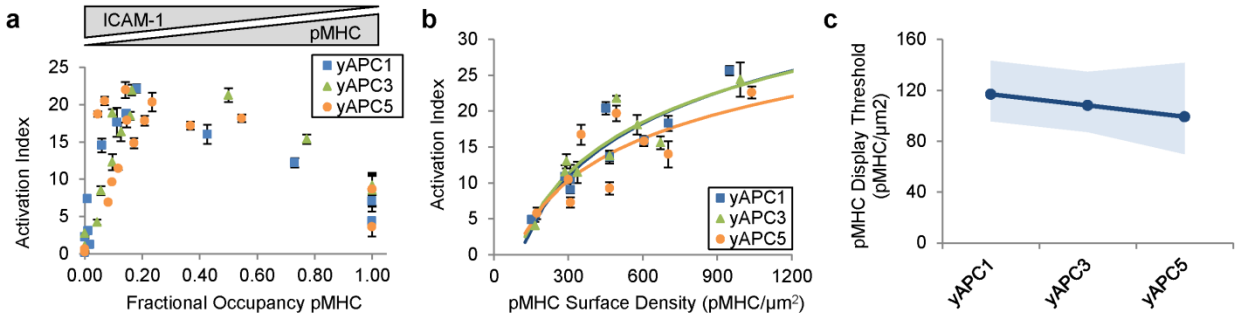

Figure 3.14. T cell response to yAPC displaying the coassembly of pMHC and ICAM-1.
(a) T cell response to unsorted yAPC1, yAPC3, and yAPC5 loaded with various ratios of pMHC and ICAM-1. (b) T cell activation index plotted against global pMHC surface density for sorted yAPC1, yAPC3, and yAPC5 loaded with 85% ICAM-1 and 15% pMHC. The yAPCs were sorted based on fixed overall protein display levels. (c) Solid lines represent

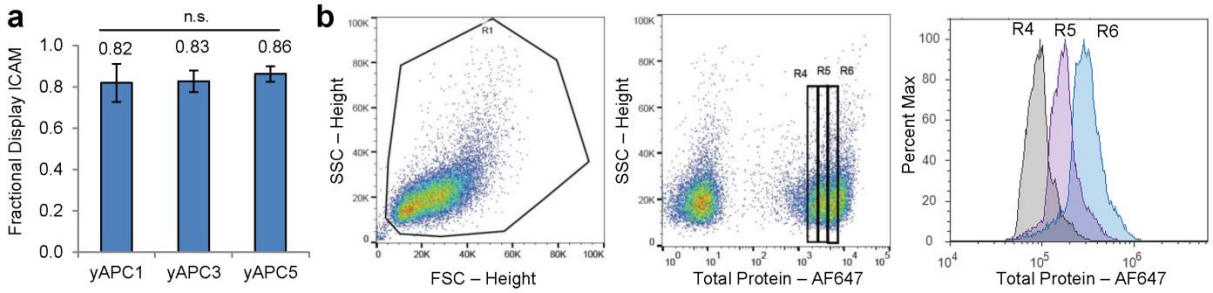

Figure 3.15. ICAM-pMHC co-display characterization.
(a) Optimum surface occupancy of 85% ICAM-1 can be reproducibly obtained for yAPC1, yAPC3, and yAPC5. (b) yAPC codisplaying ICAM-1 and pMHC were sorted to isolate populations with defined total protein display levels (Middle: R4, R5, R6). Uniformity of sorted yAPC total protein display level was verified by flow cytometric analysis (right). Plots shown are of yAPC1 for simplicity. For (a), data represent mean ± SD (n = 3).

As we hypothesized, the presence of ICAM-1 reduced the pMHC surface density threshold for T cell activation approximately 6-fold to 92 – 122 pMHC/μm^2, which is comparable to that reported for planar systems (**Table 3.1**). This observation supports our

hypothesis that sustained intercellular contact is critical for efficient T cell activation, and that ICAM-1 mediates this contact more effectively than pMHC alone on 3D antigen-presenting surfaces. In addition to maintaining intercellular contact, fine-tuning the stoichiometric ratio of adhesion and stimulatory T cell ligands may also be useful in directing T cells towards an optimum phenotype. For example, ICAM-1 has been shown to drive $CD4^+$ T cells towards a Th1 phenotype[114,312] and additional studies of other costimulatory molecules may provide insights that are relevant to the design of future T cell immunotherapeutics and their large-scale manufacture.

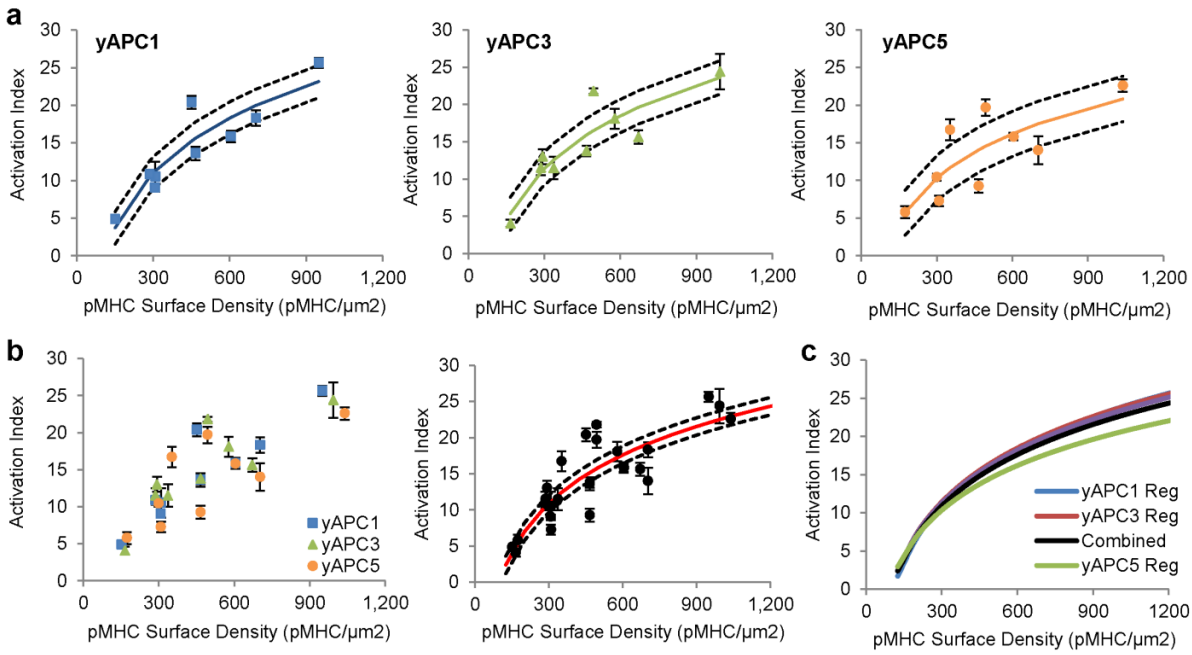

Figure 3.16. Activation index plotted with respect to pMHC surface density for yAPC codisplaying 85% ICAM-1 and 15% pMHC.
(a) T cell activation index plotted with respect to pMHC surface density when stimulated by yAPC1, yAPC3, and yAPC5 displaying 85% ICAM-1. Solid lines represent logarithmic regression lines and dashed lines correspond to 95% confidence intervals for the regressions. (b) Total (left) and valency-independent (right) T cell activation index plotted with respect to pMHC surface density. Solid line represents valency-independent logarithmic regression line and dashed lines correspond to 95% confidence intervals for the regression. (c) Logarithmic regression lines overlay for T cell activation index vs. pMHC surface density for yAPC1 (blue) yAPC3 (red) yAPC5 (green) and all yAPC combined (black) displaying 85% ICAM-1.

In this work, we developed a novel strategy for controlling the valency, surface density, and stoichiometric ratio of T cell ligands on a 3D yeast cell surface using protein-scaffold directed assembly. Using the engineered yeast as artificial antigen presentation cells, we observed that the T cell activation threshold is determined by a minimum global pMHC surface density and independent of pMHC valency. Further, we found that T cell activation is maximized when pMHC and ICAM-1 are co-assembled with a presentation ratio of 15% and 85%, respectively. In addition to increasing the magnitude of T cell activation, co-assembly of 85% ICAM-1 enhanced T cell sensitivity to antigen by 6-fold. Taken together, these results suggest that adhesion molecules like ICAM-1 play an especially important role in 3D antigen presentation, as they maintain productive intercellular contacts necessary for T cell activation. As a result, the stoichiometric ratio between adhesion and stimulatory molecules should be carefully considered when designing future 3D antigen presenting systems. Finally, we believe the platform technology described here has applications beyond T cell antigen presentation, as it can be used for nanoscale patterning of any proteins of interest on any surfaces of interest.

Table 3.1. T cell activation thresholds observed for various antigen presentation systems.

TCR Ligand	Costimulatory Ligand	Activation Readout	Patterning Technique	Spacing Threshold	Density Threshold	Reference
pMHC	None	Contact area, IL-2 secretion	Lithography	100 – 150 nm	90 – 140/μm^2	[186]
aCD3 (OKT3)	aCD28	IL-2 secretion, Proliferation	Lithography	> 150 nm	N/A	[187]
aCD3 (UCHT1 Fab_2)	ICAM-1	pY intensity	Lithography	34 – 69 nm	N/A	[188]
aCD3 (UCHT1 Fab)	ICAM-1	pY intensity	Lithography	100 nm	115/μm^2	[189]
pMHC	None	IL-2 secretion	Scaffold-directed assembly	18 – 21 nm*	550 – 650/μm^2	This work
pMHC	ICAM-1	IL-2 secretion	Scaffold-directed assembly	45 – 52 nm*	92 – 122/μm^2	This work

*Spacing threshold determined for monovalent yAPC1

3.5. Conclusions and Outlook

Controlling T cell activation is a fundamental aspect of T cell immunotherapy, as T cell activation leads to T cell expansion, differentiation, and the execution of effector functions. Over the past twenty years, researchers have shown that T cell activation can be controlled by the manipulating spatial organization of TCR ligands and costimulatory molecules. A number of studies have shown that focal patterning of TCR ligands surrounded by costimulatory ligands resembling the immunological synapse produces more potent T cell stimulation than colocalization of the same molecules.[190,194,198,281] Similarly, a series of studies using lithographically patterned surfaces have clearly shown that T cell activation can be finely tuned by controlling the spatial distribution of TCR ligands on a patterned surface.[186–189,193] While such

studies have provided invaluable insight into the molecular and signaling mechanisms that produce T cell activation,[104,105,108] they have largely relied on 2D, planar antigen presentation surfaces. The geometry of such systems stands in sharp contrast to the 3D geometry of antigen presenting cells in the body. For example, planar systems present antigen such that the molecules are all oriented in the same direction (*i.e.* perpendicular to the surface) and provide sustained interfacial contact between T cells and the surface through gravity. In contrast, the orientation of antigen presented on 3D APCs in the body is much less uniform, and interfacial contact between T cells and antigen presenting cells is mediated by molecular interactions without assistance from gravity. Thus far, technological limitations have restricted the control over the spatial organization of T cell ligands on 3D surfaces to large, multi-micron diameter patches.[288] As a result, the extent to which insights (*e.g.* minimum pMHC requirement for activation, optimum ratio of TCR ligands and costimulatory molecules, effect of pMHC/TCR ligand valency, etc.) gained using planar systems are transferrable to 3D cell-cell interactions is not well understood.

Here, we developed a modular artificial antigen presentation system based on cohesin-dockerin binding that provides nanoscale control over the spatial organization of T cell ligands on a 3D yeast cell surface. Using this system, we showed that the minimum pMHC requirement for T cell activation is approximately six-fold greater on a 3D surface than on a planar surface, in the absence of costimulatory and adhesion molecules (**Table 3.1**). This result suggests that sustained interfacial contact is an important parameter for T cell activation, and that planar antigen presentation systems underestimate the pMHC surface density required for T cell activation on 3D surfaces in the absence of costimulatory and/or adhesion molecules. Further, using yAPCs we found that T cell activation intensity as measured by IL-2 secretion is independent of pMHC valency and instead determined by the overall pMHC surface density.

This observation stands in contrast to our results using soluble multivalent pMHC (**Figure 3.5b)** indicating that T cells integrate soluble and surface-displayed pMHC signals differently.

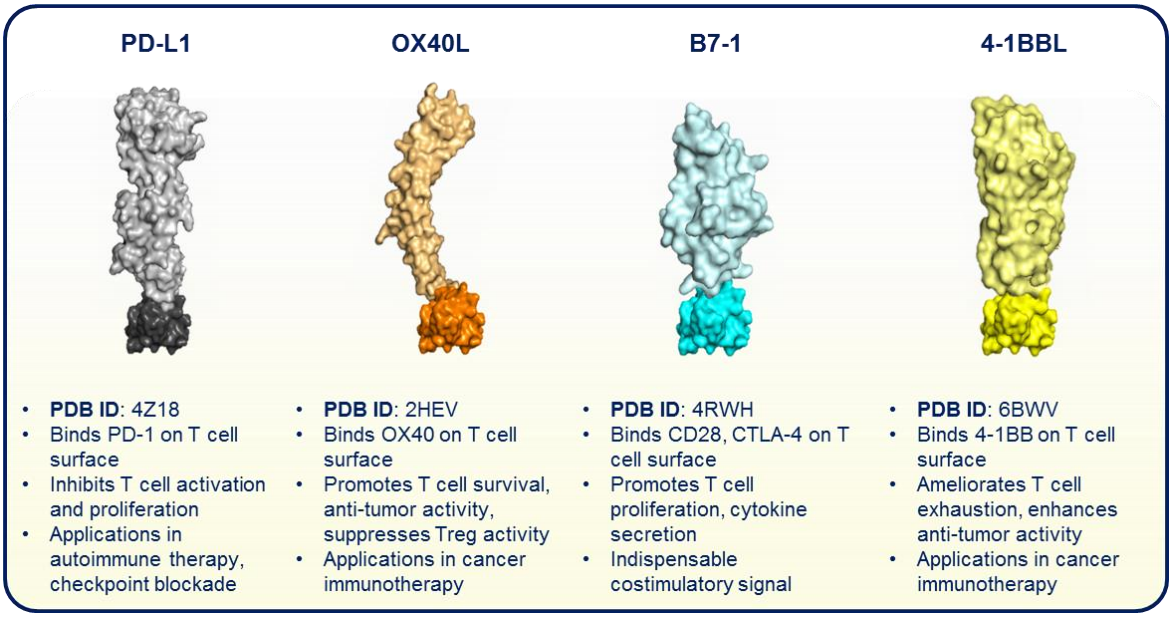

Figure 3.17. Schematic of dockerin-fused costimulatory molecules and their potential uses. These molecules have been engineered for expression in insect cells and will be used with functionalized cohesin scaffolds in the next phase of our comprehensive study on how the spatial and stoichiometric organization of T cell ligands affects T cell phenotype and function.

Using this system, we also found that T cells are maximally activated by yAPCs presenting 15% pMHC and 85% ICAM-1, exhibiting up to six-times greater IL-2 secretion than when activated by pMHC alone. This observation reveals that T cell activation can be controlled by modulating the stoichiometric ratio of pMHC and costimulatory/adhesion molecules, in addition to controlling the spatial organization of T cell ligands. Taken together, these results demonstrate that modular artificial antigen presentation based on protein-scaffold directed assembly allows for the systematic investigation of how the spatial and stoichiometric organization of T cell ligands affects T cell activation.

Building on this concept, we have designed and engineered a panel of additional dockerin-fused costimulatory/coinhibitory molecules including PD-L1, OX40L, B7-1, and 4-

1BBL (**Figure 3.17**). Using these molecules, we plan to conduct additional experiments, continuing our investigation of how the stoichiometric ratio of pMHC and costimulatory T cell ligands influences T cell activation, phenotype, and effector function. To accomplish this goal, we plan to couple our analysis of cytokine secretion with T cell proliferation assays and more detailed, high-dimensional phenotypic analysis using cytometry by time of flight (CyTOF). Together these tools should provide a comprehensive strategy for understanding how T cells integrate and ultimately respond to combinations of costimulatory/inhibitory signals of varying magnitudes.

Given the importance of T cell phenotype and effector function in T cell immunotherapy, robust molecular tools capable of finely tuning the signals that shape these parameters has significant therapeutic and research potential. We believe that the cohesin-dockerin based protein assembly strategy introduced in this chapter offers a robust toolset for modulating antigen presentation to T cells on 3D surfaces. Moreover, when coupled with high-dimensional phenotypic analysis via CyTOF, systematic studies of T cell activation using highly organized cohesin-dockerin based assemblies will provide a more comprehensive understanding of how T cells integrate stimulatory and costimulatory signals. Such studies should yield valuable insight for the development of next generation of off-the-shelf artificial antigen presenting cells to tailor to the phenotype and function of T cells for specific immunotherapeutic and research applications.

3.6. Materials and Methods

3.6.1. Design of pMHC, ICAM-1, and Cohesin Scaffolds

Recombinant pMHC fusion proteins were assembled by first isolating the extracellular domains of HLA-DRA (UniProt: P01903, residues 26-216) and HLA-DRB1*01:01 (UniProt: P04229, residues 30-227). The leucine zipper dimerization motifs Fos and Jun were fused to the C-terminus of the extracellular DRA and DRB1 chains, respectively, in lieu of the native transmembrane domains as described.[313] A dockerin domain from *C. thermocellum* (UniProt: A3DH67, residues 673-741) was fused to the C-terminus of the DRA construct via a 6X-Histidine tag. Two forms of the DRB1 chain were engineered. One DRB1*01:01 construct was fused to the invariant chain $CLIP_{87\text{-}101}$ peptide via a cleavable thrombin linker as described[276] and one DRB1*01:01 construct was fused to the well-characterized influenza antigen $HA_{306\text{-}318}$ via the same cleavable thrombin linker. The C-terminus of both DRB1*01:01 constructs were fused to a 6X-Histidine tag for purification and detection. The N-terminus of each dimeric chain was fused to the baculovirus gp64 signal peptide and ligated into separate baculovirus transfer vectors pAcGP67A (BaculoGold Baculovirus Expression System, Pharmingen BD Biosciences, San Jose, CA). The integrity of each DNA sequence was confirmed using Sanger sequencing.

The murine intercellular adhesion molecule 1 (ICAM-1) was designed similarly. The DNA sequence coding the extracellular domain of ICAM-1 (UniProt: P13597, residues 28-485) was fused to the same *C. thermocellum* dockerin as DRA via a 6X-Histidine tag for purification and detection. The N-terminus of the ICAM-1 was fused to the baculovirus gp64 signal peptide and ligated into the baculovirus transfer vector pFastBac1 (Bac-to-Bac Baculovirus Expression Systems, Life Technologies). Separate baculovirus expression systems were used for pMHC and

ICAM-1 because of the discontinuation of the BaculoGold linearized baculovirus DNA. The difference did not affect protein expression.

Protein scaffolds were designed by recombining the sequences coding for the first three cohesins of the CipA cellulosome from *C. thermocellum*. Soluble protein scaffolds are denoted with the prefix "s"APC and yeast-displayed scaffolds are denoted with the prefix "y"APC. sAPC1/yAPC1 consisted of Coh1 (UniProt: Q06851, residues 29-182), sAPC2/yAPC2 consisted of Coh1 and Coh2 (UniProt: Q06851, residues 29-322), and sAPC3/yAPC3 consisted of Coh1, Coh2, and Coh3 (UniProt: Q06851, residues 29-183 and residues 560-704). sAPC4/yAPC4 and sAPC5/yAPC5 contained the sAPC3 sequence fused to additional cohesins through a G-S-S-S linker (sAPC4: Coh1, Coh2, Coh3, and Coh1; sAPC5 Coh1, Coh2, Coh3, and Coh1, Coh2). All soluble protein scaffolds were ligated into the bacteria expression plasmid pET28a (Novagen) with a kanamycin resistance selectable marker. Yeast-displayed scaffolds were ligated into a modified form of the yeast surface display plasmid pYD1 (Invitrogen) with ampicillin resistance and tryptophan auxotrophic selectable markers and fused to an N-terminal Aga2 domain and a C-terminal V5 epitope tag for detection. All plasmids were propagated in the *E. coli* strain *Mach1*. All plasmids were sequenced using Sanger DNA sequencing for verification.

3.6.2. Baculovirus Transfection and pMHC, ICAM-1 Purification

Spodoptera frugiperda (SF9) insect cells were co-transfected with either the DRA or DRB1 baculovirus transfer vectors and linearized Baculovirus DNA (Pharmingen BD BaculoGold Biosciences, San Jose, CA) using Cellfectin II (Invitrogen) according to the manufacturer's protocol. The recombinant DRA and DRB1 baculoviruses generated from transfection were amplified separately in SF9 cells to create high-titer P1 viral stocks. pMHC

was expressed by co-infecting High-Five cells at a density of 2.0 M/mL with equal volumes of high-titer DRA and DRB1 baculovirus stocks. Multiplicity of infection was optimized as described.[205] Recombinant pMHC was harvested after 72 h and purified using affinity chromatography with Ni-NTA beads according to the manufacturer's protocol (Qiagen). The ICAM-1 baculovirus transfer vector was transformed into the *E. coli* strain DH10Bac (Bac-to-Bac Baculovirus Expression Systems, Life Technologies). Bacmid recombination was established via blue/white colony screening and PCR recombination checks as described in the manufacturer's protocol. Recombinant baculovirus DNA was purified using PureLink HiPure Plasmid miniprep kit (Invitrogen). ICAM-1 bacmid was used to transfect SF9 cells with Cellfectin II. The recombinant baculovirus generated from transfection was amplified in SF9 cells to obtain a high-titer P1 baculovirus stock. ICAM-1 was expressed by infecting High-Five cells at a density of 2.0 M/mL with high-titer ICAM-1 baculovirus stock. Recombinant ICAM-1 was purified in the same way as pMHC. SDS-PAGE analysis was performed to verify protein purity (**Figure 3.12b**).

3.6.3. Scaffold Purification and Scaffold-Directed Protein Complex Assembly

Plasmids coding for the soluble protein scaffolds were used to transform the *E. coli* strain BL21. Soluble protein scaffold expression was induced by addition of 0.1 mM IPTG in LB media when the BL21 culture reached an OD600 between 0.6 and 0.8. The induced-BL21 were cultured for 16 h at 16°C. Soluble protein scaffold was harvested by lysing the BL21 via sonication and performing affinity chromatography on the lysate using a 5 mL HisTrap column (GE Healthcare Life Sciences). The purified soluble protein scaffolds were analyzed using SDS-PAGE (**Figure 3.3a**) to verify protein purity.

To verify the scaffold-directed assembly of recombinant dockerin-fused pMHC, approximately 1.0 μg of each soluble protein scaffold construct (sAPC1 – sAPC5) was incubated with excess pMHC in 50 mM Na_3PO_4 at 30°C over 2 h. pMHC was added step-wise every 30 minutes over the 2 h incubation time. Complex formation was assessed by Native-PAGE analysis. Briefly, the protein-complexes were run on an 8% Tris-Glycine gel at 130V for 2 h 15 min and stained using SimplyBlue SafeStain. Protein-complex formation was assessed by observing a total shift of the soluble protein scaffold band.

Plasmids coding for yeast-displayed scaffolds were used to transform the *S. cerevisiae* strain EBY100. Transformants were selected by plating on tryptophan-dropout media. Transformed yeast were cultured to an OD600 of 4.0 in tryptophan-dropout media and then scaffold-expression was induced by transferring the yeast to galactose-rich media for 48 h at 20°C. After induction, 500,000 of each yAPC (yAPC1 – yAPC5) were incubated with excess pMHC in 0.5% bovine serum albumin (BSA) at 4°C overnight. The yAPC were then washed twice with 0.5% BSA and co-stained with anti-His conjugated to PE (BioLegend) and anti-V5 conjugated to Alexa Fluor 647 (Invitrogen) for 1 h. The co-stained cells were then analyzed using flow cytometry. pMHC valency was determined by analyzing the ratio of pMHC (His) to scaffold (V5) median fluorescence intensities.

3.6.4. Fluorescent Activated Cell Sorting (FACS)

yAPC1 – yAPC5 were prepared for FACS by initial fixation with 0.1% paraformaldehyde (PFA) for 15 minutes at room temperature. Fixation did not affect pMHC loading or T cell response. After fixation, the yAPC were washed 3 times with 0.5% BSA and then loaded with excess pMHC in 100 μL 0.5% BSA at 4°C overnight. The yAPC were washed

3X with 0.5% BSA, stained with Alexa Fluor 647-conjugated anti-His (clone AD1.1.10, BioRad Antibodies) for 1 h at room temperature, and resuspended in 1 mL 0.5% BSA for FACS. The fluorophore to protein ratio (F/P) of the anti-His antibody was 3.1 and was provided by the manufacturer. Sorting was performed using a MoFlo Astrios (Beckman Coulter Life Sciences, Indianapolis, IN) cell sorter. Briefly, three or four gates were drawn based on distinct pMHC surface densities (as determined by the anti-His staining) and yAPC1 – yAPC5 cells were sorted using these gates. The median fluorescence intensity was converted into median pMHC per cell using Quantum™ Alexa Fluor® 647 Fluorescence Quantitation Beads (Bangs Laboratories, Fishers, IN). The uniformity of the sorted yAPC populations was confirmed by analyzing a fraction of the sorted yAPC using flow cytometry. For activation experiments requiring lower pMHC surface density than possible through standard induction, yAPC were pretreated with 0.1 mM – 0.5 mM TCEP for 10 minutes at room temperature. This mild TCEP treatment decreased the number of surface displayed scaffolds by reducing a fraction of the Aga1-Aga2 disulfide bonds anchoring each scaffold to the yeast cell surface. Cells were washed thoroughly with 0.5% BSA following TCEP treatment and then treated as described previously.

FACS involving pMHC-ICAM-1 co-assembly was performed by first fixing yAPC1, yAPC3, and yAPC5 with 0.1% PFA for 10 minutes at room temperature. Following fixation, each yAPC was loaded with 85% ICAM-1 and 15% pMHC in 100 μL 0.5% BSA at 4°C overnight. The display ratio of 85% ICAM-1 and 15% pMHC was confirmed by staining a small fraction of each yAPC for ICAM-1 (clone YN1/1.7.4 BioLegend) and analyzing the samples using flow cytometry. ICAM-1 and pMHC loaded yAPC1, yAPC3, and yAPC5 were then washed and stained for both ICAM-1 and pMHC with Alexa Fluor 647-conjugated anti-His

(clone AD1.1.10, BioRad Antibodies) and sorted and characterized in the same way as yAPC presenting pMHC alone.

3.6.5. T Cell Activation

T cell activation assays were performed in 96 well tissue culture plates at 37°C and 5% CO_2. Activation plates were blocked prior to activation with 1% BSA overnight at 4°C to minimize non-specific immobilization of pMHC during activation. Murine HA1.7 T cell hybridoma[314] were cultured to a density of 2.0 M/mL in IMDM (Invitrogen) supplemented with 10% fetal bovine serum for activation. Once at this density, 200,000 HA1.7 T cells were applied to the activation wells in 200 μL IMDM. In experiments involving sorted yAPC, 100,000 yAPC were used for activation. In experiments involving immobilization of pMHC for activation, pMHC was immobilized overnight at 4°C in 1% BSA. In experiments involving sAPC-pMHC complexes for activation, the sAPC-pMHC were assembled 2 h prior to activation in 1% BSA in volume of approximately 7 μL and added to 200 μL IMDM for activation. The activation supernatant was collected after 18 ± 2 h and analyzed using Ready-Set-Go IL-2 ELISA (eBiosciences, San Diego, CA) according to the manufacturer's protocol. The ELISA plate was developed for 10 minutes and the IL-2 secretion was measured by recording the absorbance at 650 nm (A650). To ensure consistency between experiments, a T cell activation index was calculated by dividing the A650 from activation wells by the A650 of the unstimulated controls. Thus, activation index indicates the multiple of IL-2 secretion over unstimulated T cells.

3.6.6. Regression Equations for T Cell Activation

T cell activation index was plotted against the average scaffold spacing for each yAPC construct. For each yAPC data set, activation index and scaffold spacing were logarithmically

transformed and fitted using linear regression with a fixed slope of -2. The regression equations thus provided a valency-dependent constant for each yAPC curve. T cell activation thresholds were then calculated by solving for a scaffold spacing that corresponded to a T cell activation index of 1.0 for each yAPC. The scaffold spacing thresholds were then used to calculate the corresponding pMHC surface density to determine the global pMHC density thresholds for each yAPC. For pMHC-ICAM-1 co-assembly experiments, the regression equation for T cell activation vs. pMHC surface density was determined by logarithmically transforming the values for pMHC surface density and performing linear regression on the transformed dataset. The minimum pMHC surface density requirement for measurable T cell IL-2 secretion was found by finding the pMHC surface density that corresponded to a T cell activation index of 1.0.

3.6.7. Statistical Analysis

Statistical analysis was performed using the Student's *t* test. All error bars are representative of the mean ± standard deviation of triplicate experiments unless otherwise noted. *$*P < 0.05$, $**P < 0.01$, $***P < 0.001$.*

Chapter 4. Advancing the Artificial Antigen Presentation Design Space: Characterizing 2D Multi-Scaffold Complex Assembly

4.1 Publication Information.

***Smith, M. R.**, *****Gao, H., Yee, C. M., Bugada, L. F., Ponnandy, P., Roth, C., Mutukuri, D., Lee, L., Ziff, R. M., Lee, J., Wen, F. Elucidating structure-performance relationships in whole-cell cooperative enzyme catalysis: role of multi-enzyme assembly efficiency, enzyme density and enzyme proximity in cellulose hydrolysis. 2018. (*In revision.*)

The goal of this chapter is to explore how multi-scaffold complexes assemble on the yeast cell surface, and explore the implications of assembly efficiency on artificial antigen presentation. While this work will be published in the context of biocatalysis, the quantitative approach to characterizing yeast-surface displayed supramolecular assemblies is directly applicable to engineering highly organized assemblies of T cell ligands for artificial antigen presentation. Mason Smith and Hui Gao contributed equally as first authors on this manuscript. Hui Gao and Cori Roth designed the proteins used in this study while Luke Bugada, Deepika Mutukuri and Lester Lee assisted in their expression and purification. Christine Yee and Prabhu Ponnandy performed the enzyme activity assays and fermentation experiments, respectively. Professor Robert Ziff assisted in developing a statistical model for aScaf surface distribution.

4.2. Abstract

Multi-protein complexes inspired by nature have received attention in a number of fields including whole-cell biocatalysis, artificial antigen presentation, and biosensor engineering. Despite considerable interest, efforts to harness the full potential of multi-protein assemblies have been based on trial and error rather than rational design due to the lack of quantitative tools. This empirical approach has created a gap in our understanding of how these supramolecular complexes assemble, and what parameters affect assembly efficiency. Here, we developed quantitative experimental tools that enabled the first quantitative investigation of multi-scaffold assemblies on the yeast cell surface. Combined with a statistical model, we revealed that multi-scaffold assembly efficiency is limited by molecular crowding on the yeast cell surface, and this crowding effect is more prominent for larger scaffold constructs. This work raises interesting questions regarding the optimum design of supramolecular assemblies, including a tradeoff between multi-scaffold assembly efficiency and the expression level of surface displayed scaffolds.

4.3. Introduction

In **Chapter 3**, we showed that the spatial and stoichiometric organization of T cell ligands on a yeast cell surface could be finely controlled by protein-scaffold directed assembly using cohesin-dockerin binding. However, the assemblies we have described thus far are relatively simple and do not closely resemble the immunological synapse. One strategy for increasing the complexity of protein assemblies – and potentially mimicking the structure of the immunological synapse – is to create 2D multi-scaffold complexes using surface displayed anchor scaffolds (aScafs) and addressable primary scaffolds (pScafs) **(Figure 4.1)**.[315–317] These

complex multi-scaffold assemblies are formed by fusing a dockerin to either the N- or C-terminus of the pScaf protein. The pScaf-dockerin fusion protein can then assemble with surface displayed aScafs via *in vitro* loading to create 2D multi-scaffold complexes capable of binding dockerin-fused ligands. Because cohesin-dockerin binding is largely species-specific, the molecular organization of ligands assembled on 2D aScaf-pScaf complexes can be further controlled by engineering chimeric pScafs and aScafs composed of cohesin modules with different binding specificities (**Figure 4.1**).[293,299,318,319] More than 19 distinct cellulosomal species (i.e. microbes that utilize cohesin-dockerin binding) have been identified to date,[320] providing diverse library of orthogonal cohesin-dockerin binding pairs that can be used to construct a myriad of molecular architectures.

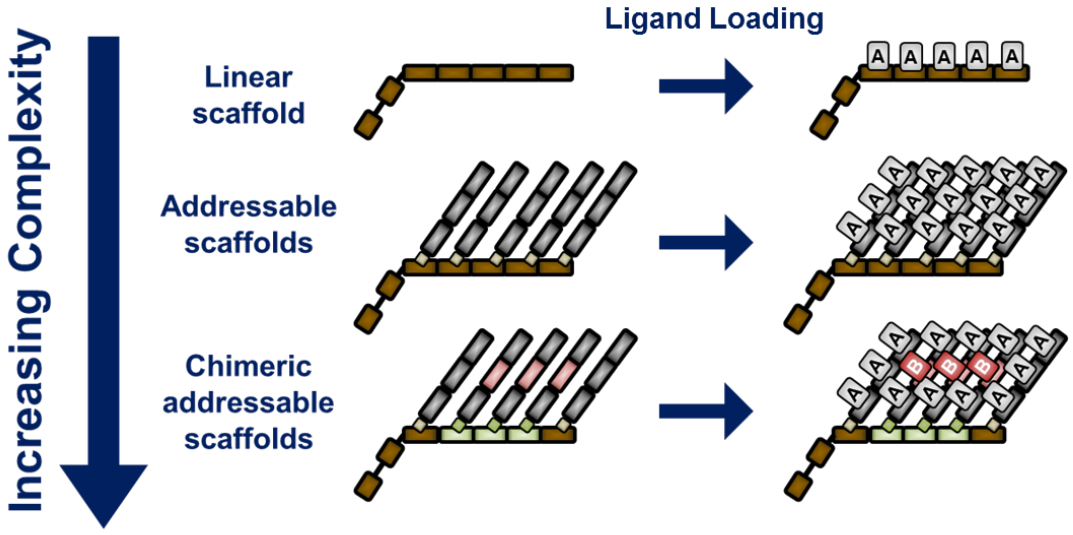

Figure 4.1. 2D multi-scaffold complex architectures.

While we have discussed cohesin-dockerin binding in the context of artificial antigen presentation, this interaction has traditionally been used to organize cooperative enzyme assemblies for the efficient hydrolysis of lignocellulosic biomass.[320–322] Lignocellulosic biomass

is among the most abundant renewable carbon sources on Earth and represents a sustainable feedstock for the production of materials, value-added chemicals, and biofuels.[323–331] The primary component of lignocellulosic biomass is cellulose, a polysaccharide that locks β-1,4-linked glucosyl units in a highly compact crystalline structure.[332] Completely hydrolyzing cellulose to glucose requires three types of enzymes: endoglucanases, exoglucanases (or cellobiohydrolases), and β-glucosidases,[332–334] which exhibit enzyme-enzyme synergy through their cooperative activities.[335–337] When these enzymes are organized on surface displayed scaffolds they also exhibit proximity synergy, which further enhances the overall activity.[319,338]

Realizing the full potential of surface-displayed multi-scaffold complexes – in both biocatalysis and artificial antigen presentation – will require a more complete understanding of how these proteins assemble, and how the assembly architecture relates to its function. For example, the extent to which pScafs and ligands saturate their respective binding sites on surface-displayed multi-scaffold assemblies is rarely reported in the literature due to a lack of quantitative tools. This is especially important in biocatalysis, where a lack of quantitative characterization complicates the comparison of biocatalyst designs, as one design may have considerably higher assembly efficiency or enzyme density than another. In the context of artificial antigen presentation, full spatial and stoichiometric characterization of the T cell ligand assembly is crucial to reproducing optimum presentation patterns. Further, because quantitative tools and protocols are rarely utilized for characterizing surface-displayed protein assemblies, it is often difficult to decouple the contribution of different structural parameters to the output. For example, without the quantitative characterization of the yAPCs described in **Chapter 3**, it would be difficult to determine the individual contribution of T cell ligand valency and overall T cell ligand surface density on T cell activation. Likewise, reliably evaluating the role of structural

parameters like aScaf expression level, overall enzyme density per cell, and the size of multi-scaffold enzyme assemblies on overall biocatalyst activity is not possible without quantitative tools.

Here we engineered yeast to present 2D multi-scaffold complexes using aScafs binding one (aScaf1), two (aScaf2), and three (aScaf3) pScafs, with each pScaf designed to bind four unique ligands. With these constructs, we developed a quantitative approach to characterize the assembly of each yeast-surface displayed 2D multi-scaffold assembly. This quantitative approach revealed that aScaf-pScaf assembly is limited by the molecular crowding of aScafs on the yeast cell surface. To better understand this result, we developed a statistical model of aScaf spatial organization based on a Poisson distribution. Using this model, we found that neighboring aScafs must be separated by some critical distance – which is dependent on aScaf size – for aScaf-pScaf binding to occur. We then used the critical distance values provided by the model to predict aScaf-pScaf assembly efficiency as a function of aScaf expression level. The statistical model agreed well with the experiment results, with both indicating that large aScaf designs are more sensitive to surface crowding during aScaf-pScaf assembly than small aScaf designs. Further, our model predicts that the total ligand surface density is maximized when aScaf-surface crowding allows only $1/e$ (~37%) of expressed aScaf to bind pScaf. Taken together, these observations suggest that aScaf-pScaf assembly is performed in an "outside-in" manner, in which the most distal aScaf cohesin sites are occupied first and, once occupied, limit pScaf access to the internal cohesin sites. While this work will be published in the context of whole-cell biocatalysis, the mechanism of surface-crowding limited assembly described here has important implications for the design of complex surface displayed assemblies in a variety of fields including artificial antigen presentation.

4.4. Results and Discussion

4.4.1. Design of 2D Multi-scaffold Complex

Yeast cells were engineered to express anchor scaffold proteins (aScafs) as C-terminal fusions with the a-agglutinin subunit Aga2 for Aga1-Aga2 yeast-surface display (**Figure 4.2a**).[299,339,340] Three different aScafs were engineered composed of one (aScaf1), two (aScaf2), or three (aScaf3) type II cohesins derived from *C. thermocellum*[341] to accommodate a corresponding number of primary scaffold proteins (pScafs). The surface-displayed aScafs were also fused to a C-terminal V5 epitope tag for detection and quantification.

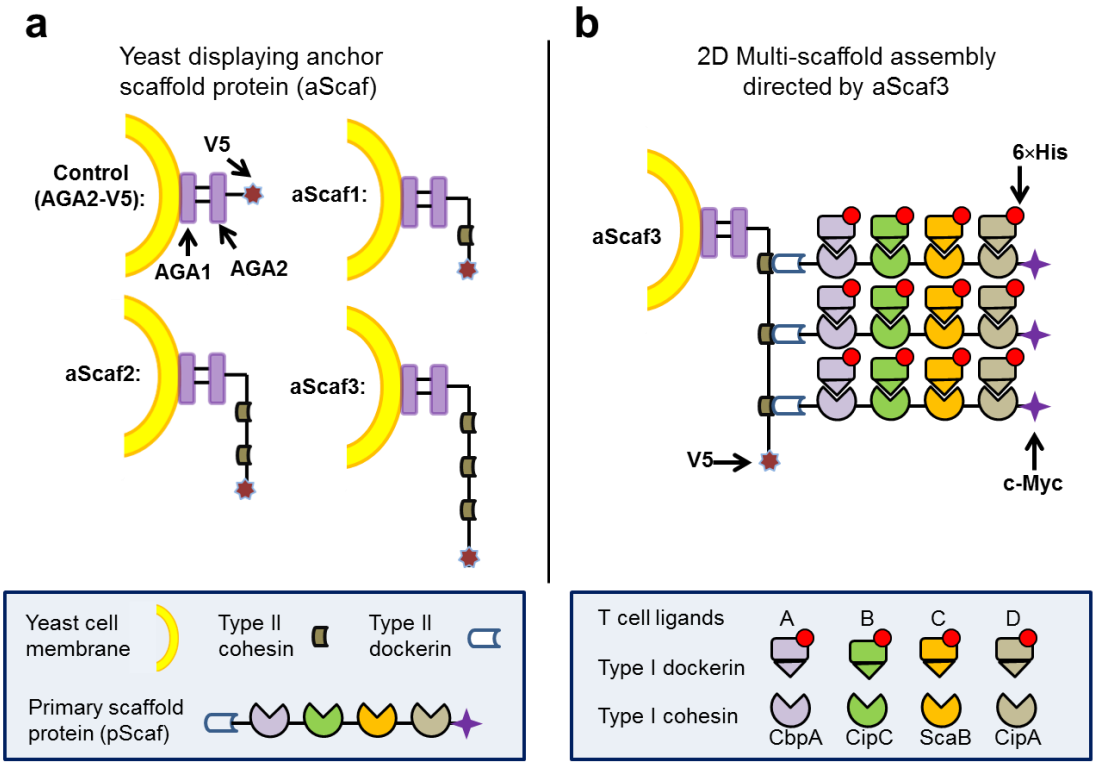

Figure 4.2. Schematic of surface-displayed 2D multi-scaffold assembly.
(a) Yeast were designed to display anchor scaffold proteins (aScafs) accommodating one (aScaf1), two (aScaf2), or three (aScaf3) addressable scaffold proteins (pScafs) through type II cohesin-dockerin binding. (b) Representation of aScaf3 2D multi-scaffold assembly. Chimeric T cell ligands can be assembled on the pScaf through species-specific type I cohesin-dockerin interactions, as indicated by color-coding.

The pScaf was designed to function as an addressable scaffold protein, binding the surface-displayed aScafs and four unique ligands through its type II dockerin and four type I cohesins, respectively (**Figure 4.2b**). Each of the four type I cohesins was derived from a scaffoldin protein of a different cellulolytic microbe: CipA of *C. thermocellum*, ScaB of *R. flavefaciens*, CipC of *C. cellulolyticum*, and CbpA of *C. cellulovorans* (**Table 4.1**). The pScaf protein was also fused to a c-Myc epitope tag for detection and quantification.

Table 4.1. Description of recombinant proteins used in this study.

Protein	Description	Accession number[a]	Expression vector	Tag
aScaf	Scaffold protein containing one, two, or three type II cohesins from scaffoldin OlpB displayed on *S. cerevisiae* surface	WP_020458018	pYD1	c-Myc
pScaf	Scaffold protein containing four of type I cohesins, one CBM, and a type II dockerin from different organisms	CipA:WP_020458017; ScaB: Q9AE52; CbpA: AAA23218; CipC: AAC28899; CBM:WP_020458017; Type II dockerin: WP_020458017	pET28a	V5

[a] The accession numbers appear in the DDBJ/EMBL/GenBank nucleotide sequence databases.

4.4.2. Quantitative Characterization of aScaf-pScaf Assembly

The successful assembly of the 2D multi-scaffold complexes is predicated on robust aScaf surface expression, which we evaluated using confocal microscopy. To detect aScaf surface expression, yeast cells expressing aScaf1, aScaf2 or aScaf3 were stained with fluorescently labeled anti-V5 antibody. As shown in **Figure 4.3a**, aScaf expression was detected for all three constructs and appeared uniform across the entire cell surface. Further, yeast displaying aScaf1 appeared to show the highest aScaf expression level while aScaf3 appeared to

show the lowest, suggesting that aScaf expression level on the yeast cell surface is a function of protein size.

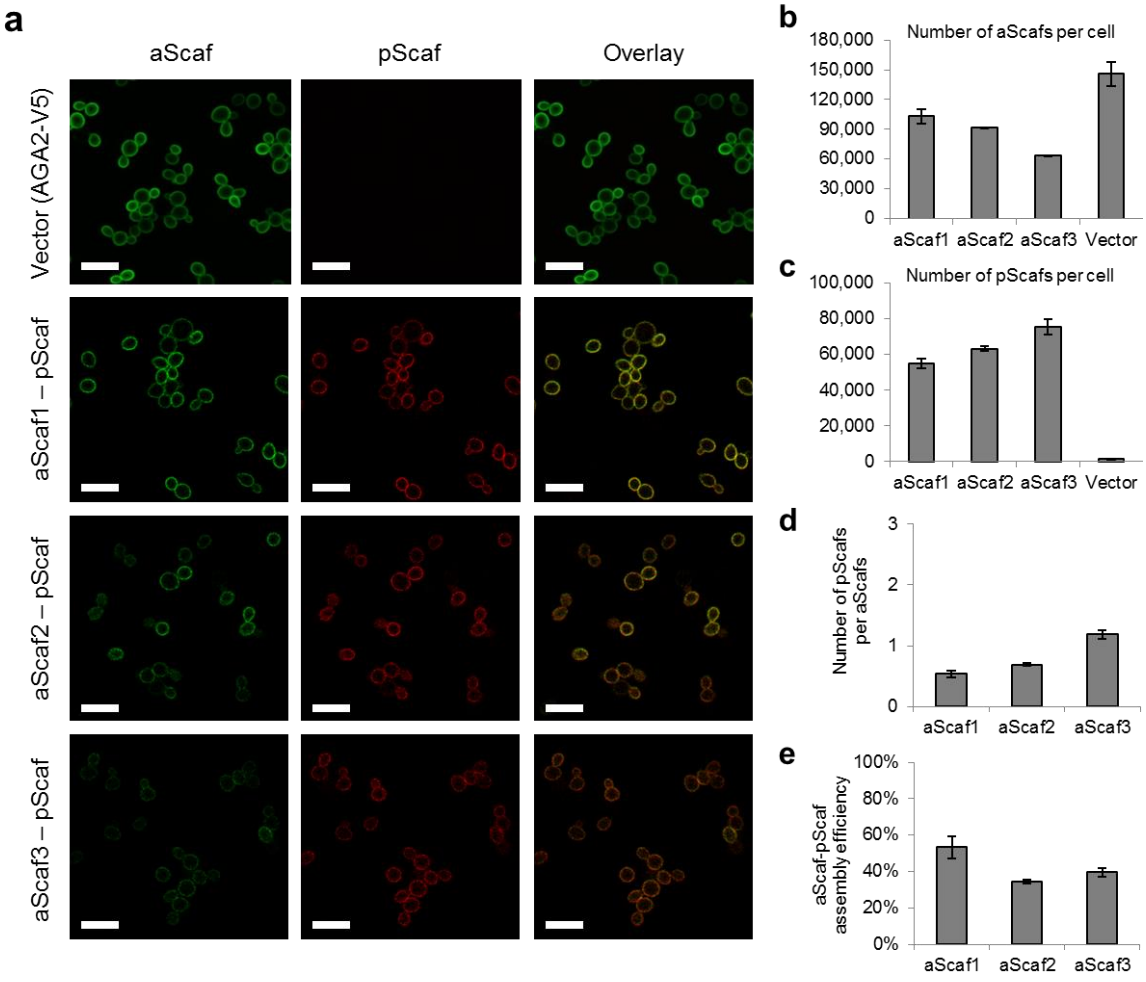

Figure 4.3. Confocal microscopy and quantitative flow cytometric analysis of aScaf-pScaf assembly on the yeast cell surface.

(a) Confocal microscope images of four yeast constructs stained for aScaf (green, anti-V5-AF647) and pScaf (red, anti-c-Myc-AF488). Vector control (AGA2-V5) included a V5 epitope tag but no type II cohesins. (b) Quantification of the number of aScaf on the surface of each yeast construct. (c) Quantification of the number of pScaf assembled on each of the four yeast constructs. (d) The average number of pScaf assembled by aScaf1, aScaf2, and aScaf3. (e) The aScaf-pScaf assembly efficiency for aScaf1-pScaf, aScaf2-pScaf and aScaf3-pScaf. Data are represented as the mean of at least two independent experiments and error bars signify standard deviation.

After confirming aScaf surface display, the average number of aScaf per cell was quantified using flow cytometry. Quantitative flow cytometry has been routinely used to quantify the surface density of mammalian proteins by staining the target protein with fluorescently labeled monoclonal antibodies and comparing the median fluorescence intensity (MFI) to that of standard beads with known numbers of molecules of equivalent soluble fluorophore (MESF).[342,343]

Using the same principle, we stained the V5 epitope tag of each aScaf design, and the aScaf expression level was then quantified by comparing its MFI to that of standard beads. In agreement with confocal microscopy observations, aScaf expression level was found to depend strongly on the aScaf size, ranging from ~103,000 for aScaf1 to ~63,000 for aScaf3 (**Figure 4.3b**). Further, the Aga2-V5 fusion protein, which was the smallest protein displayed on a yeast cell surface in this study, had an expression level of ~143,000. Taken together, these results further suggest that aScaf surface display is limited by either protein transport or increased metabolic burden associated with aScaf size.

To mitigate complications in protein transport and/or ease yeast metabolic burden, we expressed and purified the pScaf from *E. coli* rather than co-expressing it in yeast. *In vitro* loading of purified pScaf under saturating conditions ensured that multi-scaffold assembly was not influenced by protein transport or expression limitations. The purity and size of pScaf protein was verified using SDS-PAGE (**Figure 4.4**) prior to loading onto yeast cells displaying the aScafs. The aScaf-pScaf assembly was then evaluated by co-staining the cells with fluorescently labeled anti-V5 and anti-c-Myc antibodies (binding the aScaf and pScaf, respectively).

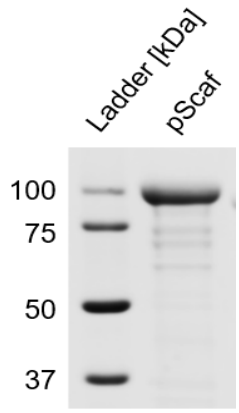

Figure 4.4. SDS-PAGE analysis of pScaf purified from *E. coli*.

Confocal microscopy showed that the pScaf was detected on all three aScaf constructs, but not on the control expressing the Aga2-V5 fusion, indicating that aScaf-pScaf assembly is specific and aScaf-dependent (**Figure 4.3a**). Quantitative flow cytometry further revealed that the number of pScafs per cell increased modestly as the aScaf size increased from ~54,000 per cell on aScaf1 to ~75,000 per cell on aScaf3 (**Figure 4.3c**). The number of pScafs per aScaf also increased as the number of pScaf binding sites (i.e. type II cohesins) on the aScaf increased, corresponding to: 0.53, 0.69 and 1.19 for aScaf1, aScaf2 and aScaf3, respectively (**Figure 4.3d**). Using this data, the aScaf-pScaf assembly efficiency was calculated by normalizing the number of pScaf per aScaf with respect to the theoretical maximum (i.e. one pScaf per aScaf1, two pScafs per aScaf2, and three pScafs per aScaf3). Interestingly, the aScaf-pScaf assembly efficiency observed for each of the three constructs was relatively low, ranging from a minimum of 34% for aScaf2 to 53% for aScaf1 (**Figure 4.3e**). Given that loading was performed with a saturating amount of pScaf protein, we hypothesized that aScaf-pScaf assembly might be limited by aScaf crowding on the yeast cell surface.

4.4.3. Modeling 2D Multi-scaffold Complex Assembly

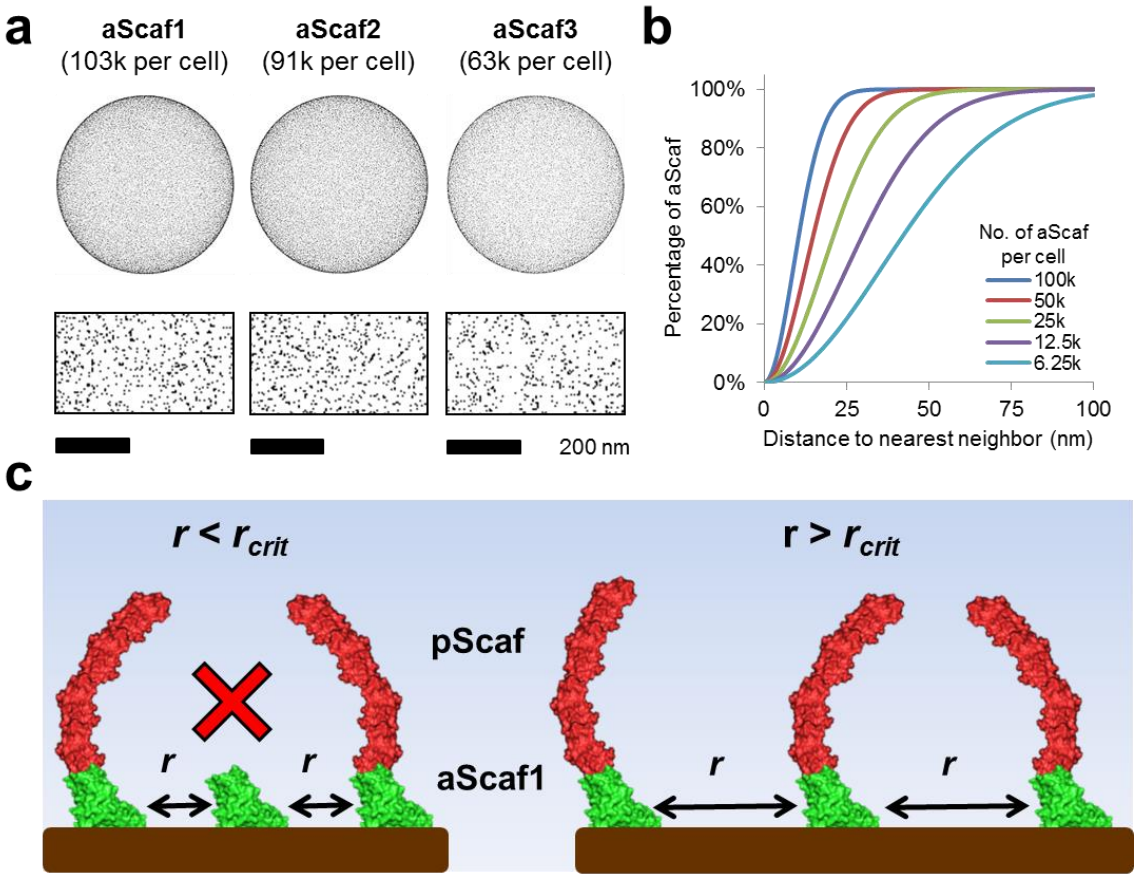

Figure 4.5. Statistical model of aScaf spatial distribution on yeast cell surface.
a) Visual representation of aScaf distribution across the yeast cell surface for aScaf1, aScaf2, and aScaf3. (b) Poisson distribution representing the spatial arrangement of aScaf as the distance to nearest neighbor. Each line represents this distribution for a different aScaf expression level (6.25k – 100k per cell). (c) Visual representation of crowding-limited assembly hypothesis. When the distance between neighboring aScafs is less than the critical distance (r_{crit}), aScaf-pScaf assembly does not occur (left). When the distance between neighboring aScafs is greater than r_{crit}, aScaf-pScaf assembly occurs (right).

To further explore our hypothesis that aScaf-pScaf assembly efficiency is limited by aScaf crowding on the yeast cell surface, we modeled the spatial arrangement of each aScaf on the cell surface using the Poisson distribution (Equation 4.1 and **Figure 4.5a**). Integrating this distribution allowed the percentage of total aScaf to be plotted with respect to its distance to nearest neighbor (Equation 4.2). When the aScaf expression level is high (e.g., 100k per cell), the

distribution of aScaf distance to nearest neighbor is tight, and the average distance between aScafs is relatively short. In contrast, when the aScaf expression level is low (e.g., 6.25k per cell), the distribution of aScaf distance to nearest neighbor is broader, and the average distance between aScafs is farther (**Figure 4.5b**). Based on this distribution, if aScaf-pScaf assembly efficiency is determined solely by aScaf surface crowding, then there should be a minimum aScaf distance to nearest neighbor (critical distance) below which aScaf-pScaf binding does not occur (**Figure 4.5c**).

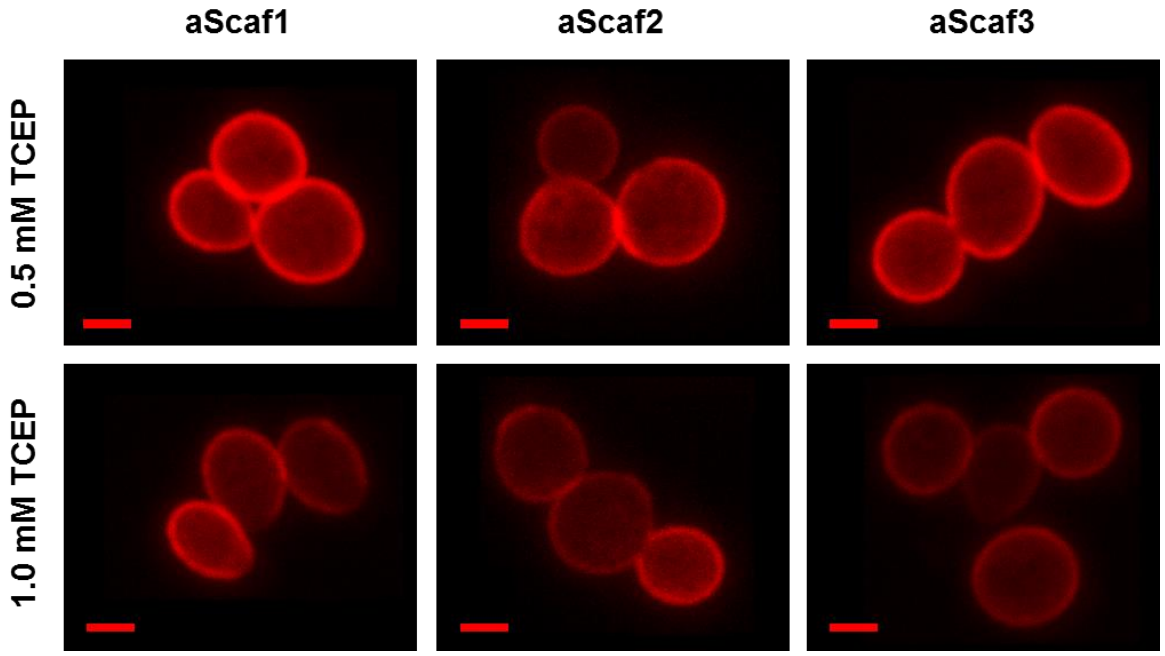

Figure 4.6. Confocal microscopy of yeast aScaf expression following TCEP treatment. Confocal microscope imaging of aScaf distribution following TCEP treatment. Scale bar represents 2 μm.

To test the crowding-limited assembly hypothesis, we needed to investigate aScaf-pScaf assembly over a range of aScaf expression levels. This was done by treating each of the aScaf constructs with various amounts of TCEP, which reduces a fraction of the disulfide bonds

anchoring the surface-displayed aScafs. TCEP treated aScafs were qualitatively analyzed by confocal microscopy to confirm that aScaf surface distribution appeared random (**Figure 4.6**).

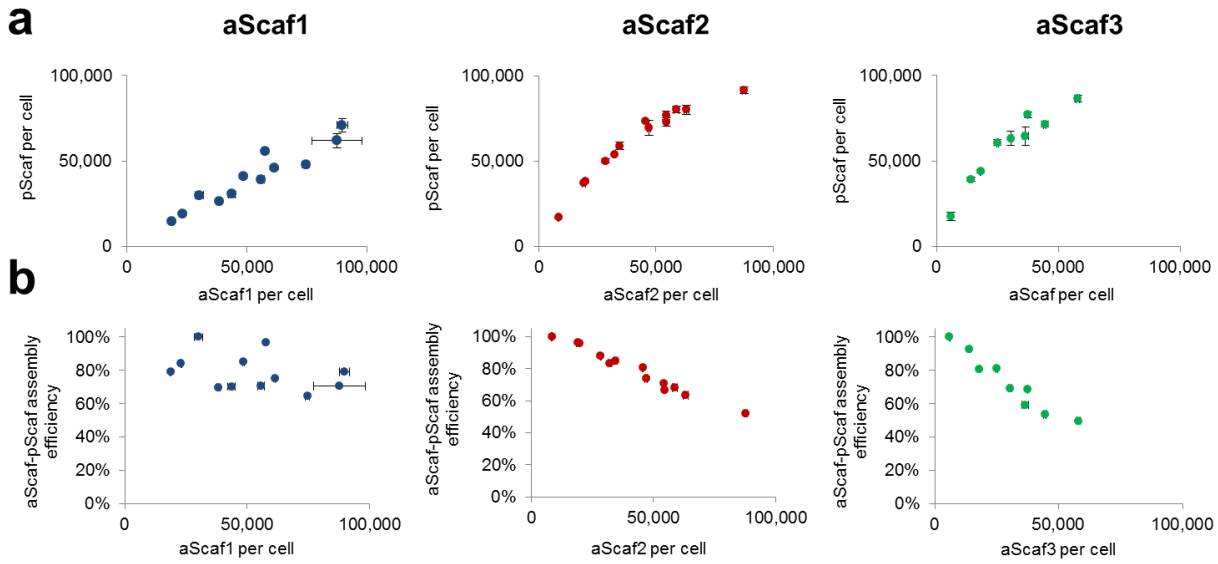

Figure 4.7. aScaf-pScaf assembly characterized for various aScaf expression levels.
(a) Number of assembled pScaf per cell plotted with respect to aScaf1, aScaf2, and aScaf3 expression level. (b) aScaf-pScaf assembly efficiency plotted with respect to aScaf expression level for aScaf1, aScaf2, and aScaf3. aScaf-pScaf assembly efficiency was normalized based on a maximum assembly efficiency of 100%. Data are plotted as the mean from at least two independent experiments. Error bars signify standard deviation.

Following confocal microscopy, each TCEP treated aScaf was loaded with pScaf and aScaf-pScaf assembly was characterized using quantitative flow cytometry (**Figure 4.7a**). Because of the sensitivity limitation of quantitative flow cytometry, aScaf-pScaf assembly efficiency was normalized to 100% for the highest aScaf-pScaf assembly observed for each aScaf construct. This normalization only modestly increased the observed aScaf-pScaf assembly efficiencies, and was used for the subsequent analyses. While the aScaf1-pScaf assembly efficiency was weakly dependent on aScaf1 expression level, the aScaf2-pScaf and aScaf3-pScaf assembly efficiencies exhibited a strong inverse correlation with aScaf expression level (**Figure 4.7b**). This result is consistent with our hypothesis that aScaf-pScaf assembly is limited by

crowding effects, as aScaf assembly was more efficient when there were fewer aScaf proteins present on the surface. Moreover, the shape of the aScaf-pScaf assembly efficiency curves in **Figure 4.7b** revealed that the aScaf3-pScaf assembly efficiency is the most sensitive to aScaf expression level, indicating that aScaf surface crowding is more prominent for larger aScaf constructs. This observation suggests that aScaf-pScaf assembly occurs in an "outside-in" manner (**Figure 4.8a**).

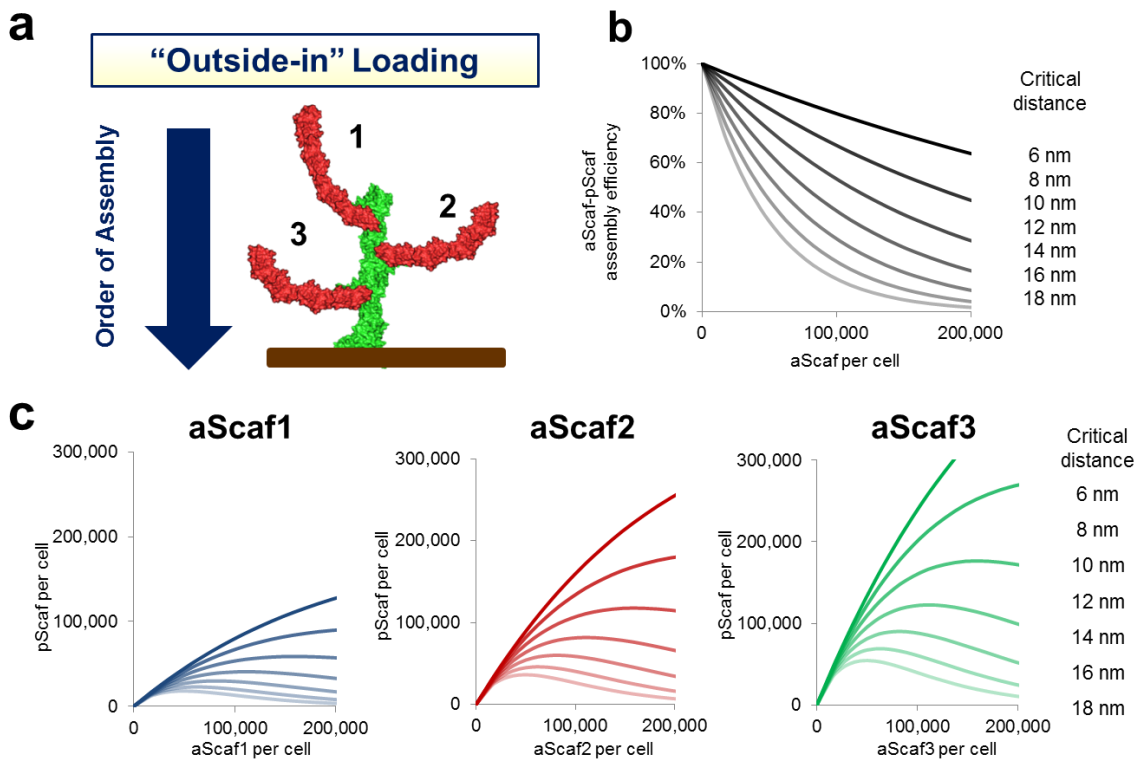

Figure 4.8. Statistical model of aScaf-pScaf assembly based on aScaf surface crowding. (a) Visual representation of "outside-in" aScaf-pScaf assembly mechanism. (b) Theoretical aScaf-pScaf assembly efficiency plotted as a function of aScaf expression level for various critical distances. (c) Theoretical number of pScaf assembled on aScaf1, aScaf2, and aScaf3, plotted with respect to aScaf expression level and for various critical distances (top curve – 6 nm; bottom curve – 18 nm).

After experimentally characterizing the aScaf-pScaf assembly efficiency with respect to aScaf expression level, we aimed to elucidate the critical distance required for aScaf-pScaf

binding of each aScaf design. Using the Poisson distribution (Equation 4.2), we plotted the theoretical aScaf-pScaf assembly efficiency as a function of aScaf expression level for different critical distances (**Figure 4.8b**). These curves indicate that if the critical distance for a particular aScaf design is small (i.e. 6 nm), aScaf-pScaf assembly efficiency is weakly dependent on aScaf expression level. In contrast, if the critical distance for a particular aScaf design is large (e.g. 18 nm), the aScaf-pScaf assembly efficiency is strongly dependent on aScaf expression level. In statistical terms, the concavity of the aScaf-pScaf assembly efficiency curve is representative of the aScaf critical distance. aScafs characterized by large critical distance will have more concave assembly curves, indicating pronounced sensitivity to crowding effects.

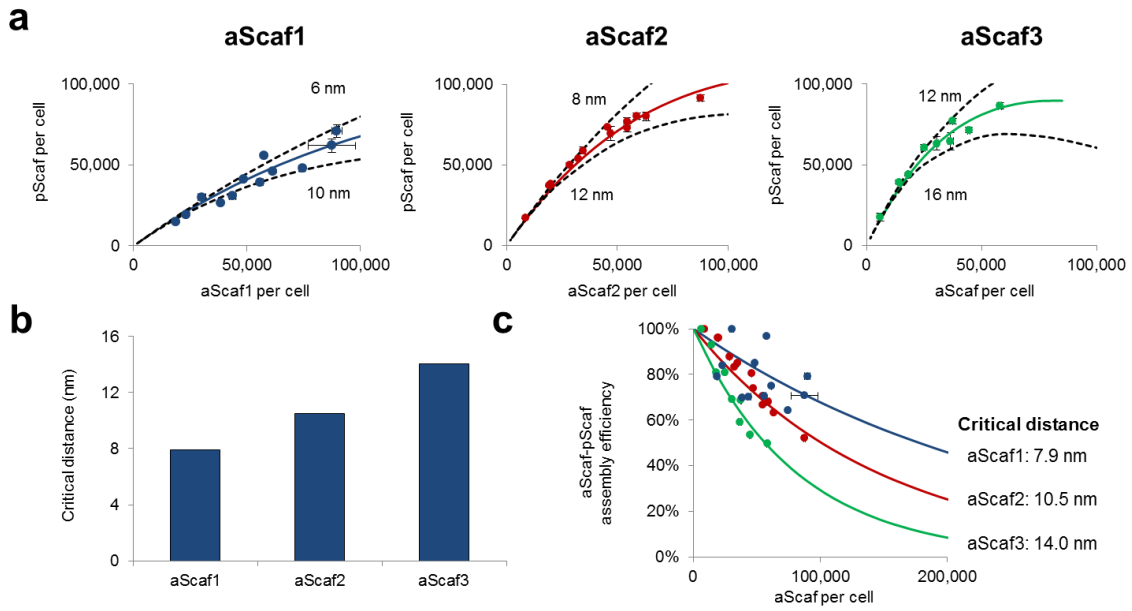

Figure 4.9. Determining critical distance for aScaf-pScaf assembly.
(a) Number of pScaf per cell for aScaf1, aScaf2, and aScaf3, plotted with respect to aScaf expression level. Solid lines represent best-fit curves generated by solving for the most representative critical distance for each aScaf dataset. Dashed lines represent theoretical curves for other critical distance values. (b) Critical distance required for aScaf-pScaf assembly for aScaf1, aScaf2, and aScaf3. (c) aScaf-pScaf assembly efficiency plotted with respect to aScaf expression level for aScaf1, aScaf2, and aScaf3. Solid lines represent best-fit curves in (a). Data are represented as the mean of at least two independent experiments. Error bars signify standard deviation.

Using the assembly efficiency curves in **Figure 4.8b**, the theoretical number of pScafs assembled on each aScaf construct was determined as a function of aScaf expression level for various critical distances (**Figure 4.8c**). Interestingly, these curves suggest that if aScaf-pScaf assembly is limited by aScaf surface crowding, increasing aScaf expression level beyond a point will actually result in a net reduction in the number of pScaf per cell.

The critical distance for each aScaf construct was determined by fitting the integrated Poisson distribution (Equation 4.2) to the aScaf-pScaf assembly data in **Figure 4.7a** by varying the critical distance in a least-squares regression (**Figure 4.9a**). As expected, this curve fitting revealed that the critical distance was dependent on aScaf size, ranging from 7.9 nm for aScaf1 to 14.0 nm for aScaf3 (**Figure 4.9b**). After determining the critical distance for each aScaf design, the corresponding aScaf-pScaf assembly efficiency curve was plotted as a function of aScaf expression level (**Figure 4.9c**). The theoretical aScaf-pScaf assembly efficiency curves fit the experimental data well, especially for aScaf2 and aScaf3. Consistent with our previous observations, these curves indicate that the largest aScaf design (namely, aScaf3) is the most sensitive to crowding effects while the smallest aScaf design was the most robust to aScaf surface crowding.

Using these aScaf-pScaf assembly efficiency curves and assuming a constant 70% pScaf-ligand assembly efficiency for each design, the predicted number of ligands assembled per cell was plotted as a function of aScaf expression level (**Figure 4.10a**). Based on crowding limited aScaf-pScaf assembly, the maximum possible ligand display level on aScaf1 is ~259,000, which is achieved at an aScaf expression level of ~257,000 (**Figure 4.10a**). The maximum possible ligand display level for aScaf2 is ~300,000, which is achieved at an aScaf expression level of ~146,000. Interestingly, under crowding-limited aScaf-pScaf assembly, aScaf3 is only predicted

to display a maximum of ~252,000 ligands per cell at an aScaf expression level of ~81,000, which is lower than both aScaf1 and aScaf2. While unexpected, this result has significant implications for the design and application of surface-displayed 2D multi-scaffold assemblies. For example, applications that seek to achieve the maximum ligand loading using 2D multi-scaffold assemblies should be wary of engineering large aScaf proteins, as the critical distance associated with these constructs will require a greater amount of cell surface area for efficient loading.

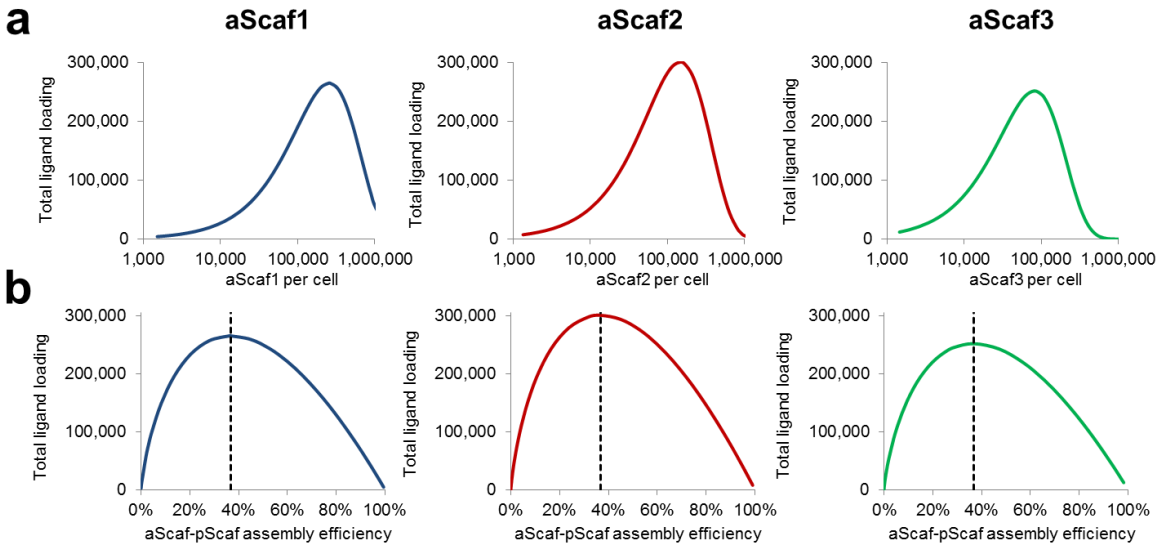

Figure 4.10. Total ligand loading predicted based on surface-crowding limited 2D multi-scaffold complex assembly.
(a) Total ligand loading based on surface-crowding limited aScaf-pScaf assembly plotted with respect to aScaf expression level for aScaf1, aScaf2, and aScaf3. (b) Total ligand loading plotted with respect to crowding-limited aScaf-pScaf assembly efficiency. Dashed line represents maximum possible ligand display level, which occurs at 37% aScaf-pScaf assembly efficiency for all constructs. For all graphs, best-fit critical distance values of 7.9 nm, 10.5 nm, and 14.0 nm were used for aScaf1, aScaf2, and aScaf3, respectively.

Another interesting implication of crowding-limited aScaf-pScaf assembly is that the total ligand display level is maximized for each aScaf design at an aScaf expression level that corresponds with an aScaf-pScaf assembly efficiency of 1/*e* (or ~37%) (**Figure 4.10b**). These

results suggest that when the aScaf expression level is higher than this optimum, each additional aScaf protein crowds out previously accessible aScaf proteins, rendering them inaccessible to pScaf binding. This phenomenon results in a net reduction in the number of possible pScafs – and corresponding ligands – assembled per cell. In contrast, when aScaf expression level is below this optimum, the spatial distribution of aScaf across the yeast cell surface is suboptimal – that is, the total yeast cell surface area is not being used efficiently for pScaf binding. As a result, more aScafs can be added to the surface without crowding effects dominating, increasing the number of possible pScafs and ligands assembled per cell, but at the expense of multi-scaffold assembly efficiency. These results highlight the clear tradeoff that arises from aScaf crowding: increasing aScaf expression level (from 0 to optimum) causes an increase in total ligand density while reducing the assembly efficiency.

4.5. Conclusions and Outlook

2D multi-scaffold assemblies provide an elegant method for finely controlling the spatial and stoichiometric organization of ligands on a cell surface. While these assemblies have traditionally been studied in the context of whole-cell biocatalysis,[293,319] they have significant potential in artificial antigen presentation, as complex molecular architectures can be engineered to mimic the structure and composition of the immunological synapse. Despite their potential, the molecular principles that govern how 2D multi-scaffold complexes assemble, and the mechanisms by which the assembly architecture influences its overall function are not well understood due to a lack of quantitative tools. Here, we developed experimental and theoretical approaches to quantify each step of a multi-scaffold assembly process. This work presents the first quantitative study of cellulosomal structure assembly and revealed that aScaf-pScaf

assembly is limited by aScaf molecular crowding, which should provide guidance for design of future cell-surface displayed protein assemblies.

Using quantitative flow cytometry, we observed that aScaf-pScaf assembly efficiency is dependent on aScaf expression level. This result suggests that aScaf surface crowding limits aScaf-pScaf assembly efficiency, and therefore aScafs must be separated from their nearest neighbor by a minimum distance for pScaf binding to occur. The molecular basis of this crowding effect is likely related to the random distribution of aScafs across the yeast cell surface. If aScaf surface distribution is random, then some areas of the yeast cell surface will have more aScafs than other areas. As the aScaf expression level increases, some of these more populated areas will become so crowded that early pScaf binding events block a surrounded aScaf from accessing a pScaf in the bulk solution. We simulated this phenomenon by modeling aScaf expression on the yeast cell surface as a Poisson distribution and found that aScaf critical distance was dependent on aScaf size (aScaf1 – 7.9 nm, aScaf1 10.5 nm, aScaf3 14.0 nm) meaning larger aScafs are more sensitive to crowding-limited pScaf assembly.

The dependence of aScaf-size on surface crowding likely arises from an “outside-in” mechanism of aScaf-pScaf assembly. Under “outside-in” assembly, the most distal cohesin on aScafs are closest to the “bulk” solution, and thus likely to bind pScafs before cohesins closer to the cell surface. As more of the distal cohesins become occupied by pScafs, neighboring partial assemblies begin to obstruct the diffusion of soluble pScafs from the bulk solution to the interior cohesins, resulting in additional aScaf-pScaf assembly inefficiency. Therefore, at the same aScaf expression level, aScafs composed of more cohesins would have lower aScaf-pScaf assembly efficiency than aScafs composed of fewer cohesins.

Interestingly, inefficient aScaf-pScaf assembly caused by surface crowding is not necessarily an impediment to achieving a high cellular ligand density. Instead, our model predicts that total ligand density is maximized when surface crowding allows only 37% of expressed aScaf to bind pScaf (i.e. 37% aScaf-pScaf assembly efficiency). At first, this result may seem counterintuitive as one might assume that high assembly efficiency correlates with higher ligand density. However, because aScaf crowding limits aScaf-pScaf assembly efficiency, high assembly efficiencies are only possible at relatively low aScaf expression levels. While increasing aScaf expression level reduces aScaf-pScaf assembly efficiency, the additional aScafs (up to ~257,000 aScaf1 per cell, ~145,000 aScaf2 per cell, and ~81,000 aScaf3 per cell) provide more pScaf binding sites – and thus ligand binding sites – than are lost by inefficient assembly (**Figure 4.10b**).

Achieving the aScaf expression level necessary for maximum ligand display presents other challenges given the considerable metabolic burden such expression levels impose. Although we were able to achieve a maximum expression level of ~103,000 for the smallest aScaf used in this study (aScaf1), this is was only possible by expressing the pScaf separately and assembling the 2D multi-scaffold complexes *in vitro*. If all the components of the assembly (aScaf, pScaf, and potentially each unique ligand) were expressed in a single cell, the maximum attainable aScaf expression level would like be significantly reduced, given the increased metabolic burden associated with expressing each protein. Nevertheless, the tradeoff between ligand density and aScaf-pScaf assembly efficiency observed in this study highlights an unanticipated consequence of molecular crowding during a stochastic protein assembly process.

While 2D multi-scaffold assemblies have significant potential in artificial antigen presentation, the size of these supramolecular complexes may introduce additional

complications. Multi-protein assemblies "built-up" from the cell surface are not generally found on natural or engineered APCs and the presence of these large assemblies will like affect the spatial distribution of proteins at the T cell interface. In **Chapter 1,** we introduced the kinetic-segregation theory of TCR triggering, which postulates that size-based exclusion of phosphatases from the T cell-APC interface drives ITAM phosphorylation (**Figure 4.11a**). A number of studies have demonstrated that restricting phosphatase exclusion from the engaged TCR – including by elongating TCR ligands – significantly reduces kinase activity, and thus inhibits T cell activation.[104–107] Therefore, it is possible that surface-displayed 2D multi-scaffold assemblies loaded with TCR ligands will increase the space between an antigen presenting surface and the T cell membrane, reducing size-driven segregation of CD45 from the cSMAC (**Figure 4.11b**).

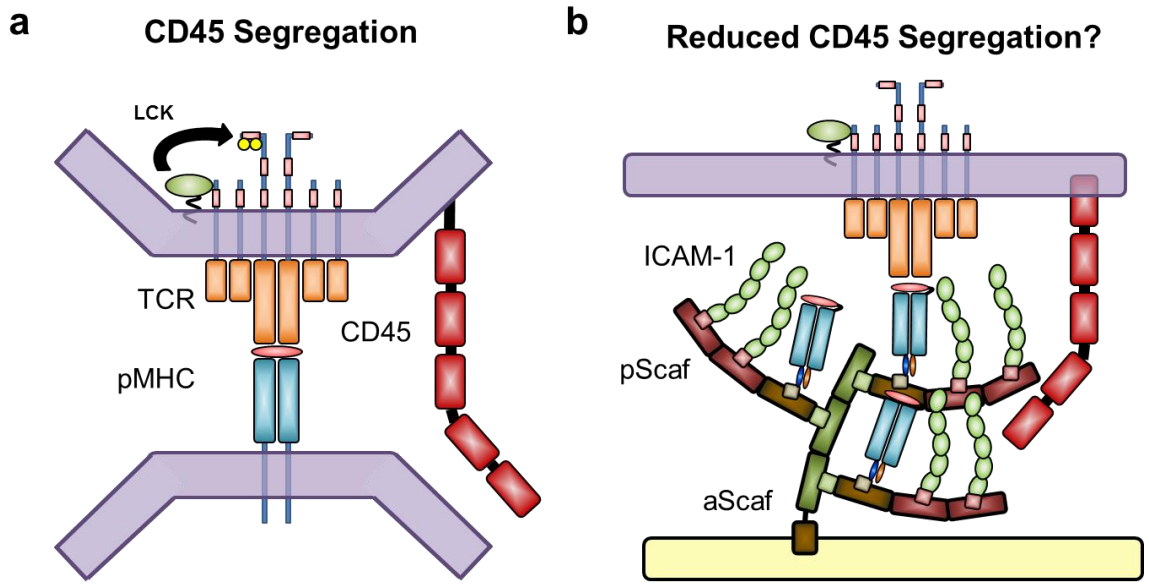

Figure 4.11. Effect of 2D multi-scaffold assemblies on size-based CD45 segregation.
(a) The kinetic-segregation theory of TCR triggering hypothesizes that ITAM phosphorylation is driven by the size-based segregation of bulky phosphatases (CD45) from the immediate proximity of an engaged TCR. The absence of phosphatases tilts the basal balance of kinase-phosphatase activity on the TCR ITAMS in favor of phosphorylation and TCR triggering occurs. (b) Large 2D multi-scaffold assemblies could increase the distance between the antigen presentation surface and the T cell membrane, which would reduce CD45 segregation and thus inhibit TCR triggering.

Going forward, we plan to apply the insights gained in this study to investigate how the structure of 2D multi-scaffold assemblies can be tuned to control T cell activation. While a series of studies will be necessary to determine what – if any – size assembly inhibits TCR triggering through reduced CD45 segregation, we believe that 2D multi-scaffold assemblies offer new opportunities in the artificial antigen presentation design space. In contrast to conventional patterning technologies associated with planar artificial antigen presentation, 2D multi-scaffold assemblies provide extraordinary control over the spatial and stoichiometric arrangement of T cell ligands on any nearly antigen presentation surface imaginable. Further, these assemblies enable the construction of highly ordered supramolecular structures composed of multiple of T cell ligands, which can be designed to resemble the immunological synapse. Using orthogonal cohesin-dockerin binding pairs, scaffold-based assembly can direct the assembly of molecules associated with cSMAC (i.e. pMHC) to the center of the complex and simultaneously direct molecules associated with the p/dSMAC (i.e. ICAM-1) to the distal regions of the complex (**Figure 4.11b**).

4.6. Materials and Methods

4.6.1. Strains, Media and Reagents

The *S. cerevisiae* strain EBY100 (Invitrogen, Carlsbad, CA) was used for aScaf expression and 2D multi-scaffold assembly. The *E. coli* strains (Invitrogen) Mach1 and BL21 (DE3) were used for recombinant DNA engineering and protein expression, respectively. All recombinant yeast and *E. coli* strains are summarized in **Table 4.1**. *C. thermocellum* DSM1237, *C. cellulovorans*, *C. cellulolyticum* and *R. flavefaciens* were purchased from ATCC (Manassas, VA) and cultured anaerobically following ATCC protocols. Recombinant EBY100 cells were

cultured using SC-Trp medium: 1.67 g/L yeast nitrogen base without amino acids, 5 g/L ammonium sulfate (Difco Laboratories, Detroit, MI), 20 g/L glucose, 15 g/L adenine hemisulfate, and 0.64 g/L complete supplement mixture without tryptophan (MP Biomedicals, Solon, OH). Induction of aScaf expression on yeast cell surface was performed in YPG media (1% yeast extract, 2% peptone, 2% galactose). *E. coli* was cultured in Luria-Bertani (LB) medium containing 50 μg/mL kanamycin. Unless otherwise indicated, all chemicals were purchased from Sigma-Aldrich (St. Louis, MO).

4.6.2. Plasmid Construction, Protein Expression and Protein Purification

The aScaf and pScaf expression cassettes were cloned in pYD1 (Invitrogen, Carlsbad CA) and pET28a (Novagen, WI, USA), respectively. Sources of all protein sequences and primers used in this study are listed in **Table 4.1**. All plasmids were constructed using either homologous recombination in EBY100 or restriction-enzyme digestion and ligation in Mach1. aScaf surface expression was induced by incubating EBY100 strains transformed with pYD1-Aga2-V5, pYD1-aScaf1, pYD1-aScaf2, pYD1-aScaf3 in YPG for 60 hours at 20˚C. pScaf protein expression was induced by incubating BL21 (DE3) transformed with pET28a-pScaf, in LB with 0.1 mM isopropyl-β-D-thiogalactopyranoside (IPTG) overnight at 16 °C. The pScaf protein was then purified from BL21 (DE3) cell lysate using fast protein liquid chromatography (FPLC) with a HisTrap HP column (GE healthcare, Fairfield, CT). The 6×His tag on pScaf was cleaved using thrombin (EMD Millipore, Billerica, MA) according to the manufacturer's protocol following purification.

4.6.3. Quantitative Characterization of 2D Multi-scaffold Assembly

aScaf-pScaf assembly was performed by incubating 1.0 μM pScaf with 1.0×10^6 yeast displaying each aScaf design overnight at 4 ^{o}C in 50 mM PBS buffer (pH 7.4) containing 1.0% BSA. After incubation, cells were washed and co-stained using anti-V5-AF647 (Invitrogen) and anti-c-Myc-PE (Invitrogen) at 2 ng/μL of each antibody for one hour on ice. aScaf-pScaf assembly was assessed qualitatively using an Olympus FV-1200 confocal microscope (Olympus, Melville, NY) with a 60x objective. The yeast-cell displayed assemblies were then co-stained with anti-V5-AF647 and anti-c-Myc-AF647 (R&D Systems, Minneapolis, MN) at 2 ng/μL of each antibody for one hour on ice. Co-stained cells were then analyzed using flow cytometry and the MFI of each component was recorded. The number of aScaf and pScaf present on the yeast cell was determined using quantitative flow cytometry with Quantum^{TM} Alexa Fluor 647 and Quantum^{TM} R-PE fluorescence quantitation beads (Bangs Laboratories, Fishers, IN). Briefly, quantitation beads with four densities of molecules of equivalent soluble fluorophore (MESF) were analyzed by flow cytometry, and the MFI corresponding to each distinct density of fluorophores was determined. Using these data, MESF (provided by the manufacturer) was plotted with respect to MFI and linear regression was performed to derive a relationship between fluorescence intensity and fluorophore number. The number of aScaf and pScaf on each co-stained yeast cell was then determined using linear regression equation corresponding to the appropriate fluorophore.

4.6.4. Modeling aScaf Spatial Distribution on Yeast Cell Surface and 2D Multi-scaffold Assembly

aScaf spatial distribution on the yeast cell surface was modeled as a Poisson distribution in which the probability (P) that one aScaf had a distance to nearest neighbor of r is:

$$P(r) = 2\pi r\rho e^{-\pi r^2 \rho} \quad (4.1)$$

where ρ represents the aScaf surface density (i.e. aScaf expression level/ yeast surface area). Yeast cells were assumed to be spheres with a radius of 2 μm based on confocal imaging and a previous study.[344] The fraction of total aScaf (f_{aScaf}) with a distance to its nearest neighbor equal to or smaller than r is then found by integrating Equation 4.1 with respect to r:

$$f_{aScaf} = \int_0^r 2\pi r\rho e^{-\pi r^2 \rho}\, dr = 1 - e^{-\pi r^2 \rho} \quad (4.2)$$

The critical distance for aScaf1, aScaf2, and aScaf3 was determined by solving Equation 4.2 for an r value that best fit the experimental data in **Figure 4.9** using non-linear least squares regression. After determining the r_{crit} for each aScaf, the theoretical aScaf-pScaf assembly efficiency was determined with respect to aScaf expression levels (i.e. different ρ values) by solving Equation 4.2 to for f_{aScaf} with $r > r_{crit}$ at each aScaf expression level. The number of pScaf per aScaf was then found by multiplying the pScaf-aScaf assembly efficiency at a given aScaf expression level by the number of cohesins in each aScaf (i.e. 1 for aScaf1). The number of ligand per aScaf was similarly predicted as a function of aScaf expression level assuming 70% assembly pScaf-ligand assembly efficiency.

Chapter 5. Future Directions

T cell immunotherapy currently faces two significant challenges: difficulty identifying and isolating T cells recognizing appropriate antigenic targets and difficulty sustaining a robust and effective T cell response *in vivo*. In this dissertation, we have presented a set of quantitative and high-throughput molecular tools that are designed to address these limitations by enabling the rapid identification of immunologically relevant T cell epitopes and the fine-tuning of T cell activation through highly controlled artificial antigen presentation. Here, we will discuss future directions and ongoing research projects using these tools, and provide an outlook for the research area as a whole.

5.1. Enhanced Antigen-Specific T cell Detection

While the MAPS strategy introduced in **Chapter 2** allows for the rapid detection of promiscuously binding and potentially immunodominant T cell epitopes, MAPS alone is not capable of *isolating* T cells recognizing these epitopes. As discussed in **Chapter 1**, antigen-specific T cells are traditionally isolated by staining the peripheral T cell population with fluorescently labeled pMHC tetramers and performing fluorescence activated cell sorting (FACS).[42,71] This strategy has significantly improved our understanding of antigen-specific T cell phenotype and function; however, the binding affinity threshold for pMHC tetramer staining is insufficient to detect the entire T cell repertoire. The affinity limitation of pMHC tetramer

staining is especially problematic when the goal is to isolate self-reactive or tumor-reactive T cells, as these TCRs cells tend to bind their respective antigen with very low affinity.[70,71] One strategy that has been pursued to increase the detection limit of antigen-specific T cells is to engineer highly multivalent pMHC molecules that bind TCR with greater binding avidity.[71,72] A number of such pMHC multimers have been engineered to date,[73–77] and the sensitivity of T cell epitope detection generally correlates with the degree of pMHC multivalency.[77] Therefore, we are currently exploring the development of our own design of highly multivalent pMHC molecules for sensitive T cell epitope detection using protein-scaffold directed assembly.

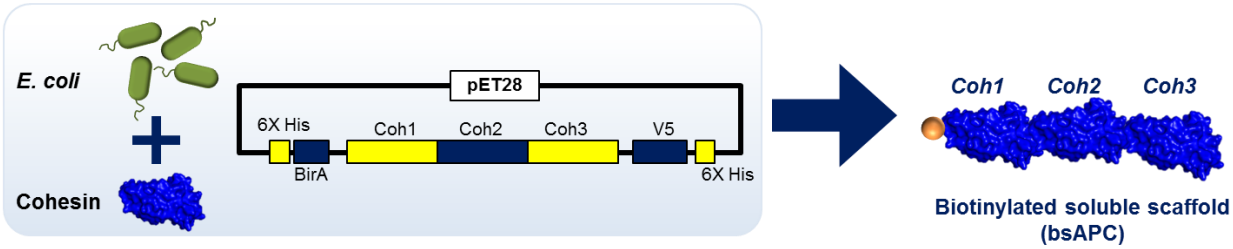

Figure 5.1. Schematic of bsAPC protein design.

In **Chapter 3**, we showed that soluble scaffolds (sAPCs) could be loaded with pMHC to create complexes with well-defined pMHC valency (**Figure 3.3c**). Further, we showed that these soluble multivalent pMHC complexes activated T cells in a valency-dependent manner (**Figure 3.5b**), suggesting that TCR crosslinking and triggering by soluble complexes is strongly dependent on pMHC valency. Building on this approach, we modified the sAPC design to include an N-terminal biotinylation site (**Figure 5.1**). The resulting biotinylated sAPCs (bsAPCs) could then be tetramerized using fluorescently labeled SAv to create even higher valency complexes, which we have called ultramers (**Figure 5.2a**). For example, ultramers formed using

bsAPC3 provide a total of 12 pMHC binding sites while ultramers formed using bsAPC6 provide a total of 24 pMHC binding sites.

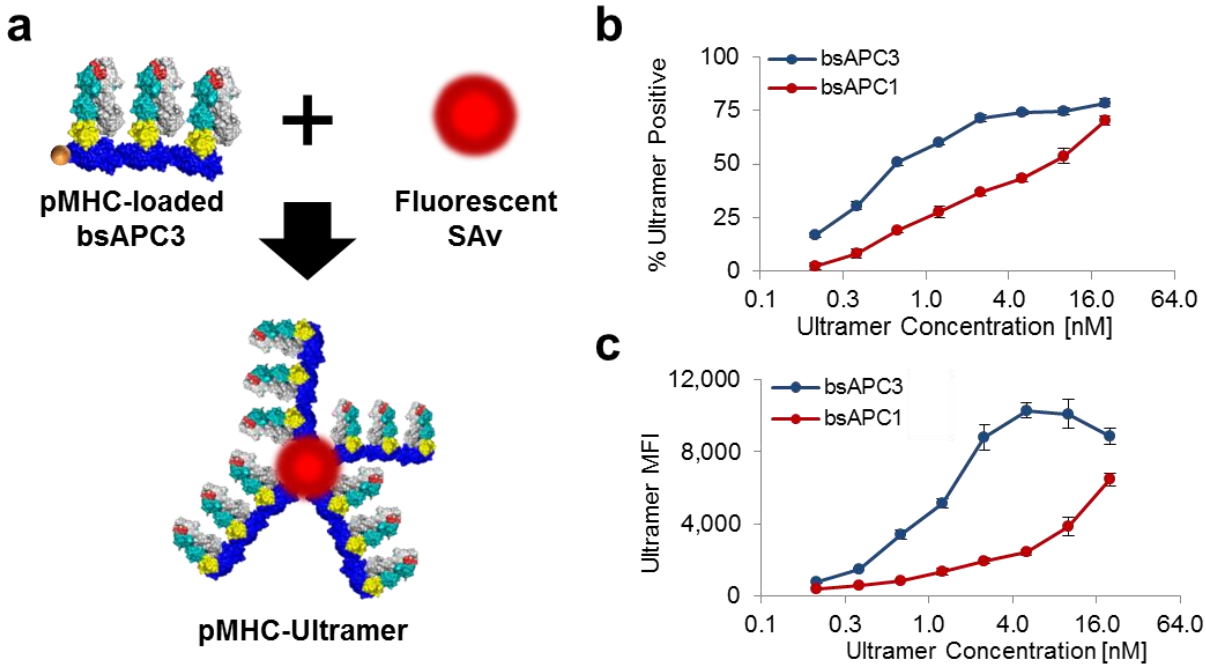

Figure 5.2. Schematic of pMHC ultramer formation and its use for antigen-specific T cell detection.
(a) pMHC ultramers are formed by incubating pMHC-loaded bsAPC scaffolds with fluorescently labeled SAv. (b) Percent of ultramer positive T cells when stained with various concentrations of ultramer formed with bsAPC1 or bsAPC3. (c) MFI of ultramer positive T cells when stained with various concentrations of pMHC ultramers formed with bsAPC1 or bsAPC3. Each point represents the mean of three independent trials and error bars represent standard deviation of the mean.

When used for antigen-specific T cell staining, pMHC ultramers formed with bsAPC3 significantly outperformed pMHC ultramers formed with bsAPC1 (functionally equivalent to tetramers) (**Figure 5.2b-c**). This observation is consistent with a recent study using pMHC dodecamers and provides further evidence that increasing the valency of fluorescent pMHC multimers increases the staining sensitivity.[77] Based on the idea that pMHC valency enhances staining sensitivity, a follow up study was performed using ultramers formed with bsAPC1, bsAPC3, and bsAPC6. While ultramers formed with bsAPC3 and bsAPC6 outperformed

ultramers formed with bsAPC1 in terms of T cell staining sensitivity, no significant difference was observed between ultramers formed with bsAPC3 and bsAPC6 (**Figure 5.3**). This could be due to the fact that the TCR being detected in these assays (HA1.7) binds its cognate pMHC (DR1-HA) with a sufficiently high affinity, such that the pMHC-TCR binding avidity is not significantly enhanced by increasing pMHC valency beyond 12. Additional studies using ultramer staining of peripheral antigen-specific T cells will be needed to determine if ultramers based on bsAPC6 can increase the detection limits of antigen-specific T cells beyond that of pMHC dodecamers.

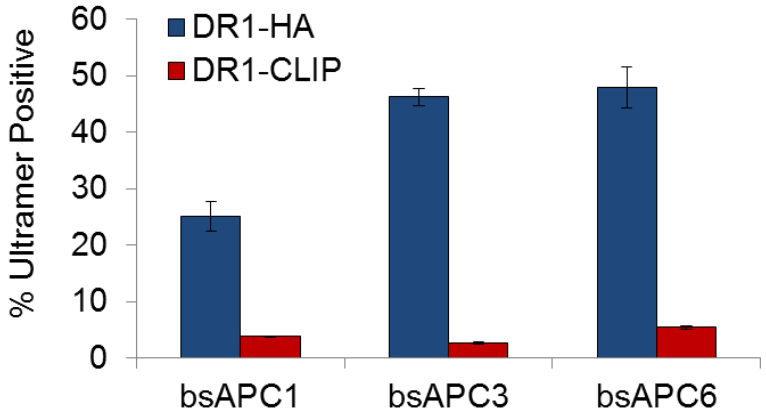

Figure 5.3. pMHC ultramer detection of antigen-specific T cells.
Frequency of ultramer positive T cells observed when staining with pMHC ultramers formed using bsAPC1, bsAPC3, or bsAPC6. Ultramers were loaded with either DR1-HA (agonist pMHC) or DR1-CLIP (negative control). Each point represents the mean of three independent trials and error bars represent standard deviation.

5.2. Highly Organized Acellular Artificial Antigen Presentation

In **Chapter 3**, we showed that yeast antigen presenting cells (yAPCs) could be used to finely tune T cell activation by controlling the spatial and stoichiometric organization of T cell ligands on surface-displayed scaffolds. While yAPCs provide a robust cellular platform for artificial antigen presentation, their microbial nature precludes their use in a clinical environment. Fortunately, functionalized sAPCs – like the bSAPCs described in **Section 5.2** –

allow organized protein-scaffold directed assemblies to be presented on a wide range of biocompatible surfaces. As we continue to explore applications of protein-scaffold directed artificial antigen presentation, we plan to transition to a biocompatible platform like biodegradable SAv-coated microparticles and/or nanoparticles. In addition to providing a more clinically relevant activation surface, acellular platforms allow the investigation of important physical parameters not possible on yeast including activation-surface rigidity,[345–347] size,[227,285] and shape.[218,225]

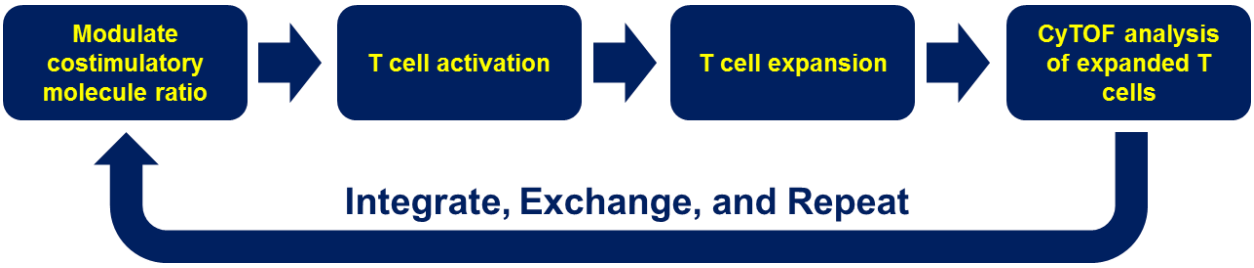

Figure 5.4. Systematic investigation of T cell activation using highly organized protein assemblies.
Systematic investigation of T cell activation can be performed in four steps. First, a panel of assemblies presenting various stoichiometric ratios of a target costimulatory molecule (or molecules) and pMHC are formed. Assemblies will be loaded on protein scaffolds, which are fixed to biocompatible particles. These assembly-displaying particles are then used to activate T cells. T cell activation is assessed by measuring cytokine secretion and monitoring T cell expansion. Finally, the phenotype of the expanded T cells is examined using CyTOF. This data is then analyzed and integrated with existing data, the costimulatory molecule assembly is exchanged, and the process is repeated.

Regardless of the specific presentation platform, our primary research goal is to systematically investigate how the spatial and stoichiometric organization of T cell ligand assemblies influences T cell activation. We have previously observed that $CD4^+$ T cell IL-2 secretion is maximized when the cells are stimulated with yAPCs presenting 85% ICAM-1 and 15% pMHC (**Figure 3.14a**). Based on this result, it is reasonable to assume that manipulating the

stoichiometric ratio of other costimulatory ligands could be used to optimize other T cell responses (e.g. T cell proliferation, Th1 polarization, etc.). Therefore, we plan to continue these studies going forward, expanding the scope of our investigation to include T cell proliferation capacity and T cell phenotype using high-dimensional tools like CyTOF (**Figure 5.4**). By including these additional outputs in our study of T cell activation, we can gain a deeper and more holistic understanding of how T cell signal integration translates to different functional responses. Further, this systematic approach to investigating T cell activation by high-dimensional phenotypic analysis could elucidate biomarkers or – patterns of biomarkers – that correlate with either effective or ineffective T cell phenotypes for a particular immunotherapeutic application. Once optimal presentation patterns are understood (e.g. optimum ICAM-1 pMHC ratio), we can shift our focus to the development of off-the-shelf aAPCs custom engineered to elicit specific T cell responses.

5.3. Final Thoughts

T cell immunotherapy is a broad and interdisciplinary research area involving immunology, biostatistics, computer science, molecular biology, and engineering. Given the scope of T cell immunotherapy research, the tools described in this dissertation represent just one of many strategies for addressing some of the more intractable challenges in the field. Further, as our understanding of T cell biology – and the immune system more broadly – improves, new challenges will certainly emerge, as others are resolved. Therefore, I will conclude with a brief discussion of where I believe the field is headed, and what tools and strategies are likely to be important in the future.

In this dissertation, we have focused on tools related to $CD4^+$ T cell identification and activation. In contrast, most immunotherapy research focuses exclusively on activating and expanding $CD8^+$ T cells. $CD8^+$ T cells execute effector functions directly on the targeted cell, and thus are indispensable for most types of T cell immunotherapy; however, $CD4^+$ T cells play an important role in sustaining a $CD8^+$ T cell response, as well as activating B cells. In fact, a number of studies have suggested that the presence of $CD4^+$ T cells promotes more robust anti-tumor $CD8^+$ T cell responses,[138,348–351] and that $CD4^+$ T cells alone can also mediate tumor regression.[352] These findings highlight the fact that the functional relationship between $CD4^+$ T cells and $CD8^+$ T cells is not fully understood. Therefore, researchers should avoid rigid and potentially superficial categorization and instead investigate how the synergistic activity of $CD4^+$ and $CD8^+$ T cells can be leveraged to achieve an optimal T cell response.

While rapid development and FDA approval of CAR T cell therapy speaks to its therapeutic potential, the most broadly efficacious immunotherapies developed to date are immune checkpoint inhibitors.[353] Immune checkpoint inhibitors are monoclonal antibodies that bind to inhibitory proteins like PD-L1 and CTLA-4, effectively blocking T cells from integrating the signals that attenuate T cell activation. Because immunosuppression within the tumor microenvironment continues to pose a significant challenge for cell-based immunotherapies in solid tumors, a combination of checkpoint inhibitors with such therapies should improve overall treatment efficacy. Similarly, as computational and technological advances improve the science of protein engineering, combining deliverable therapies with cell-based approaches should also provide new methods for disrupting immunosuppression in tumors and tuning T cell response *in situ*.

An important consideration that is often underappreciated in academic research laboratories is how market and regulatory forces shape the risk profile of particular drugs or therapies. For example, non-cell based drugs and biologics have a well-established regulatory framework for their development and approval. In contrast, the regulatory landscape for cell-based therapies is poorly defined and likely to change, which translates to greater risk for pharmaceutical companies pursuing these therapies. These regulatory considerations will likely incentivize the development of more conventional therapies with better-defined risk profiles into the future. Therefore, it will be important to understand how ambitious cell-based immunotherapies interact and synergize with the pipeline of conventional drugs and biologics.

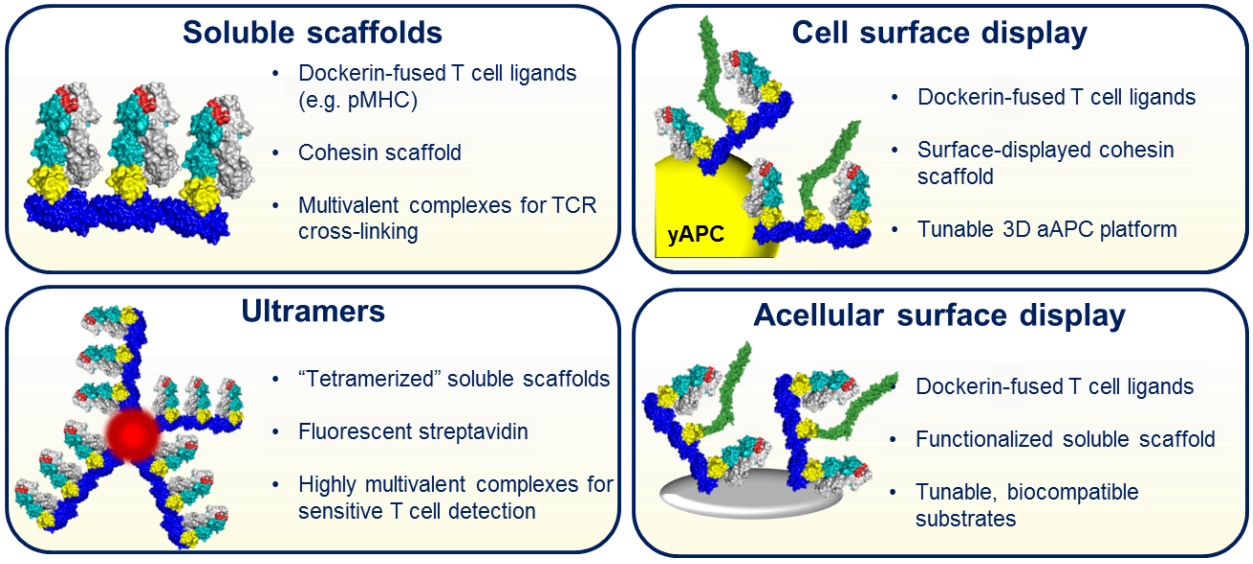

Figure 5.5. Molecular tools for isolating and activating antigen-specific T cells.

Finally, as the information bottleneck shifts from data acquisition to data analysis, computational methods will likely play an increasingly prominent role in generating new insights. This paradigm shift toward high-dimensional data analysis has been catalyzed by

technological breakthroughs that substantially increase the number of parameters that can be studied in a single experiment (e.g. whole genome/exome sequencing and CyTOF). In **Chapter 1** and **Chapter 2**, we briefly discussed the promise demonstrated by machine learning methods using artificial neural networks in predicting peptide-MHC binding. Similar methods should continue to play an important role in analyzing and deconvoluting highly complex datasets as new high-dimensional tools like CyTOF and rapid whole-exome sequencing become more widely used.[354,355] Further, because machine learning methods improve as the amount of relevant data increases, systematic studies that aim to fully characterize the space of possible T cell responses should be more valuable than previously thought. For example, a significant volume of phenotypic data correlating with ineffective, inappropriate, or counterintuitive T cell responses could generate profound insights – that would otherwise never occur – when fed into advanced artificial neural networks.

In this dissertation, we have introduced a novel set of molecular tools that are designed to address some of the more difficult challenges facing T cell immunotherapy (**Figure 5.5**). Like all tools, we cannot envision every possible application at the time of development. Similarly, the most appropriate application of each tool discussed will likely change over time. Nevertheless, we believe that protein-scaffold directed assembly is an exciting toolset that will continue to have a wide range of applications in molecular biology and immunology in the future.[356]

References

1. Robinson, J. *et al.* The IPD and IMGT/HLA database: Allele variant databases. *Nucleic Acids Res.* **43,** D423–D431 (2015).

2. Zhang, Y. *et al.* CD8+ T-Cell Response-Associated Evolution of Hepatitis B Virus Core Protein and Disease Progress. *J. Virol.* JVI.02120-17 (2018). doi:10.1128/JVI.02120-17

3. Painter, C. A. *et al.* Conformational lability in the class II MHC 310 helix and adjacent extended strand dictate HLA-DM susceptibility and peptide exchange. *Proc. Natl. Acad. Sci.* **108,** 19329–19334 (2011).

4. Rammensee, H. G., Falk, K. & Rötzschke, O. Peptides naturally presented by MHC class I molecules. *Annu. Rev. Immunol.* **11,** 213–44 (1993).

5. Neefjes, J., Jongsma, M. L. M., Paul, P. & Bakke, O. Towards a systems understanding of MHC class I and MHC class II antigen presentation. *Nat. Rev. Immunol.* **11,** 823–836 (2011).

6. Chicz, R., Urban, R., Lane, W. & Gorga, J. Predominant naturally processed peptides bound to HLA-DR1 are derived from MHC-related molecules and are heterogeneous in size. *Nat. az index* (1992).

7. Sturniolo, T. *et al.* Generation of tissue-specific and promiscuous HLA ligand databases using DNA microarrays and virtual HLA class II matrices. *Nat. Biotechnol.* **17,** 555–61 (1999).

8. Consogno, G. *et al.* Identification of immunodominant regions among promiscuous HLA-DR-restricted CD4+ T-cell epitopes on the tumor antigen MAGE-3. *Blood* **101,** 1038–44 (2003).

9. Bui, H. H. *et al.* Predicting population coverage of T-cell epitope-based diagnostics and vaccines. *BMC Bioinformatics* **7,** 1–5 (2006).

10. Patronov, A. & Doytchinova, I. T-cell epitope vaccine design by immunoinformatics T-cell epitope vaccine design by immunoinformatics. *Open Biol.* **3,** 120–139 (2013).

11. Jones, E. Y., Fugger, L., Strominger, J. L. & Siebold, C. MHC class II proteins and disease: a structural perspective. *Nat. Rev. Immunol.* **6,** 271–82 (2006).

12. Holland, C. J., Cole, D. K. & Godkin, A. Re-Directing CD4(+) T Cell Responses with the Flanking Residues of MHC Class II-Bound Peptides: The Core is Not Enough. *Front. Immunol.* **4,** 172 (2013).

13. Arnold, P. Y. *et al.* The majority of immunogenic epitopes generate CD4+ T cells that are dependent on MHC class II-bound peptide-flanking residues. *J. Immunol.* **169,** 739–49 (2002).

14. Lafuente, E. M. & Reche, P. a. Prediction of MHC-peptide binding: a systematic and comprehensive overview. *Curr. Pharm. Des.* **15,** 3209–20 (2009).

15. Brusic, V., Rudy, G., Honeyman, G., Hammer, J. & Harrison, L. Prediction of MHC class II-binding peptides using an evolutionary algorithm and artificial neural network. *Bioinformatics* **14,** 121–130 (1998).

16. Nielsen, M. *et al.* Reliable prediction of T-cell epitopes using neural networks with novel sequence representations. *Protein Sci.* **12,** 1007–1017 (2003).

17. Luo, H. *et al.* Machine Learning Methods for Predicting HLA-Peptide Binding Activity. *Bioinform. Biol. Insights* **9,** 21–9 (2015).

18. Jensen, K. K. *et al.* Improved methods for predicting peptide binding affinity to MHC class II molecules. *Immunology* 1–13 (2018). doi:10.1111/imm.12889

19. Zhang, L., Udaka, K., Mamitsuka, H. & Zhu, S. Toward more accurate pan-specific MHC-peptide binding prediction: A review of current methods and tools. *Brief. Bioinform.* **13,** 350–364 (2012).

20. Nielsen, M. & Lund, O. NN-align. An artificial neural network-based alignment algorithm for MHC class II peptide binding prediction. *BMC Bioinformatics* **10,** 296 (2009).

21. Reche, P. a, Glutting, J.-P. & Reinherz, E. L. Prediction of MHC class I binding peptides using profile motifs. *Hum. Immunol.* **63,** 701–9 (2002).

22. Nielsen, M., Lundegaard, C. & Lund, O. Prediction of MHC class II binding affinity using SMM-align, a novel stabilization matrix alignment method. *BMC Bioinformatics* **8,** 238 (2007).

23. Reche, P. A. & Reinherz, E. L. in *Immunoinformatics: Predicting Immunogenicity In Silico* (ed. Flower, D. R.) 185–200 (Humana Press, 2007). doi:10.1007/978-1-60327-118-9_13

24. Hattotuwagama, C. K., Doytchinova, I. A. & Flower, D. R. in *Immunoinformatics: Predicting Immunogenicity In Silico* (ed. Flower, D. R.) 227–245 (Humana Press, 2007). doi:10.1007/978-1-60327-118-9_16

25. Kumar, N. & Mohanty, D. MODPROPEP: A program for knowledge-based modeling of protein-peptide complexes. *Nucleic Acids Res.* **35,** 549–555 (2007).

26. Huang, M., Huang, W., Wen, F. & Larson, R. G. Efficient estimation of binding free energies between peptides and an MHC class II molecule using coarse-grained molecular dynamics simulations with a weighted histogram analysis method. *J. Comput. Chem.* **38,** 2007–2019 (2017).

27. Lin, H. H., Zhang, G. L., Tongchusak, S., Reinherz, E. L. & Brusic, V. Evaluation of MHC-II peptide binding prediction servers: Applications for vaccine research. *BMC Bioinformatics* **9,** 1–10 (2008).

28. Meydan, C., Otu, H. H. & Sezerman, O. U. Prediction of peptides binding to MHC class I and II alleles by temporal motif mining. *BMC Bioinformatics* **14,** S13 (2013).

29. Liao, W. W. P. & Arthur, J. W. Predicting peptide binding to Major Histocompatibility Complex molecules. *Autoimmun. Rev.* **10,** 469–473 (2011).

30. Zhang, H. *et al.* Limitations of ab initio predictions of peptide binding to MHC class II molecules. *PLoS One* **5,** (2010).

31. Justesen, S., Harndahl, M., Lamberth, K., Nielsen, L. L. B. & Buus, S. Functional recombinant MHC class II molecules and high-throughput peptide-binding assays. *Immunome Res.* **5,** (2009).

32. Yin, L. & Stern, L. J. Measurement of peptide binding to MHC class II molecules by fluorescence polarization. *Curr. Protoc. Immunol.* **2014,** 5.10.1-5.10.12 (2014).

33. Salvat, R., Moise, L., Bailey-Kellogg, C. & Griswold, K. E. A High Throughput MHC II Binding Assay for Quantitative Analysis of Peptide Epitopes. *J. Vis. Exp.* **85,** 1–11 (2014).

34. Sylvester-Hvid, C. *et al.* Establishment of a quantitative ELISA capable of determining peptide - MHC class I interaction. *Tissue Antigens* **59,** 251–8 (2002).

35. Bernardeau, K. *et al.* A simple competitive assay to determine peptide affinity for HLA class II molecules: A useful tool for epitope prediction. *J. Immunol. Methods* **371,** 97–105 (2011).

36. Jiang, W. & Boder, E. T. High-throughput engineering and analysis of peptide binding to class II MHC. *Proc. Natl. Acad. Sci. U. S. A.* **107,** 13258–63 (2010).

37. Novak, E. J. *et al.* Tetramer-guided epitope mapping: rapid identification and characterization of immunodominant CD4+ T cell epitopes from complex antigens. *J. Immunol.* **166,** 6665–70 (2001).

38. Tacken, P. J., de Vries, I. J. M., Torensma, R. & Figdor, C. G. Dendritic-cell immunotherapy: from ex vivo loading to in vivo targeting. *Nat. Rev. Immunol.* **7,** 790–802 (2007).

39. Larché, M. & Wraith, D. C. Peptide-based therapeutic vaccines for allergic and autoimmune diseases. *Nat. Med.* **11,** S69-76 (2005).

40. Purcell, A. W., McCluskey, J. & Rossjohn, J. More than one reason to rethink the use of peptides in vaccine design. *Nat. Rev. Drug Discov.* **6,** 404–414 (2007).

41. Wen, F. & Zhao, H. in *Immunoproteomics: Methods and Protocols* (eds. Fulton, K. M. & Twine, S. M.) 245–264 (Humana Press, 2013). doi:10.1007/978-1-62703-589-7_15

42. Altman, J. J. D. *et al.* Phenotypic analysis of antigen-specific T lymphocytes. *Science* **274,** 94–6 (1996).

43. Novak, E. J., Liu, A. W., Nepom, G. T. & Kwok, W. W. MHC class II tetramers identify peptide-specific human CD4+ T cells proliferating in response to influenza A antigen. *J. Clin. Invest.* **104,** 63–67 (1999).

44. Grotenbreg, G. M. *et al.* Discovery of CD8+ T cell epitopes in Chlamydia trachomatis infection through use of caged class I MHC tetramers. *Proc. Natl. Acad. Sci. U. S. A.* **105,** 3831–6 (2008).

45. Bakker, A. H. *et al.* Conditional MHC class I ligands and peptide exchange technology for the human MHC gene products HLA-A1, -A3, -A11, and -B7. *Proc. Natl. Acad. Sci. U. S. A.* **105,** 3825–30 (2008).

46. Day, C. L. *et al.* Ex vivo analysis of human memory CD4 T cells specific for hepatitis C virus using MHC class II tetramers. *J. Clin. Invest.* **112,** 831–42 (2003).

47. Newell, E. W., Klein, L. O., Yu, W. & Davis, M. M. Simultaneous detection of many T-cell specificities using combinatorial tetramer staining. *Nat. Methods* **6,** 497–9 (2009).

48. Newell, E. W. *et al.* Combinatorial tetramer staining and mass cytometry analysis facilitate T-cell epitope mapping and characterization. *Nat. Biotechnol.* **31,** 623–9 (2013).

49. Moon, J. J. *et al.* Naive CD4+T Cell Frequency Varies for Different Epitopes and Predicts Repertoire Diversity and Response Magnitude. *Immunity* **27,** 203–213 (2007).

50. Vita, R. *et al.* The immune epitope database (IEDB) 3.0. *Nucleic Acids Res.* **43,** D405-12 (2015).

51. Arstila, T. P. *et al.* A direct estimate of the human alphabeta T cell receptor diversity. *Science* **286,** 958–61 (1999).

52. Zarnitsyna, V. I., Evavold, B. D., Schoettle, L. N., Blattman, J. N. & Antia, R. Estimating the diversity, completeness, and cross-reactivity of the T cell repertoire. *Front. Immunol.* **4,** 1–11 (2013).

53. James, E. A. *et al.* Tetramer-guided epitope mapping reveals broad, individualized repertoires of tetanus toxin-specific CD4+ T cells and suggests HLA-based differences in epitope recognition. *Int. Immunol.* **19,** 1291–1301 (2007).

54. Scriba, T. J. *et al.* Ultrasensitive detection and phenotyping of CD4+ T cells with optimized HLA class II tetramer staining. *J. Immunol.* **175,** 6334–6343 (2005).

55. Appay, V. & Rowland-Jones, S. L. The assessment of antigen-specific CD8+ T cells through the combination of MHC class I tetramer and intracellular staining. *J. Immunol. Methods* **268,** 9–19 (2002).

56. Cohen, C. J. *et al.* Isolation of neoantigen-specific T cells from tumor and peripheral lymphocytes. *J. Clin. Invest.* **125,** 3981–3991 (2015).

57. Schmidt, J., Dojcinovic, D., Guillaume, P. & Luescher, I. Analysis, isolation, and activation of antigen-specific CD4+ and CD8+ T cells by soluble MHC-peptide complexes. *Front. Immunol.* **4,** 1–14 (2013).

58. Fourneau, J. M., Cohen, H. & Van Endert, P. M. A chaperone-assisted high yield system for the production of HLA-DR4 tetramers in insect cells. *J. Immunol. Methods* **285,** 253–264 (2004).

59. van Rooij, N. *et al.* Tumor Exome Analysis Reveals Neoantigen-Specific T-Cell Reactivity in an Ipilimumab-Responsive Melanoma. *J. Clin. Oncol.* **31,** e439–e442 (2013).

60. Strønen, E. *et al.* Targeting of cancer neoantigens with donor-derived T cell receptor repertoires. *Science* **352,** 1337–41 (2016).

61. Schumacher, T. N. & Schreiber, R. D. Neoantigens in cancer immunotherapy. *Science (80-.).* **348,** 69–74 (2015).

62. Ornatsky, O., Kinach, R. & Bandura, D. Development of analytical methods for multiplex bio-assay with inductively coupled plasma mass spectrometry. *J. Anal. At. Spectrom.* **23,** 463–469 (2008).

63. Spitzer, M. H. & Nolan, G. P. Mass Cytometry: Single Cells, Many Features. *Cell* **165,** 780–791 (2016).

64. Germain, R. N. & Hoffmann, A. What Can Immunologists Learn from Systems Approaches? *Trends Immunol.* **39,** 163–166 (2018).

65. Yao, Y. *et al.* CyTOF supports efficient detection of immune cell subsets from small samples. *J. Immunol. Methods* **415,** 1–5 (2014).

66. Newell, E. W., Sigal, N., Bendall, S. C., Nolan, G. P. & Davis, M. M. Cytometry by Time-of-Flight Shows Combinatorial Cytokine Expression and Virus-Specific Cell Niches within a Continuum of CD8+T Cell Phenotypes. *Immunity* **36,** 142–152 (2012).

67. Newell, E. W. & Davis, M. M. Beyond model antigens: High-dimensional methods for the analysis of antigen-specific T cells. *Nat. Biotechnol.* **32,** 149–157 (2014).

68. Laugel, B. *et al.* Different T cell receptor affinity thresholds and CD8 coreceptor dependence govern cytotoxic T lymphocyte activation and tetramer binding properties. *J. Biol. Chem.* **282,** 23799–23810 (2007).

69. Sabatino, J. J., Huang, J., Zhu, C. & Evavold, B. D. High prevalence of low affinity peptide-MHC II tetramer-negative effectors during polyclonal CD4+ T cell responses. *J. Exp. Med.* **208,** 81–90 (2011).

70. Cole, D. K. *et al.* Human TCR-binding affinity is governed by MHC class restriction. *J. Immunol.* **178,** 5727–34 (2007).

71. Wooldridge, L. *et al.* Tricks with tetramers: how to get the most from multimeric peptide-MHC. *Immunology* **126,** 147–164 (2009).

72. Davis, M. M., Altman, J. D. & Newell, E. W. Interrogating the repertoire: broadening the scope of peptide-MHC multimer analysis. *Nat. Rev. Immunol.* **11,** 551–8 (2011).

73. Guillaume, P. *et al.* Soluble major histocompatibility complex-peptide octamers with impaired CD8 binding selectively induce Fas-dependent apoptosis. *J. Biol. Chem.* **278,** 4500–4509 (2003).

74. Batard, P. *et al.* Dextramers: New generation of fluorescent MHC class I/peptide multimers for visualization of antigen-specific CD8+T cells. *J. Immunol. Methods* **310,** 136–148 (2006).

75. Dolton, G. *et al.* Comparison of peptide-major histocompatibility complex tetramers and dextramers for the identification of antigen-specific T cells. *Clin. Exp. Immunol.* **177,** 47–63 (2014).

76. Massilamany, C., Krishnan, B. & Reddy, J. Major Histocompatibility Complex Class II Dextramers: New Tools for the Detection of antigen-Specific, CD4 T Cells in Basic and Clinical Research. *Scand. J. Immunol.* **82,** 399–408 (2015).

77. Huang, J. *et al.* Detection, phenotyping, and quantification of antigen-specific T cells using a peptide-MHC dodecamer. *Proc. Natl. Acad. Sci. U. S. A.* 201602488 (2016). doi:10.1073/pnas.1602488113

78. Karjalainen, K. High sensitivity, low affinity--paradox of T-cell receptor recognition. *Curr. Opin. Immunol.* **6,** 9–12 (1994).

79. van der Merwe, P. A. & Dushek, O. Mechanisms for T cell receptor triggering. *Nat. Rev. Immunol.* **11,** 47–55 (2011).

80. Cochran, J. R., Cameron, T. O. & Stern, L. J. The Relationship of MHC-Peptide Binding and T Cell Activation Probed Using Chemically Defined MHC Class II Oligomers. *Immunity* **12,** 241–250 (2000).

81. Irvine, D. J., Purbhoo, M. a, Krogsgaard, M. & Davis, M. M. Direct observation of ligand recognition by T cells. *Nature* **419,** 845–9 (2002).

82. Veillette, a, Bookman, M. a, Horak, E. M. & Bolen, J. B. The CD4 and CD8 T cell surface antigens are associated with the internal membrane tyrosine-protein kinase p56lck. *Cell* **55,** 301–308 (1988).

83. Li, Q.-J. *et al.* CD4 enhances T cell sensitivity to antigen by coordinating Lck accumulation at the immunological synapse. *Nat. Immunol.* **5,** 791–799 (2004).

84. Krogsgaard, M., Li, Q., Sumen, C. & Huppa, J. B. Agonist / endogenous peptide – MHC heterodimers drive T cell activation and sensitivity. *Nature* **434,** 6–11 (2005).

85. Hampl, J., Chien, Y. H. & Davis, M. M. CD4 augments the response of a T cell to agonist but not to antagonist ligands. *Immunity* **7,** 379–385 (1997).

86. Locksley, R. M., Reiner, S. L., Hatam, F., Littman, D. R. & Killeen, N. Helper T cells without CD4: control of leishmaniasis in CD4-deficient mice. *Science* **261,** 1448–1451 (1993).

87. Ma, Z., Sharp, K. a., Janmey, P. a. & Finkel, T. H. Surface-anchored monomeric agonist pMHCs alone trigger TCR with high sensitivity. *PLoS Biol.* **6,** e43 (2008).

88. Klotzsch, E., Stiegler, J., Ben-Ishay, E. & Gaus, K. Do mechanical forces contribute to nanoscale membrane organisation in T cells? *Biochim. Biophys. Acta - Mol. Cell Res.* **1853,** 822–829 (2015).

89. Ma, Z., Janmey, P. A. & Finkel, T. H. The receptor deformation model of TCR triggering. *FASEB J.* **22,** 1002–1008 (2007).

90. Ma, Z., Discher, D. E. & Finkel, T. H. Mechanical force in T cell receptor signal initiation. *Front. Immunol.* **3,** 2–4 (2012).

91. Li, Y.-C. *et al.* Cutting Edge: mechanical forces acting on T cells immobilized via the TCR complex can trigger TCR signaling. *J. Immunol.* **184,** 5959–5963 (2010).

92. Gil, D., Schrum, A. G., Alarcón, B. & Palmer, E. T cell receptor engagement by peptide-MHC ligands induces a conformational change in the CD3 complex of thymocytes. *J. Exp. Med.* **201,** 517–522 (2005).

93. Beddoe, T. *et al.* Antigen Ligation Triggers a Conformational Change within the Constant Domain of the αβ T Cell Receptor. *Immunity* **30,** 777–788 (2009).

94. Kuhns, M. S. & Davis, M. M. The Safety on the TCR Trigger. *Cell* **135,** 594–596 (2008).

95. Xu, C. *et al.* Regulation of T Cell Receptor Activation by Dynamic Membrane Binding of the CD3?? Cytoplasmic Tyrosine-Based Motif. *Cell* **135,** 702–713 (2008).

96. Imbert, V. *et al.* Induction of tyrosine phosphorylation and T-cell activation by vanadate peroxide, an inhibitor of protein tyrosine phosphatases. *Biochem. J.* **297 (Pt 1,** 163–173 (1994).

97. Liu, B., Chen, W., Evavold, B. D. & Zhu, C. Accumulation of dynamic catch bonds between TCR and agonist peptide-MHC triggers T cell signaling. *Cell* **157,** 357–368 (2014).

98. Minguet, S., Swamy, M., Alarcón, B., Luescher, I. F. & Schamel, W. W. a. Full Activation of the T Cell Receptor Requires Both Clustering and Conformational Changes at CD3. *Immunity* **26,** 43–54 (2007).

99. Malissen, B. & Bongrand, P. Early T Cell Activation: Integrating Biochemical, Structural, and Biophysical Cues. *Annu. Rev. Immunol.* **33,** 539–561 (2015).

100. McCall, M. N., Shotton, D. M. & Barclay, a N. Expression of soluble isoforms of rat CD45. Analysis by electron microscopy and use in epitope mapping of anti-CD45R monoclonal antibodies. *Immunology* **76,** 310–317 (1992).

101. Anton van der Merwe, P., Davis, S. J., Shaw, a S. & Dustin, M. L. Cytoskeletal polarization and redistribution of cell-surface molecules during T cell antigen recognition. *Semin. Immunol.* **12,** 5–21 (2000).

102. Davis, S. J. & van der Merwe, P. A. The kinetic-segregation model: TCR triggering and beyond. *Nat. Immunol.* **7,** 803–809 (2006).

103. Nika, K. *et al.* Constitutively active lck kinase in T cells drives antigen receptor signal transduction. *Immunity* **32,** 766–777 (2010).

104. Cordoba, S. P. *et al.* The large ectodomains of CD45 and CD148 regulate their segregation from and inhibition of ligated T-cell receptor. *Blood* **121,** 4295–4302 (2013).

105. James, J. R. & Vale, R. D. Biophysical mechanism of T-cell receptor triggering in a reconstituted system. *Nature* **487,** 64–69 (2012).

106. Ma, Z. *et al.* TCR Triggering by pMHC Ligands Tethered on Surfaces via Poly(Ethylene Glycol) Depends on Polymer Length. *PLoS One* **9,** e112292 (2014).

107. Choudhuri, K., Wiseman, D., Brown, M. H., Gould, K. & van der Merwe, P. A. T-cell receptor triggering is critically dependent on the dimensions of its peptide-MHC ligand. *Nature* **436,** 578–582 (2005).

108. Grakoui, A. *et al.* The Immunological Synapse: A Molecular Machine Controlling T Cell Activation. *Science (80-.).* **285,** 221–227 (1999).

109. Bromley, S. K. *et al.* The Immunological Synapse. *Annu. Rev. Immunol.* **19,** 375–396 (2001).

110. Gimmi, C. D., Freeman, G. J., Gribben, J. G., Gray, G. & Nadler, L. M. Human T-cell clonal anergy is induced by antigen presentation in the absence of B7 costimulation. *Proc. Natl. Acad. Sci. U. S. A.* **90,** 6586–6590 (1993).

111. Appleman, L. J. & Boussiotis, V. a. T cell anergy and costimulation. *Immunol. Rev.* **192,** 161–180 (2003).

112. Getts, D. R. *et al.* Microparticles bearing encephalitogenic peptides induce T-cell tolerance and ameliorate experimental autoimmune encephalomyelitis. *Nat. Biotechnol.* **30,** 1217–24 (2012).

113. Paulos, C. M. *et al.* The inducible costimulator (ICOS) is critical for the development of human T(H)17 cells. *Sci. Transl. Med.* **2,** 55ra78 (2010).

114. Verma, N. K. *et al.* LFA-1/ICAM-1 Ligation in Human T Cells Promotes Th1 Polarization through a GSK3β Signaling-Dependent Notch Pathway. *J. Immunol.* **197,** 108–18 (2016).

115. Verma, N. K. & Kelleher, D. Not Just an Adhesion Molecule: LFA-1 Contact Tunes the T Lymphocyte Program. *J. Immunol.* **199,** 1213–1221 (2017).

116. Long, A. H. *et al.* 4-1BB costimulation ameliorates T cell exhaustion induced by tonic signaling of chimeric antigen receptors. *Nat. Med.* **21,** 581–90 (2015).

117. Chen, L. & Flies, D. B. Molecular mechanisms of T cell co-stimulation and co-inhibition. *Nat. Rev. Immunol.* **13,** 227–242 (2013).

118. Sanchez-Lockhart, M. *et al.* Cutting edge: CD28-mediated transcriptional and posttranscriptional regulation of IL-2 expression are controlled through different signaling pathways. *J. Immunol.* **173,** 7120–7124 (2004).

119. Holdorf, A. D., Lee, K.-H., Burack, W. R., Allen, P. M. & Shaw, A. S. Regulation of Lck activity by CD4 and CD28 in the immunological synapse. *Nat. Immunol.* **3,** 259–264 (2002).

120. Damle, N. K., Klussman, K., Linsley, P. S. & Aruffo, A. Differential costimulatory effects of adhesion molecules B7, ICAM-1, LFA-3, and VCAM-1 on resting and antigen-primed CD4+ T lymphocytes. *J. Immunol.* **148,** 1985–92 (1992).

121. Parameswaran, N., Suresh, R., Bal, V., Rath, S. & George, a. Lack of ICAM-1 on APCs during T Cell Priming Leads to Poor Generation of Central Memory Cells. *J. Immunol.* **175,** 2201–2211 (2005).

122. Wülfing, C., Sjaastad, M. D. & Davis, M. M. Visualizing the dynamics of T cell activation: intracellular adhesion molecule 1 migrates rapidly to the T cell/B cell interface and acts to sustain calcium levels. *Proc. Natl. Acad. Sci. U. S. A.* **95,** 6302–6307 (1998).

123. Zhang, H. *et al.* 4-1BB Is Superior to CD28 Costimulation for Generating CD8+ Cytotoxic Lymphocytes for Adoptive Immunotherapy. *J. Immunol.* **179,** 4910–4918 (2007).

124. Curran, M. a *et al.* Systemic 4-1BB activation induces a novel T cell phenotype driven by high expression of Eomesodermin. *J. Exp. Med.* **210,** 743–55 (2013).

125. Vinay, D. S. & Kwon, B. S. 4-1BB (CD137), an inducible costimulatory receptor, as a specific target for cancer therapy. *BMB Rep.* **47,** 122–9 (2014).

126. Suhoski, M. M. *et al.* Engineering artificial antigen-presenting cells to express a diverse array of co-stimulatory molecules. *Mol. Ther.* **15,** 981–8 (2007).

127. Zeng, W., Su, M., Anderson, K. S. & Sasada, T. Artificial antigen-presenting cells expressing CD80, CD70, and 4-1BB ligand efficiently expand functional T cells specific to tumor-associated antigens. *Immunobiology* **219,** 583–92 (2014).

128. Hodge, J. W. *et al.* A triad of costimulatory molecules synergize to amplify T-cell activation. *Cancer Res.* **59,** 5800–7 (1999).

129. Pentcheva-Hoang, T., Egen, J. G., Wojnoonski, K. & Allison, J. P. B7-1 and B7-2 selectively recruit CTLA-4 and CD28 to the immunological synapse. *Immunity* **21,** 401–413 (2004).

130. Qureshi, O. S. *et al.* Trans-endocytosis of CD80 and CD86: a molecular basis for the cell-extrinsic function of CTLA-4. *Science* **332,** 600–603 (2011).

131. Kim, R., Emi, M. & Tanabe, K. Cancer immunosuppression and autoimmune disease: Beyond immunosuppressive networks for tumour immunity. *Immunology* **119,** 254–264 (2006).

132. Pauken, K. E. & Wherry, E. J. Overcoming T cell exhaustion in infection and cancer. *Trends Immunol.* **36,** 265–276 (2015).

133. Chen, W. *et al.* Conversion of peripheral CD4+CD25- naive T cells to CD4+CD25+ regulatory T cells by TGF-beta induction of transcription factor Foxp3. *J. Exp. Med.* **198,** 1875–86 (2003).

134. Kremer, J. M. *et al.* Treatment of rheumatoid arthritis by selective inhibition of T-cell activation with fusion protein CTLA4Ig. *N. Engl. J. Med.* **349,** 1907–15 (2003).

135. Prakken, B. J. *et al.* Epitope-specific immunotherapy induces immune deviation of proinflammatory T cells in rheumatoid arthritis. *Proc. Natl. Acad. Sci. U. S. A.* **101,** 4228–33 (2004).

136. Seo, S. K. *et al.* 4-1BB-mediated immunotherapy of rheumatoid arthritis. **10,** 1088–1094 (2004).

137. Bluestone, J. A. *et al.* Type 1 diabetes immunotherapy using polyclonal regulatory T cells. *Sci. Transl. Med.* **7,** 315ra189 (2015).

138. Kamphorst, A. O. & Ahmed, R. CD4 T-cell immunotherapy for chronic viral infections and cancer. *Immunotherapy* **5,** 975–987 (2013).

139. Barber, D. L. *et al.* Restoring function in exhausted CD8 T cells during chronic viral infection. *Nature* **439,** 682–687 (2006).

140. Wherry, E. J. *et al.* Molecular Signature of CD8+T Cell Exhaustion during Chronic Viral Infection. *Immunity* **27,** 670–684 (2007).

141. Sen, D. R. *et al.* The epigenetic landscape of T cell exhaustion. *Science (80-.).* **354,** 1165–1169 (2016).

142. Ye, B. *et al.* T-cell exhaustion in chronic hepatitis B infection: current knowledge and clinical significance. *Cell Death Dis.* **6,** e1694 (2015).

143. Restifo, N. P., Dudley, M. E. & Rosenberg, S. a. Adoptive immunotherapy for cancer: harnessing the T cell response. *Nat. Rev. Immunol.* **12,** 269–81 (2012).

144. Rosenberg, S. A. Raising the Bar: The Curative Potential of Human Cancer Immunotherapy. *Sci. Transl. Med.* **4,** 127ps8-127ps8 (2012).

145. Rosenberg, S. A., Spiess, P. & Lafreniere, R. A new approach to the adoptive immunotherapy of cancer with tumor-infiltrating lymphocytes. *Science* **233,** 1318–21 (1986).

146. Topalian, S. L., Muul, L. M., Solomon, D. & Rosenberg, S. A. Expansion of human tumor infiltrating lymphocytes for use in immunotherapy trials. *J. Immunol. Methods* **102,** 127–41 (1987).

147. Rosenberg, S. A. *et al.* Use of tumor-infiltrating lymphocytes and interleukin-2 in the immunotherapy of patients with metastatic melanoma. A preliminary report. *N. Engl. J. Med.* **319,** 1676–80 (1988).

148. Dudley, M. E. *et al.* Cancer regression and autoimmunity in patients after clonal repopulation with antitumor lymphocytes. *Science* **298,** 850–4 (2002).

149. Johnson, L. A. & June, C. H. Driving gene-engineered T cell immunotherapy of cancer. *Cell Res.* **27,** 38–58 (2017).

150. June, C. H., Riddell, S. R. & Schumacher, T. N. Adoptive cellular therapy : A race to the f nish line. *Sci. Transl. Med.* **7,** 1–8 (2015).

151. Morgan, R. A. *et al.* Cancer regression in patients after transfer of genetically engineered lymphocytes. *Science* **314,** 126–9 (2006).

152. Rosenberg, S. A. *et al.* Durable complete responses in heavily pretreated patients with metastatic melanoma using T-cell transfer immunotherapy. *Clin. Cancer Res.* **17,** 4550–7 (2011).

153. Robbins, P. F. *et al.* Tumor regression in patients with metastatic synovial cell sarcoma and melanoma using genetically engineered lymphocytes reactive with NY-ESO-1. *J. Clin. Oncol.* **29,** 917–24 (2011).

154. Robbins, P. F. *et al.* A pilot trial using lymphocytes genetically engineered with an NY-ESO-1-reactive T-cell receptor: Long-term follow-up and correlates with response. *Clin. Cancer Res.* **21,** 1019–1027 (2015).

155. Rapoport, A. P. *et al.* NY-ESO-1-specific TCR-engineered T cells mediate sustained antigen-specific antitumor effects in myeloma. *Nat. Med.* **21,** 914–921 (2015).

156. Johnson, L. a *et al.* Gene therapy with human and mouse T-cell receptors mediates cancer regression and targets normal tissues expressing cognate antigen. *Blood* **114,** 535–46 (2009).

157. Vinay, D. S. *et al.* Immune evasion in cancer: Mechanistic basis and therapeutic strategies. *Semin. Cancer Biol.* **35,** S185–S198 (2015).

158. Dunn, G. P., Old, L. J. & Schreiber, R. D. The Three Es of Cancer Immunoediting. *Annu. Rev. Immunol.* **22,** 329–360 (2004).

159. Morgan, R. A. *et al.* Cancer regression and neurological toxicity following anti-MAGE-A3 TCR gene therapy. *J. Immunother.* **36,** 133–151 (2013).

160. Linette, G. P. *et al.* Cardiovascular toxicity and titin cross-reactivity of af fi nity-enhanced T cells in myeloma and melanoma. *Blood* **122,** 863–872 (2013).

161. Kuwana, Y. *et al.* Expression of chimeric receptor composed of immunoglobulin-derived V resions and T-cell receptor-derived C regions. *Biochem. Biophys. Res. Commun.* **149,** 960–968 (1987).

162. Gross, G., Waks, T. & Eshhar, Z. Expression of immunoglobulin-T-cell receptor chimeric molecules as functional receptors with antibody-type specificity. *Proc. Natl. Acad. Sci. U. S. A.* **86,** 10024–8 (1989).

163. Eshhar, Z., Waks, T., Gross, G. & Schindler, D. G. Specific activation and targeting of cytotoxic lymphocytes through chimeric single chains consisting of antibody-binding domains and the gamma or zeta subunits of the immunoglobulin and T-cell receptors. *Proc. Natl. Acad. Sci.* **90,** 720–724 (1993).

164. Sadelain, M., Brentjens, R. & Rivière, I. The promise and potential pitfalls of chimeric antigen receptors. *Curr. Opin. Immunol.* **21,** 215–223 (2009).

165. Savoldo, B. *et al.* CD28 costimulation improves expansion and persistence of chimeric antigen receptor-modified T cells in lymphoma patients. *J. Clin. Invest.* **121,** 1822–6 (2011).

166. June, C. H., O'Connor, R. S., Kawalekar, O. U., Ghassemi, S. & Milone, M. C. CAR T cell immunotherapy for human cancer. *Science (80-.).* **359,** 1361–1365 (2018).

167. Milone, M. C. *et al.* Chimeric receptors containing CD137 signal transduction domains mediate enhanced survival of T cells and increased antileukemic efficacy in vivo. *Mol. Ther.* **17,** 1453–1464 (2009).

168. Carpenito, C. *et al.* Control of large, established tumor xenografts with genetically retargeted human T cells containing CD28 and CD137 domains. *Proc. Natl. Acad. Sci.* **106,** 3360–3365 (2009).

169. Kochenderfer, J. N. *et al.* Eradication of B-lineage cells and regression of lymphoma in a patient treated with autologous T cells genetically engineered to recognize CD19. *Blood* **116,** 4099–102 (2010).

170. Brentjens, R. J. *et al.* CD19-Targeted T Cells Rapidly Induce Molecular Remissions in Adults with Chemotherapy-Refractory Acute Lymphoblastic Leukemia. *Sci. Transl. Med.* **5,** 177ra38-177ra38 (2013).

171. Porter, D. L., Levine, B. L., Kalos, M., Bagg, A. & June, C. H. Chimeric antigen receptor-modified T cells in chronic lymphoid leukemia. *N. Engl. J. Med.* **365,** 725–33 (2011).

172. Tang, X.-Y. *et al.* Third-generation CD28/4-1BB chimeric antigen receptor T cells for chemotherapy relapsed or refractory acute lymphoblastic leukaemia: a non-randomised, open-label phase I trial protocol. *BMJ Open* **6,** e013904 (2016).

173. Brentjens, R. J. *et al.* Safety and persistence of adoptively transferred autologous CD19-targeted T cells in patients with relapsed or chemotherapy refractory B-cell leukemias. *Blood* **118,** 4817–4828 (2011).

174. Yip, A. & Webster, R. M. The market for chimeric antigen receptor T cell therapies. *Nat. Rev. Drug Discov.* **17,** 161–162 (2018).

175. Morgan, R. A. *et al.* Case report of a serious adverse event following the administration of T cells transduced with a chimeric antigen receptor recognizing ERBB2. *Mol. Ther.* **18,** 843–51 (2010).

176. Thistlethwaite, F. C. *et al.* The clinical efficacy of first-generation carcinoembryonic antigen (CEACAM5)-specific CAR T cells is limited by poor persistence and transient pre-conditioning-dependent respiratory toxicity. *Cancer Immunol. Immunother.* **66,** 1425–1436 (2017).

177. Newick, K., Moon, E. & Albelda, S. M. Chimeric antigen receptor T-cell therapy for solid tumors. *Mol. Ther. oncolytics* **3,** 16006 (2016).

178. Drake, C. G., Jaffee, E. & Pardoll, D. M. Mechanisms of immune evasion by tumors. *Adv. Immunol.* **90,** 51–81 (2006).

179. O'Rourke, D. M. *et al.* A single dose of peripherally infused EGFRvIII-directed CAR T cells mediates antigen loss and induces adaptive resistance in patients with recurrent glioblastoma. *Sci. Transl. Med.* **9,** (2017).

180. Fesnak, A. D., June, C. H. & Levine, B. L. Engineered T cells : the promise and challenges of cancer immunotherapy. *Nat. Publ. Gr.* **16,** 566–581 (2016).

181. Guedan, S. *et al.* ICOS-based chimeric antigen receptors program bipolar TH17/TH1 cells. *Blood* **124,** 1070–80 (2014).

182. Kantoff, P. W. P. *et al.* Sipuleucel-T immunotherapy for castration-resistant prostate cancer. *N. Engl. J. Med.* **363,** 411–422 (2010).

183. Chambers, J. D. & Neumann, P. J. Listening to Provenge--what a costly cancer treatment says about future Medicare policy. *N. Engl. J. Med.* **364,** 1687–1689 (2011).

184. Kim, J. V, Latouche, J.-B., Rivière, I. & Sadelain, M. The ABCs of artificial antigen presentation. *Nat. Biotechnol.* **22,** 403–10 (2004).

185. Spatz, J. P. & Geiger, B. Molecular Engineering of Cellular Environments: Cell Adhesion to Nano-Digital Surfaces. *Methods Cell Biol.* **83,** 89–111 (2007).

186. Deeg, J. *et al.* T cell activation is determined by the number of presented antigens. *Nano Lett.* **13,** 5619–26 (2013).

187. Matic, J., Deeg, J., Scheffold, A., Goldstein, I. & Spatz, J. P. Fine tuning and efficient T cell activation with stimulatory aCD3 nanoarrays. *Nano Lett.* **13,** 5090–7 (2013).

188. Delcassian, D. *et al.* Nanoscale ligand spacing influences receptor triggering in T cells and NK cells. *Nano Lett.* **13,** 5608–14 (2013).

189. Cai, H. *et al.* Molecular Occupancy of Nanodot Arrays. *ACS Nano* **10,** 4173–83 (2016).

190. Shen, K., Thomas, V. K., Dustin, M. L. & Kam, L. C. Micropatterning of costimulatory ligands enhances CD4+ T cell function. *Proc. Natl. Acad. Sci. U. S. A.* **105,** 7791–7796 (2008).

191. Bashour, K. T. *et al.* Cross talk between CD3 and CD28 is spatially modulated by protein lateral mobility. *Mol. Cell. Biol.* **34,** 955–64 (2014).

192. Pi, F. *et al.* Size-Tunable Organic Nanodot Arrays: A Versatile Platform for Manipulating and Imaging Cells. *Nano Lett.* **15,** 5178–5184 (2015).

193. Dillard, P., Pi, F., Lellouch, A. C., Limozin, L. & Sengupta, K. Nano-clustering of ligands on surrogate antigen presenting cells modulates T cell membrane adhesion and organization. *Integr. Biol. (Camb).* **8,** 287–301 (2016).

194. Mossman, K. & Groves, J. Micropatterned supported membranes as tools for quantitative studies of the immunological synapse. *Chem. Soc. Rev.* **36,** 46–54 (2007).

195. Sackmann, E. Supported Membrane: Scientific and Practical Applications. *Science (80-.).* **271,** 43–8 (1996).

196. Hsu, C.-J. *et al.* Ligand mobility modulates immunological synapse formation and T cell activation. *PLoS One* **7,** e32398 (2012).

197. Manz, B. N., Jackson, B. L., Petit, R. S., Dustin, M. L. & Groves, J. T-cell triggering thresholds are modulated by the number of antigen within individual T-cell receptor clusters. *Proc. Natl. Acad. Sci. U. S. A.* **108,** 9089–94 (2011).

198. Mossman, K. D., Campi, G., Groves, J. T. & Dustin, M. L. Altered TCR signaling from geometrically repatterned immunological synapses. *Science* **310,** 1191–3 (2005).

199. Varma, R., Campi, G., Yokosuka, T., Saito, T. & Dustin, M. L. T Cell Receptor-Proximal Signals Are Sustained in Peripheral Microclusters and Terminated in the Central Supramolecular Activation Cluster. *Immunity* **25,** 117–127 (2006).

200. Shen, K., Milone, M., Dustin, M. L. & Kam, L. C. Nanoengineering of Immune Cell Function. *Mater. Res. ...* 1–11 (2009). doi:10.1557/PROC-1209-YY03-01.Nanoengineering

201. Eggermont, L. J., Paulis, L. E., Tel, J. & Figdor, C. G. Towards efficient cancer immunotherapy: advances in developing artificial antigen-presenting cells. *Trends Biotechnol.* 1–10 (2014). doi:10.1016/j.tibtech.2014.06.007

202. Smith, M. R., Tolbert, S. V. & Wen, F. Protein-Scaffold Directed Nanoscale Assembly of T Cell Ligands: Artificial Antigen Presentation with Defined Valency, Density, and Ratio. *ACS Synth. Biol.* **7,** 1629–1639 (2018).

203. Sun, S. *et al.* Dual function of Drosophila cells as APCs for naive CD8+ T cells: implications for tumor immunotherapy. *Immunity* **4,** 555–64 (1996).

204. Cai, Z. *et al.* Transfected Drosophila cells as a probe for defining the minimal requirements for stimulating unprimed CD8+ T cells. *Proc. Natl. Acad. Sci. U. S. A.* **93,** 14736–14741 (1996).

205. Wen, F., Sethi, D. K., Wucherpfennig, K. W. & Zhao, H. Cell surface display of functional human MHC class II proteins: yeast display versus insect cell display. *Protein Eng. Des. Sel.* **24,** 701–9 (2011).

206. Schoenberger, S. P. *et al.* Efficient Direct Priming of Tumor-specific Cytotoxic T Lymphocyte in Vivo by an Engineered APC Efficient Direct Priming of Tumor-specific Engineered APC1 Cytotoxic T Lymphocyte in Vivo by an. 3094–3100 (1998).

207. Latouche, J. B. & Sadelain, M. Induction of human cytotoxic T lymphocytes by artificial antigen-presenting cells. *Nat. Biotechnol.* **18,** 405–9 (2000).

208. Papanicolaou, G. A. *et al.* Rapid expansion of cytomegalovirus-specific cytotoxic T lymphocytes by artificial antigen-presenting cells expressing a single HLA allele. *Blood* **102,** 2498–505 (2003).

209. Thomas, A. K., Maus, M. V., Shalaby, W. S., June, C. H. & Riley, J. L. A cell-based artificial antigen-presenting cell coated with anti-CD3 and CD28 antibodies enables rapid expansion and long-term growth of CD4 T lymphocytes. *Clin. Immunol.* **105,** 259–272 (2002).

210. Neal, L. R. *et al.* The Basics of Artificial Antigen Presenting Cells in T Cell-Based Cancer Immunotherapies. *J. Immunol. Res. Ther.* **2,** 68–79 (2017).

211. Steinman, R. M. & Banchereau, J. Taking dendritic cells into medicine. **449,** 419–426 (2007).

212. Crispe, I. N., Bevan, M. J. & Staerz, U. D. Selective activation of Lyt 2+ precursor T cells by ligation of the antigen receptor. *Nature* **317,** 627–629 (1985).

213. Manger, B., Weiss, a, Weyand, C., Goronzy, J. & Stobo, J. D. T cell activation: differences in the signals required for IL 2 production by nonactivated and activated T cells. *J. Immunol.* **135,** 3669–73 (1985).

214. Curtsinger, J., Deeths, M. J., Pease, P. & Mescher, M. F. Artificial cell surface constructs for studying receptor-ligand contributions to lymphocyte activation. *J. Immunol. Methods* **209,** 47–57 (1997).

215. Tham, E. L., Jensen, P. L. & Mescher, M. F. Activation of antigen-specific T cells by artificial cell constructs having immobilized multimeric peptide-class I complexes and recombinant B7-Fc proteins. *J. Immunol. Methods* **249,** 111–119 (2001).

216. Oelke, M. & Schneck, J. P. Overview of a HLA-Ig based 'lego-like system' for T cell monitoring, modulation and expansion. *Immunol. Res.* **47,** 248–256 (2010).

217. Steenblock, E. R. & Fahmy, T. M. A comprehensive platform for ex vivo T-cell expansion based on biodegradable polymeric artificial antigen-presenting cells. *Mol. Ther.* **16,** 765–772 (2008).

218. Sunshine, J. C., Perica, K., Schneck, J. P. & Green, J. J. Particle shape dependence of CD8+ T cell activation by artificial antigen presenting cells. *Biomaterials* **35,** 269–77 (2014).

219. Prakken, B. *et al.* Artificial antigen-presenting cells as a tool to exploit the immune 'synapse'. *Nat. Med.* **6,** 1406–1410 (2000).

220. De La Peña, H. *et al.* Artificial exosomes as tools for basic and clinical immunology. *J. Immunol. Methods* **344,** 121–132 (2009).

221. Zappasodi, R. *et al.* The effect of artificial antigen-presenting cells with preclustered anti-CD28/-CD3/-LFA-1 monoclonal antibodies on the induction of ex vivo expansion of functional human antitumor T cells. *Haematologica* **93,** 1523–34 (2008).

222. Mandal, S. *et al.* Therapeutic nanoworms: towards novel synthetic dendritic cells for immunotherapy. *Chem. Sci.* **4,** 4168 (2013).

223. Hammink, R. *et al.* Controlling T-Cell Activation with Synthetic Dendritic Cells Using the Multivalency Effect. *ACS omega* **2,** 937–945 (2017).

224. Cheung, A. S., Zhang, D. K. Y., Koshy, S. T. & Mooney, D. J. Scaffolds that mimic antigen-presenting cells enable ex vivo expansion of primary T cells. *Nat. Biotechnol.* **36,** 160–169 (2018).

225. Meyer, R. A. *et al.* Biodegradable nanoellipsoidal artificial antigen presenting cells for antigen specific T-cell activation. *Small* **11,** 1519–25 (2015).

226. Perica, K. *et al.* Enrichment and Expansion with Nanoscale Artificial Antigen Presenting Cells for Adoptive Immunotherapy. *ACS Nano* **9,** 6861–71 (2015).

227. Sunshine, J. C. & Green, J. J. Nanoengineering approaches to the design of artificial antigen-presenting cells. *Nanomedicine (Lond).* **8,** 1173–89 (2013).

228. Trickett, A. & Kwan, Y. L. T cell stimulation and expansion using anti-CD3/CD28 beads. *J. Immunol. Methods* **275,** 251–5 (2003).

229. Oelke, M. *et al.* Ex vivo induction and expansion of antigen-specific cytotoxic T cells by HLA-Ig-coated artificial antigen-presenting cells. *Nat. Med.* **9,** 619–624 (2003).

230. Decuzzi, P. *et al.* Size and shape effects in the biodistribution of intravascularly injected particles. *J. Control. Release* **141,** 320–327 (2010).

231. van der Weijden, J., Paulis, L. E., Verdoes, M., van Hest, J. C. M. & Figdor, C. G. The right touch: design of artificial antigen-presenting cells to stimulate the immune system. *Chem. Sci.* **5,** 3355–3367 (2014).

232. Bertrand, N. & Leroux, J. The journey of a drug-carrier in the body: An anatomo-physiological perspective. *J. Control. Release* **161,** 152–163 (2012).

233. Uchtenhagen, H. *et al.* Efficient ex vivo analysis of CD4+ T-cell responses using combinatorial HLA class II tetramer staining. *Nat. Commun.* **7,** 12614 (2016).

234. Banchereau, J. & Palucka, a K. Dendritic cells as therapeutic vaccines against cancer. *Nat. Rev. Immunol.* **5,** 296–306 (2005).

235. Dar, H. *et al.* Prediction of promiscuous T-cell epitopes in the Zika virus polyprotein: An in silico approach. *Asian Pac. J. Trop. Med.* **9,** 844–850 (2016).

236. Andreatta, M. *et al.* Accurate pan-specific prediction of peptide-MHC class II binding affinity with improved binding core identification. *Immunogenetics* **67,** 641–650 (2015).

237. Nielsen, M., Lund, O., Buus, S. & Lundegaard, C. MHC Class II epitope predictive algorithms. *Immunology* **130,** 319–328 (2010).

238. Wang, P. *et al.* A systematic assessment of MHC class II peptide binding predictions and evaluation of a consensus approach. *PLoS Comput. Biol.* **4,** e1000048 (2008).

239. Jensen, P. E., Moore, J. C. & Lukacher, A. E. A europium fluoroimmunoassay for measuring peptide binding to MHC class I molecules. *J. Immunol. Methods* **215,** 71–80 (1998).

240. Sidney, J. *et al. Measurement of MHC/peptide interactions by gel filtration or monoclonal antibody capture*. *Current Protocols in Immunology* (2013). doi:10.1002/0471142735.im1803s100

241. Zarutskie, J. a *et al.* The kinetic basis of peptide exchange catalysis by HLA-DM. *Proc. Natl. Acad. Sci. U. S. A.* **98,** 12450–5 (2001).

242. Joshi, R. V., Zarutskie, J. A. & Stern, L. J. A three-step kinetic mechanism for peptide binding to MHC class II proteins. *Biochemistry* **39,** 3751–62 (2000).

243. Narayan, K., Su, K. W., Chou, C. L., Khoruzhenko, S. & Sadegh-Nasseri, S. HLA-DM mediates peptide exchange by interacting transiently and repeatedly with HLA-DR1. *Mol. Immunol.* **46,** 3157–3162 (2009).

244. Maiers, M., Gragert, L. & Klitz, W. Corrigendum to "High-resolution HLA alleles and haplotypes in the United States population" [Hum Imunol 68 (2007) 779–788]. *Hum. Immunol.* **69,** 141 (2008).

245. Reynolds, C. *et al.* T Cell Immunity to the Alkyl Hydroperoxide Reductase of Burkholderia pseudomallei: A Correlate of Disease Outcome in Acute Melioidosis. *J. Immunol.* **194,** 4814–24 (2015).

246. Jain, S., Vashistt, J., Gupta, K., Kumar, A. & Changotra, H. Molecular Analysis of VP7 Gene of Rotavirus G1 Strains Isolated from North India. *Curr. Microbiol.* **73,** 1–9 (2016).

247. Aoki, S. T. *et al.* Structure of Rotavirus Outer-Layer Protein VP7 Bound with a Neutralizing Fab. *Science (80-.).* **324,** 1444–1447 (2009).

248. Dai, L. *et al.* Structures of the Zika Virus Envelope Protein and Its Complex with a Flavivirus Broadly Protective Antibody. *Cell Host Microbe* **19,** 696–704 (2016).

249. Robbiani, D. F. *et al.* Recurrent Potent Human Neutralizing Antibodies to Zika Virus in Brazil and Mexico. *Cell* **169,** 597–609.e11 (2017).

250. Tai, W. *et al.* Critical neutralizing fragment of Zika virus EDIII elicits cross-neutralization and protection against divergent Zika viruses article. *Emerg. Microbes Infect.* **7,** (2018).

251. Wang, P. *et al.* Peptide binding predictions for HLA DR, DP and DQ molecules. *BMC Bioinformatics* **11,** 568 (2010).

252. Oseroff, C. *et al.* Molecular determinants of T cell epitope recognition to the common Timothy grass allergen. *J. Immunol.* **185,** 943–55 (2010).

253. Madhi, S., Cunliffe, N. & Steele, D. Effect of human rotavirus vaccine on severe diarrhea in African infants. *... Engl. J. ...* 289–298 (2010).

254. Ciarlet, M. & Schödel, F. Development of a rotavirus vaccine: clinical safety, immunogenicity, and efficacy of the pentavalent rotavirus vaccine, RotaTeq. *Vaccine* **27 Suppl 6,** G72-81 (2009).

255. Ward, R. L. & Bernstein, D. I. Rotarix: A Rotavirus Vaccine for the World. *Clin. Infect. Dis.* **48,** 222–228 (2009).

256. Zeller, M. *et al.* Genetic analyses reveal differences in the VP7 and VP4 antigenic epitopes between human rotaviruses circulating in Belgium and rotaviruses in Rotarix and RotaTeq. *J. Clin. Microbiol.* **50,** 966–76 (2012).

257. Stettler, K. *et al.* Specificity, cross-reactivity, and function of antibodies elicited by Zika virus infection. *Science* **353,** 823–6 (2016).

258. Xu, X. *et al.* Identifying Candidate Targets of Immune Responses in Zika Virus Based on Homology to Epitopes in Other Flavivirus Species. *PLoS Curr.* **8,** (2016).

259. Paul, L. M. *et al.* Dengue virus antibodies enhance Zika virus infection. *Clin. Transl. Immunol.* **5,** e117 (2016).

260. Lima, N. S., Rolland, M., Modjarrad, K. & Trautmann, L. T Cell Immunity and Zika Virus Vaccine Development. *Trends Immunol.* **38,** 594–605 (2017).

261. Zellweger, R. M. *et al.* Role of Humoral versus Cellular Responses Induced by a Protective Dengue Vaccine Candidate. *PLoS Pathog.* **9,** (2013).

262. Aid, M. *et al.* Zika Virus Persistence in the Central Nervous System and Lymph Nodes of Rhesus Monkeys. *Cell* **169,** 610–620.e14 (2017).

263. Mlakar, J. *et al.* Zika Virus Associated with Microcephaly. *N. Engl. J. Med.* **374,** 951–958 (2016).

264. Petersen, E. *et al.* Rapid Spread of Zika Virus in The Americas - Implications for Public Health Preparedness for Mass Gatherings at the 2016 Brazil Olympic Games. *Int. J. Infect. Dis.* **44,** 11–15 (2016).

265. Lessler, J. *et al.* Assessing the global threat from Zika virus. *Science (80-.).* **353,** (2016).

266. Reynolds, C. J. *et al.* T cell immunity to Zika virus targets immunodominant epitopes that show cross-reactivity with other Flaviviruses. *Sci. Rep.* **8,** 1–12 (2018).

267. Manca, F. *et al.* Constraints in T-B cooperation related to epitope topology on E. coli beta-galactosidase. I. The fine specificity of T cells dictates the fine specificity of antibodies directed to conformation-dependent determinants. *Eur. J. Immunol.* **15,** 345–50 (1985).

268. Berzofsky, J. A. T-B reciprocity. An Ia-restricted epitope-specific circuit regulating T cell-B cell interaction and antibody specificity. *Surv. Immunol. Res.* **2,** 223–9 (1983).

269. Lanzavecchia, A. Antigen-specific interaction between T and B cells. *Nature* **314,** 537–9 (1983).

270. Rivino, L. *et al.* Differential Targeting of Viral Components by CD4+ versus CD8+ T Lymphocytes in Dengue Virus Infection. *J. Virol.* **87,** 2693–2706 (2013).

271. Sette, A. *et al.* Selective CD4+T Cell Help for Antibody Responses to a Large Viral Pathogen: Deterministic Linkage of Specificities. *Immunity* **28,** 847–858 (2008).

272. Swain, S. L., McKinstry, K. K. & Strutt, T. M. Expanding roles for $CD4^+$ T cells in immunity to viruses. *Nat. Rev. Immunol.* **12,** 136–48 (2012).

273. Ahmad, T. A., Eweida, A. E. & El-Sayed, L. H. T-cell epitope mapping for the design of powerful vaccines. *Vaccine Reports* **6,** 13–22 (2016).

274. Oyarzún, P., Ellis, J. J., Bodén, M. & Kobe, B. PREDIVAC: CD4+ T-cell epitope prediction for vaccine design that covers 95% of HLA class II DR protein diversity. *BMC Bioinformatics* **14,** 52 (2013).

275. Kalandadze, A., Galleno, M., Foncerrada, L., Strominger, J. L. & Wucherpfennig, K. W. Expression of recombinant HLA-DR2 molecules. *J. Biol. Chem.* **271,** 20156–20162 (1996).

276. Jang, M.-H., Seth, N. P. & Wucherpfennig, K. W. Ex Vivo Analysis of Thymic CD4 T Cells in Nonobese Diabetic Mice with Tetramers Generated from I-Ag7/Class II-Associated Invariant Chain Peptide Precursors. *J. Immunol.* **171,** 4175–4186 (2003).

277. Kinnear, G., Jones, N. D. & Wood, K. J. Costimulation Blockade. *Transplant. J.* **95,** 527–535 (2013).

278. Groves, J. T. & Dustin, M. L. Supported planar bilayers in studies on immune cell adhesion and communication. *J. Immunol. Methods* **278,** 19–32 (2003).

279. Irvine, D. J. & Doh, J. Synthetic surfaces as artificial antigen presenting cells in the study of T cell receptor triggering and immunological synapse formation. *Semin. Immunol.* **19,** 245–54 (2007).

280. Cai, H. *et al.* Bifunctional nanoarrays for probing the immune response at the single-molecule level. *J. Vac. Sci. Technol. B Nanotechnol. Microelectron.* **31,** 6F902 (2013).

281. Doh, J. & Irvine, D. J. Immunological synapse arrays: patterned protein surfaces that modulate immunological synapse structure formation in T cells. *Proc. Natl. Acad. Sci. U. S. A.* **103,** 5700–5 (2006).

282. Cochran, J. R., Cameron, T. O., Stone, J. D., Lubetsky, J. B. & Stern, L. J. Receptor proximity, not intermolecular orientation, is critical for triggering T-cell activation. *J. Biol. Chem.* **276,** 28068–74 (2001).

283. Bennett, N. R., Zwick, D. B., Courtney, A. H. & Kiessling, L. L. Multivalent Antigens for Promoting B and T Cell Activation. *ACS Chem. Biol.* **10,** 1817–24 (2015).

284. Motta, I., Lone, Y.-C. & Kourilsky, P. In vitro induction of naive cytotoxic T lymphocytes with complexes of peptide and recombinant MHC class I molecules coated onto beads: role of TCR/ligand density. *Eur. J. Immunol.* **28,** 3685–3695 (1998).

285. Perica, K., Kosmides, A. K. & Schneck, J. P. Linking form to function: Biophysical aspects of artificial antigen presenting cell design. *Biochim. Biophys. Acta* **1853,** 781–90 (2015).

286. Bosch, B., Heipertz, E. L., Drake, J. R. & Roche, P. A. Major histocompatibility complex (MHC) class II-peptide complexes arrive at the plasma membrane in cholesterol-rich microclusters. *J. Biol. Chem.* **288,** 13236–13242 (2013).

287. Schamel, W. W. A. & Alarcón, B. Organization of the resting TCR in nanoscale oligomers. *Immunol. Rev.* **251,** 13–20 (2013).

288. Kamalasanan, K. *et al.* Patchy, anisotropic microspheres with soft protein islets. *Angew. Chem. Int. Ed. Engl.* **50,** 8706–8 (2011).

289. Chen, B. *et al.* Janus particles as artificial antigen-presenting cells for T cell activation. *ACS Appl. Mater. Interfaces* **6,** 18435–9 (2014).

290. Li, Y. & Kurlander, R. J. Comparison of anti-CD3 and anti-CD28-coated beads with soluble anti-CD3 for expanding human T cells: Differing impact on CD8 T cell phenotype and responsiveness to restimulation. *J. Transl. Med.* **8,** 104 (2010).

291. Sun, F., Zhang, W.-B., Mahdavi, A., Arnold, F. H. & Tirrell, D. A. Synthesis of bioactive protein hydrogels by genetically encoded SpyTag-SpyCatcher chemistry. *Proc. Natl. Acad. Sci.* **111,** 11269–11274 (2014).

292. Boder, E. T., Bill, J. R., Nields, A. W., Marrack, P. C. & Kappler, J. W. Yeast surface display of a noncovalent MHC class II heterodimer complexed with antigenic peptide. *Biotechnol. Bioeng.* **92,** 485–91 (2005).

293. Smith, M. R., Khera, E. & Wen, F. Engineering Novel and Improved Biocatalysts by Cell Surface Display. *Ind. Eng. Chem. Res.* **54,** 4021–4032 (2015).

294. Boder, E. T. & Wittrup, K. D. Yeast surface display for screening combinatorial polypeptide libraries. *Nat. Biotechnol.* **15,** 553–7 (1997).

295. Gai, S. A. & Wittrup, K. D. Yeast surface display for protein engineering and characterization. *Curr. Opin. Struct. Biol.* **17,** 467–73 (2007).

296. Smith, S. N., Harris, D. T. & Kranz, D. M. *Yeast Surface Display*. **1319,** (Springer New York, 2015).

297. Wu, C. H., Mulchandani, A. & Chen, W. Versatile microbial surface-display for environmental remediation and biofuels production. *Trends Microbiol.* **16,** 181–188 (2008).

298. Gerngross, U. T., Romaniec, M. P., Kobayashi, T., Huskisson, N. S. & Demain, a L. Sequencing of a Clostridium thermocellum gene (cipA) encoding the cellulosomal SL-protein reveals an unusual degree of internal homology. *Mol. Microbiol.* **8,** 325–34 (1993).

299. Wen, F., Sun, J. & Zhao, H. Yeast surface display of trifunctional minicellulosomes for simultaneous saccharification and fermentation of cellulose to ethanol. *Appl. Environ. Microbiol.* **76,** 1251–60 (2010).

300. Handelsman, T. *et al.* Cohesin-dockerin interaction in cellulosome assembly: a single Asp-to-Asn mutation disrupts high-affinity cohesin-dockerin binding. *FEBS Lett.* **572,** 195–200 (2004).

301. Stern, L. J. *et al.* Crystal structure of the human class II MHC protein HLA-DR1 complexed with an influenza virus peptide. *Nature* **368,** 215–21 (1994).

302. Hennecke, J., Carfi, A. & Wiley, D. C. Structure of a covalently stabilized complex of a human alphabeta T-cell receptor, influenza HA peptide and MHC class II molecule, HLA-DR1. *EMBO J.* **19,** 5611–24 (2000).

303. Xie, J. *et al.* Photocrosslinkable pMHC monomers stain T cells specifically and cause ligand-bound TCRs to be 'preferentially' transported to the cSMAC. *Nat. Immunol.* **13,** 674–680 (2012).

304. Wang, X. X. & Shusta, E. V. The use of scFv-displaying yeast in mammalian cell surface selections. *J. Immunol. Methods* **304,** 30–42 (2005).

305. Lillemeier, B. F. *et al.* TCR and Lat are expressed on separate protein islands on T cell membranes and concatenate during activation. *Nat. Immunol.* **11,** 90–96 (2010).

306. Dustin, M. L. & Springer, T. A. T-cell receptor cross-linking transiently stimulates adhesiveness through LFA-1. *Nature* **341,** 619–24 (1989).

307. Lollo, B. a, Chan, K. W., Hanson, E. M., Moy, V. T. & Brian, a a. Direct evidence for two affinity states for lymphocyte function-associated antigen 1 on activated T cells. *J. Biol. Chem.* **268,** 21693–700 (1993).

308. Mueller, K. L. *et al.* Cutting edge: LFA-1 integrin-dependent T cell adhesion is regulated by both ag specificity and sensitivity. *J. Immunol.* **173,** 2222–6 (2004).

309. Comrie, W. A., Li, S., Boyle, S. & Burkhardt, J. K. The dendritic cell cytoskeleton promotes T cell adhesion and activation by constraining ICAM-1 mobility. *J. Cell Biol.* **208,** 457–73 (2015).

310. Suzuki, J., Yamasaki, S., Wu, J., Koretzky, G. A. & Saito, T. The actin cloud induced by LFA-1-mediated outside-in signals lowers the threshold for T-cell activation. *Blood* **109,** 168–75 (2007).

311. Zuckerman, L. A., Pullen, L. & Miller, J. Functional consequences of costimulation by ICAM-1 on IL-2 gene expression and T cell activation. *J. Immunol.* **160,** 3259–68 (1998).

312. Smits, H. H. *et al.* Intercellular adhesion molecule-1/LFA-1 ligation favors human Th1 development. *J. Immunol.* **168,** 1710–6 (2002).

313. Kalandadze, A., Galleno, M., Foncerrada, L., Strominger, J. L. & Wucherpfennig, K. W. Expression of Recombinant HLA-DR2 Molecules. *J. Biol. Chem.* **271,** 20156–20162 (1996).

314. Boen, E., Crownover, a R., McIlhaney, M., Korman, a J. & Bill, J. Identification of T Cell Ligands in a Library of Peptides Covalently Attached to HLA-DR4. *J. Immunol.* **165,** 2040–2047 (2000).

315. Stern, J., Moraïs, S., Lamed, R. & Bayer, E. A. Adaptor Scaffoldins: An Original Strategy for Extended Designer Cellulosomes, Inspired from Nature. *MBio* **7,** e00083 (2016).

316. Tsai, S.-L. L., DaSilva, N. A. & Chen, W. Functional display of complex cellulosomes on the yeast surface via adaptive assembly. *ACS Synth. Biol.* **2,** 14–21 (2013).

317. Fan, L.-H. L., Zhang, Z.-J. Z., Yu, X. X.-Y., Xue, Y.-X. & Tan, T.-W. Self-surface assembly of cellulosomes with two miniscaffoldins on Saccharomyces cerevisiae for cellulosic ethanol production. *Proc. Natl. Acad. Sci. U. S. A.* **109,** 1–6 (2012).

318. Moraïs, S. *et al.* Deconstruction of lignocellulose into soluble sugars by native and designer cellulosomes. *MBio* **3,** 1–11 (2012).

319. Bugada, L. F., Smith, M. R. & Wen, F. Engineering Spatially Organized Multienzyme Assemblies for Complex Chemical Transformation. *ACS Catal.* 7898–7906 (2018). doi:10.1021/acscatal.8b01883

320. Artzi, L., Bayer, E. A. & Moraïs, S. Cellulosomes: bacterial nanomachines for dismantling plant polysaccharides. *Nat. Rev. Microbiol.* **15,** 83–95 (2016).

321. Bayer, E. A., Belaich, J.-P., Shoham, Y. & Lamed, R. The Cellulosomes: Multienzyme Machines for Degradation of Plant Cell Wall Polysaccharides. *Annu. Rev. Microbiol.* **58,** 521–554 (2004).

322. Fontes, C. M. G. A. & Gilbert, H. J. Cellulosomes: Highly Efficient Nanomachines Designed to Deconstruct Plant Cell Wall Complex Carbohydrates. *Annu. Rev. Biochem.* **79,** 655–681 (2010).

323. Dodds, D. R. & Gross, R. A. Chemistry: Chemicals from biomass. *Science* **318,** 1250–1251 (2007).

324. Gupta, N. K., Fukuoka, A. & Nakajima, K. Amorphous Nb2O5as a Selective and Reusable Catalyst for Furfural Production from Xylose in Biphasic Water and Toluene. *ACS Catal.* **7,** 2430–2436 (2017).

325. Zinoviev, S. *et al.* Next-generation biofuels: Survey of emerging technologies and sustainability issues. *ChemSusChem* **3,** 1106–1133 (2010).

326. Huber, G. W., Iborra, S. & Corma, A. Synthesis of transportation fuels from biomass: Chemistry, catalysts, and engineering. *Chemical Reviews* **106,** 4044–4098 (2006).

327. Isikgor, F. H. & Becer, C. R. Lignocellulosic biomass: a sustainable platform for the production of bio-based chemicals and polymers. *Polym. Chem.* **6,** 4497–4559 (2015).

328. Caes, B. R., Teixeira, R. E., Knapp, K. G. & Raines, R. T. Biomass to Furanics: Renewable Routes to Chemicals and Fuels. *ACS Sustain. Chem. Eng.* **3,** 2591–2605 (2015).

329. Himmel, M. E. & Bayer, E. A. Lignocellulose conversion to biofuels: current challenges, global perspectives. *Current Opinion in Biotechnology* **20,** 316–317 (2009).

330. Yeh, T. M. *et al.* Hydrothermal catalytic production of fuels and chemicals from aquatic biomass. *J. Chem. Technol. Biotechnol.* **88,** 13–24 (2013).

331. Wen, F., Nair, N. U. & Zhao, H. Protein engineering in designing tailored enzymes and microorganisms for biofuels production. *Curr. Opin. Biotechnol.* **20,** 412–419 (2009).

332. Horn, S. J., Vaaje-Kolstad, G., Westereng, B. & Eijsink, V. G. H. Novel enzymes for the degradation of cellulose. *Biotechnology for Biofuels* **5,** (2012).

333. Percival Zhang, Y. H., Himmel, M. E. & Mielenz, J. R. Outlook for cellulase improvement: Screening and selection strategies. *Biotechnology Advances* **24,** 452–481 (2006).

334. Schwarz, W. H. The cellulosome and cellulose degradation by anaerobic bacteria. *Appl. Microbiol. Biotechnol.* **56,** 634–649 (2001).

335. Lynd, L. R., Weimer, P. J., van Zyl, W. H. & Pretorius, I. S. Microbial Cellulose Utilization: Fundamentals and Biotechnology. *Microbiol. Mol. Biol. Rev.* **66,** 739–739 (2002).

336. Shang, B. Z. & Chu, J. W. Kinetic modeling at single-molecule resolution elucidates the mechanisms of cellulase synergy. *ACS Catal.* **4,** 2216–2225 (2014).

337. Percival Zhang, Y. H. *et al.* A transition from cellulose swelling to cellulose dissolution by o-phosphoric acid: evidence from enzymatic hydrolysis and supramolecular structure. *Biomacromolecules* **7,** 644–8 (2006).

338. Morais, S. *et al.* Cellulase-xylanase synergy in designer cellulosomes for enhanced degradation of a complex cellulosic substrate. *MBio* **1,** e00285-10 (2010).

339. Boder, E. T. & Wittrup, K. D. Yeast surface display for screening combinatorial polypeptide libraries. *Nat. Biotechnol.* **15,** 553–7 (1997).

340. Liang, Y., Si, T., Ang, E. L. & Zhao, H. An Engineered Pentafunctional Minicellulosome for Simultaneous Saccharification and Ethanol Fermentation in Saccharomyces cerevisiae. *Appl. Environ. Microbiol.* **80,** 6677–6684 (2014).

341. Bayer, E. A., Shimon, L. J. W., Shoham, Y. & Lamed, R. Cellulosomes—Structure and Ultrastructure. *J. Struct. Biol.* **124,** 221–234 (1998).

342. Davis, K. A., Abrams, B., Iyer, S. B., Hoffman, R. A. & Bishop, J. E. Determination of CD4 antigen density on cells: role of antibody valency, avidity, clones, and conjugation. *Cytometry* **33,** 197–205 (1998).

343. Gratama, J. W. *et al.* Flow cytometric quantitation of immunofluorescence intensity: Problems and perspectives. *Cytometry* **33,** 166–178 (1998).

344. Smith, M. R., Tolbert, S. V. & Wen, F. *Protein-scaffold Directed Nanoscale Assembly of T Cell Ligands: Artificial Antigen Presentation with Defined Valency, Density and Ratio*. *ACS Synthetic Biology* (2018). doi:10.1021/acssynbio.8b00119

345. O'Connor, R. S. *et al.* Substrate Rigidity Regulates Human T Cell Activation and Proliferation. *J. Immunol.* **189,** 1330–1339 (2012).

346. Judokusumo, E., Tabdanov, E., Kumari, S., Dustin, M. L. & Kam, L. C. Mechanosensing in T lymphocyte activation. *Biophys. J.* **102,** L5–L7 (2012).

347. Lambert, L. H. *et al.* Improving T Cell Expansion with a Soft Touch. *Nano Lett.* **4086,** acs.nanolett.6b04071 (2017).

348. Antony, P. A. *et al.* CD8+ T Cell Immunity Against a Tumor/Self-Antigen Is Augmented by CD4+ T Helper Cells and Hindered by Naturally Occurring T Regulatory Cells. *J. Immunol.* **174,** 2591–2601 (2005).

349. Muranski, P. & Restifo, N. P. Adoptive immunotherapy of cancer using CD4+T cells. *Curr. Opin. Immunol.* **21,** 200–208 (2009).

350. Caserta, S., Alessi, P., Guarnerio, J., Basso, V. & Mondino, A. Synthetic CD4+ T cell-targeted antigen-presenting cells elicit protective antitumor responses. *Cancer Res.* **68,** 3010–3018 (2008).

351. Hunder, N. N. *et al.* Treatment of metastatic melanoma with autologous CD4+ T cells against NY-ESO-1. *N Engl J Med* **358,** 2698–2703 (2008).

352. Tran, E. *et al.* Cancer immunotherapy based on mutation-specific CD4+ T cells in a patient with epithelial cancer. *Science* **344,** 641–5 (2014).

353. Gotwals, P. *et al.* Prospects for combining targeted and conventional cancer therapy with immunotherapy. *Nat. Rev. Cancer* **17,** 286–301 (2017).

354. Lelieveld, S. H., Veltman, J. A. & Gilissen, C. Novel bioinformatic developments for exome sequencing. *Hum. Genet.* **135,** 603–14 (2016).

355. Chester, C. & Maecker, H. T. Algorithmic Tools for Mining High-Dimensional Cytometry Data. *J. Immunol.* **195,** 773–779 (2015).

356. Bayer, E. A., Morag, E. & Lamed, R. The cellulosome--a treasure-trove for biotechnology. *Trends Biotechnol.* **12,** 379–86 (1994).